Correlating Synthetic Methods, Morphology, Atomic-Level Structure and Catalytic Activity of Sn-β Catalysts

Patrick Wolf,[a,b,‡] *Maxence Valla,*[a,‡] *Francisco Núñez-Zarur,*[a,c‡] *Aleix Comas-Vives,*[a,*,‡] *Aaron J. Rossini,*[d,†,‡]
Connor Firth,[b] *Hana Kallas,*[b] *Anne Lesage,*[e] *Lyndon Emsley,*[d] *Christophe Copéret,*[a,*] *and Ive Hermans*[b,*]

[a]Department of Chemistry and Applied Biosciences, ETH Zurich, Vladimir Prelog Weg 2, 8093 Zurich
(Switzerland)

[b]Department of Chemistry & Department of Chemical and Biological Engineering, University of
Wisconsin – Madison, 1101 University Avenue, Madison, WI 53706 (USA)

[c] Instituto de Química, Universidad de Antioquia, Calle 70 N°. 52-21, Medellín, Colombia

[d]Institut des Sciences et Ingénierie Chimiques, Ecole Polytechnique Fédérale de Lausanne (EPFL), 1015
Lausanne (Switzerland)

[e]Centre de RMN à Tres Hauts Champs, Institut de Sciences Analytiques, Université de Lyon
(CNRS/ENS Lyon/UCB Lyon 1) 69100 Villeurbanne (France)

[†]current address: Department of Chemistry, Iowa State University, Ames, IA, 50011 (USA)

ABSTRACT: Sn-β zeolites prepared using different recipes feature very different catalytic activity for aqueous phase glucose isomerization, suggesting the presence of different active sites. A systematic study of the morphology and atomic-level structure of the materials using DNP NMR spectroscopy in combination with first principles calculations allows for the discrimination between potential sites and leads to a proposal of specific structural features that are important for high activity. The results indicate that the materials showing highest activity posses a highly hydrophobic, defect-free zeolite framework. Those materials show so-called closed and associated partially hydrolyzed Sn(IV)-sites in the T6 and T5/T7 lattice position. On the other hand post-synthetically synthesized Sn-β samples prepared in two steps *via* dealumination and subsequent solid-state ion-exchange from Al-β show significant lower activity which is associated with a hydrophilic framework and/or a lower accessibility and lattice position of the Sn sites in the zeolite crystal. Further we provide a method to distinguish between different Sn sites based on NMR cartography using chemical shift and chemical shift anisotropy as readily measurable parameters. This cartography not only allows identifying the nature of the active sites (closed, defect-open and hydrolyzed-open), but also their position within the BEA framework.

KEYWORDS: Zeolites - Sn-β, DNP SENS - glucose isomerization - ^{119}Sn solid state NMR - Ab Initio Calculations - stannosilicates

INTRODUCTION

Isomorphous substitution of a small fraction of the Si(IV) centers in the crystalline framework of zeolites with Lewis acids results in promising heterogeneous catalysts.[1] In particular, Sn(IV) centers incorporated into zeolite β (BEA topology) catalyze a number of atom-efficient and industrially attractive transformations, such as the Baeyer-Villiger oxidation with hydrogen peroxide,[2] the Meerwein-Pondorf-Verley-Oppenauer hydrogen-transfer reaction[3] and the isomerization of monosaccharides.[4] More recently, Sn-β has also been found to promote direct aldol reactions[5] and other C-C coupling reactions in the development of new routes for the production of important intermediates such as α-hydroxy-γ-butyrolactone[6] and 4-(hydroxymethyl)benzoic acid derivatives[7].

Sn-β is traditionally synthesized by direct incorporation of Sn(IV) centers into the zeolite β framework during hydrothermal synthesis.[2,3a,3b,4b,4c] Unfortunately, this procedure is typically associated with long synthesis timescales, and only limited amounts of tin may be incorporated. For these reasons, there has been a large effort in developing faster synthesis protocols[8] and post-synthetic methods (*i.e.*, incorporating tin into dealuminated β zeolite) to produce Sn-β.[9] However, the catalytic activities of the resulting materials strongly depend on the synthetic method. It is, however, not clear that materials obtained by different synthetic routes result in Sn(IV) sites having the same molecular environment. In addition, the nature and identity of the active sites in Sn-β themselves are still matter of intense debate. The challenge in determining the active sites is pronounced as the crystal structure of the zeolite BEA shows nine crystallographically distinct sites,[10] referred to as "T-sites" as depicted in Figure 1 (top). All of these sites can potentially be substituted by tin, a problem generally observed for zeolites containing heteroatoms.[11] Vjunov *et al.* recently combined EXAFS and solid state NMR to quantitatively probe the Al-distribution in the corresponding commercial Al-β.[12]

Solid-state NMR spectroscopy has emerged as a powerful technique to identify the structure of tin-containing materials and can be used to investigate the differences in structures and environments of Sn(IV) centers in different Sn-β materials. Davis and co-workers acquired ^{119}Sn solid-state NMR spectra of ^{119}Sn-labeled Sn-β obtained from hydrothermal synthesis.[13] In their study, ^{119}Sn isotopic enrichment was required because of the combined low natural abundance of ^{119}Sn (NA = 8.6 %) and the low Sn-content of the samples (typically 1-2 wt%). It was proposed that both "closed" [$(SiO)_4Sn$] and "open" [$(SiO)_3Sn(OH)$] Sn sites are present in these materials[14] (Figure 1, bottom) and that the open sites would be most active for the glucose isomerization.[13,15] Density functional theory (DFT) calculations on cluster models also suggest a higher inherent activity of the open site due to enhanced site flexibility and a synergistic effect with the adjacent silanol group.[16]

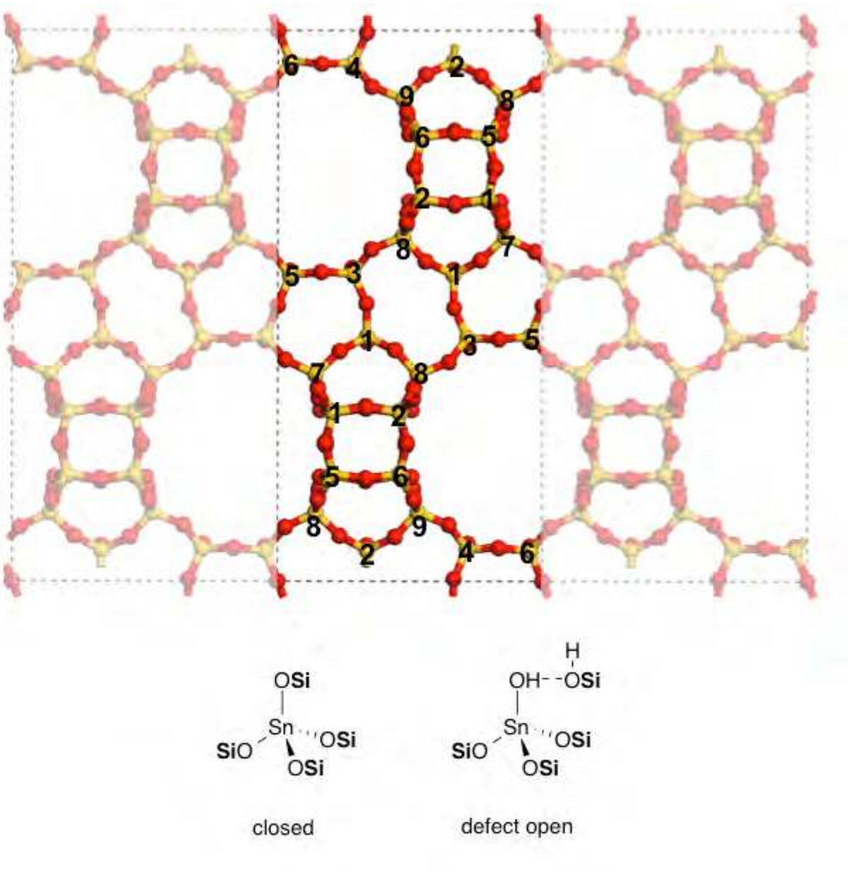

Figure 1. Crystal structure of the BEA zeolite framework with labeling of the distinct T-sites (*top*). The proposed "closed" and "defect-open" Sn(IV)-sites in dehydrated form resulting from substitution of Sn(IV) into a Si(IV) T-site (*bottom*).

More recently Dynamic Nuclear Polarization Enhanced NMR Spectroscopy (DNP-NMR)[17] was shown to be an expedient method to obtain ^{119}Sn NMR signatures of Sn-β zeolites with natural isotopic abundance ^{119}Sn within short acquisition time (minutes to hours).[18] In particular, the significant reduction in experimental time made possible by DNP-NMR allows for recording two dimensional ^{119}Sn magic angle turning (MAT) NMR spectra and thereby obtaining both isotropic ^{119}Sn chemical shifts and ^{119}Sn chemical shift anisotropy (CSA) parameters, which is not possible by conventional solid-state NMR due to the low sensitivity.[18a] Since the CSA is very sensitive to the symmetry and the chemical nature around the tin center, its measurement provides direct information on the Sn-site structure and further insight to the Sn sites in Sn-β zeolites. In particular we have shown that the incorporation of Sn in a post-synthetic approach led to the presence of mainly two isolated Sn sites in hydrated samples with NMR chemical shifts of –659 ppm and –685 ppm, consistent with the presence of two octahedral tin sites in different environments.[18a] It is worth noting that the DNP enhanced ^{119}Sn solid-state NMR spectra of Sn-β prepared *via* direct hydrothermal synthesis showed a distinct resonance at –700 ppm.[18b] Earlier work, using conventional ^{119}Sn solid-state NMR (with ^{119}Sn isotopic labeling), showed isotropic chemical shifts ranging from δ_{iso} = –685 to –736 ppm.[19] The observation of distinct ^{119}Sn chemical shifts in Sn-β prepared by different synthetic routes suggests the presence of different Sn(IV)-sites in the otherwise seemingly similar Sn-β samples.

Sels *et al*. recently presented a detailed experimental study using EXAFS, XANES, UV-Vis and TPR to compare the active sites in post-synthetically grafted Sn-β and hydrothermal Sn-β. A new Sn-site for post-synthetic liquid phase grafted Sn-β was proposed, where the Sn is coordinated with three framework SiO^- and one distant charge-balancing SiO^-.[20] Furthermore, a different T-site occupancy was suggested for post-synthetic Sn-β *vs*. hydrothermal Sn-β. Sn sites in different T-sites could have different electronic properties, site accessibility, and also different proximity to silanol groups, which could all contribute to the catalytic activity.

With the fundamental aim of understanding the differences between various Sn-β catalysts at an atomic level and to correlate the structure of the active sites and the catalytic activity, we prepared Sn-β catalysts by solid-solid ion-exchange from dealuminated β zeolite and by traditional hydrothermal synthesis. Microscopy, powder X-ray diffraction (pXRD) and adsorption isotherms (N_2, Ar, H_2O) were used as complementary characterization techniques. ^{119}Sn and ^{29}Si DNP-NMR, combined with DFT calculations, are used to obtain an atomic description of the surface sites. Correlation between catalytic activity for the aqueous phase glucose-fructose isomerization and the presence of specific sites according to DNP-NMR and DFT calculations allows the construction of a map of spectroscopic signatures of the different tin sites. This enables structure-activity relationship and shows that the most active materials in our series consist of predominantly closed sites in T6 and T5/T7 of a hydrophobic zeolite β framework in the as-synthetized sample.

RESULTS

Catalyst performance and characterization. Sn-β zeolites with metal loadings of 1.0 ± 0.2 wt % were prepared by both hydrothermal synthesis and post-synthetic incorporation into dealuminated β zeolites. Direct hydrothermal synthesis was carried out in fluoride media with and without the use of β zeolite seeds. The seeded sample was formed by adding nano-sized dealuminated β zeolite crystals. Post-synthetic Sn-β samples were prepared starting from two commercial Al-β zeolites, which were synthesized in a hydroxide media, with SiO_2/Al_2O_3 ratios of 25 or 300 (denoted as Sn/deAl-Beta-OH-25 and Sn/deAl-Beta-OH-300, respectively). We also prepared our own Al-β zeolite synthesized in fluoride media with SiO_2/Al_2O_3 ratios of 30 or 400 and then synthesized post-synthetic Sn-β zeolite (denoted as Sn/deAl-Beta-F-30 and Sn/deAl-Beta-F-400, respectively). The materials were tested for the equilibrated isomerization of glucose-to-fructose in water, where Sn-β samples obtained from post-synthetic modification (Table 1, entries 1-4) in general showed a 3-5 times lower initial activity per total amount of Sn compared to the post-synthesis materials (Table 1, entry 5 and 6). The formation of fructose *via* the base-catalyzed enolization pathway by hydroxide ions in solution was excluded performing isotopic tracer studies with D-glucose-d2. All catalysts selectively formed fructose products with the deuterium labeling at the first carbon, indicated by the absence of the ^1H resonance at $\delta = 3.47$ ppm (Figure S1). This unambiguously confirms that fructose is exclusively formed *via* intramolecular 1,2-hydride shift over Lewis acid Sn centers.[21] In agreement, no indication for the presence of interzeolite SnO_2 was found (*vide infra*). Moreover, reacting glucose with dealuminated β zeolite did not show any activity and performing a hot filtration test confirmed the heterogeneous nature of the catalysis, since after removal of the catalyst no further production of fructose was observed. The observation of the different activity per Sn therefore suggests an inherent difference in the physical and/or chemical properties of the Sn-β zeolites prepared *via* the two different methods.

Table 1. Activity and activation energies of different Sn-β zeolites in the aqueous phase isomerization reaction of glucose.[a,f]

Entry	Catalyst[b]	Activity per Sn_{init}[c,d] [h^{-1}]	Fructose Yield[e] [%]	Fructose Selectivity[e] [%]	E_{app}[f] [kcal mol^{-1}]	Pre-exponential factor *A*[f,g]
			Sn-β From Post-Synthetic Incorporation			
1	Sn/deAl-Beta-OH-25	55 ± 12	8	68	23.7 ± 2.8	34.0 ± 3.8
2	Sn/deAl-Beta-OH-300	50 ± 10	8	68	21.4 ± 2.3	30.8 ± 3.2
3	Sn/deAl-Beta-F-30	48 ± 10	9	68	22.2 ± 1.9	32.3 ± 2.6
4	Sn/deAl-Beta-F-400	128 ± 16	21	68	21.3 ± 1.0	32.0 ± 1.4
			Sn-β From Hydrothermal Synthesis			
5	Sn-Beta-seed	280 ± 50	28	67	-	-
6	Sn-Beta	279 ± 32	29	66	21.4 ± 0.9	33.1 ± 1.1

[a] Reaction conditions: 50 mg of catalyst in 5 mL of a 5 wt % aqueous glucose solution (0.3 M) at 100 °C. [b] Sn/deAl-Beta: tin incorporated into dealuminated β by solid-solid ion-exchange; OH: parent Al-Beta zeolite synthesized in hydroxide media; F: parent Al-Beta zeolite synthesized in fluoride media; 25: SiO_2/Al_2O_3 ratio of parent zeolite; Sn-Beta: hydrothermally synthesized Sn-β zeolite; seed: β seed crystals added to the synthesis gel. [c] Defined as the mole product generated per mole Sn per hour calculated at the initial stage of the reaction. [d] Error based on ICP-OES determined Sn-loading. [e] After 1h of reaction. [f] rates are measured in mole product formed per second normalized per total mole metal in the catalyst; temperatures for Arrhenius plot range from 80-110°C (Figure S6). [g] units: (mol · dm^3)(mol Sn · s · mol glucose)$^{-1}$

It was shown that the hydrophobicity of micro- and mesoporous oxides has a strong influence on the efficiency of aqueous phase biomass conversions.[22,23] Therefore, H_2O adsorption isotherms were recorded to measure the hydrophobicity of all the different Sn-β zeolites (Figure 2). Independent of seeding, a Type III adsorption isotherm[24] was observed for both of the Sn-β zeolites prepared *via* direct hydrothermal tin incorporation. On the other hand, the H_2O isotherms for the Sn-β samples prepared from commercial Al-β zeolites (Sn/deAl-Beta-OH-25 and Sn/deAl-Beta-OH-300) showed a Type II adsorption isotherm.[24]

The amount of water adsorbed in both the micro- and mesopores was significantly higher (see Table S1), indicating a more hydrophilic framework, probably associated with the presence of defect sites within the BEA framework (Si-OH groups, see below). In the case of the Sn/deAl-Beta-OH-25, this observation is not surprising since at Sn-loadings of 1 wt%, less than 10% of the vacant T-sites created during dealumination are filled. Parent deAl-Beta-OH-300 can theoretically fit 1.25 wt% of Sn, so ca. 80% of the silanol nests should be closed after tin incorporation. However, very similar H_2O adsorption behavior, especially in the microporous region, was observed for both of the Sn/deAl-Beta-OH zeolites (Figure 2, blue), suggesting that the majority of the hydrophilic defect sites are already present in the parent Al-β zeolites (^{29}Si solid-state NMR confirms this, see below). From literature, it is well known that zeolites synthesized in a fluoride media possess less connectivity defects than those obtained from hydroxide media, resulting in a material with higher hydrophobicity.[25] Indeed the H_2O adsorption isotherms of post-synthetic Sn-β zeolites prepared from Al-β synthesized in fluoride media show a significant improvement in the hydrophobicity of the catalyst (Figure 2, red). As for the hydroxide mediated Sn/deAl-Beta-OH samples, slightly more water was adsorbed at higher relative pressure on the sample with lower SiO_2/Al_2O_3 ratio. This is likely due to silanol nests created during acid treatment of the dealumination step. For the Sn/deAl-Beta-F-400, where all vacant T-sites should be filled with Sn(IV), a Type III adsorption isotherm identical to the ones obtained for the Sn-β zeolites from direct hydrothermal synthesis was observed. The total water uptake per gram of catalyst was determined to be around 5 times lower than for the Sn/deAl-Beta-OH-25. We conclude from these experiments that the post-synthetic Sn/deAl-Beta-F-400 material has very similar hydrophobicity properties to the direct hydrothermal Sn-β samples. Although improved catalytic performance was observed, Sn/deAl-Beta-F-400 did not reach the benchmark activity of the materials obtained through direct incorporation of the metal (Table 1, entries 5 and 6).

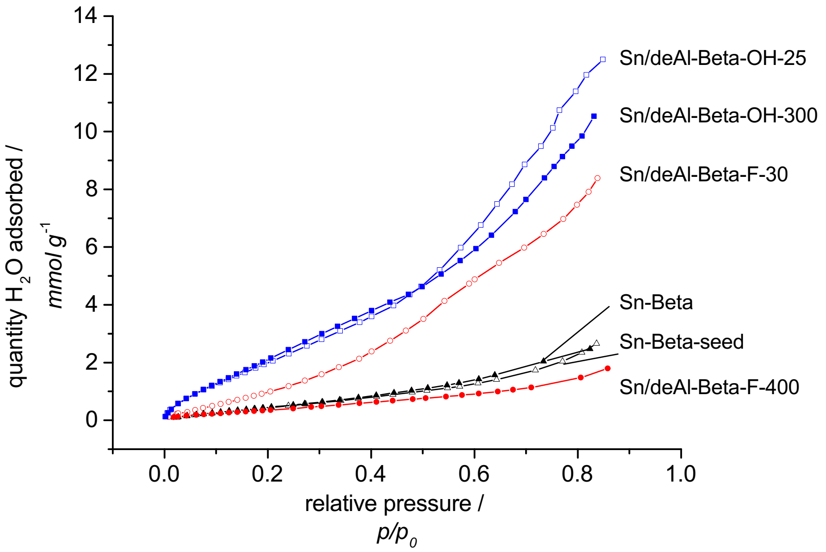

Figure 2. H_2O adsorption isotherms at 298 K for post synthetic Sn-β catalysts obtained from parent zeolites synthesized in hydroxide media (*blue*), post synthetic Sn-β obtained from parent zeolites synthesized in fluoride media (*red*) and Sn-β catalysts prepared *via* traditional hydrothermal synthesis (*black*).

BET areas between 610 and 650 m^2 g^{-1} were obtained from N_2 adsorption measurements at 77 K for all Sn-β samples, except for the Sn/deAl-Beta-F-400 where a BET area of 554 m^2 g^{-1} was obtained. Micropore and mesopore volume, as well as the external surface area, were extracted from the t-method[26] (Table S1). Slightly smaller micropore volume is observed for all post-synthetic materials, while the mesopore volume and the external surface area was higher for the two samples obtained from commercial zeolites and the Sn/deAl-Beta-F-30. The Sn/deAl-Beta-F-400 and both direct hydrothermal Sn-β zeolites exhibit significantly lower external surface area, *i.e.* larger crystal size resulting from retarded crystallization in fluoride mediated synthesis. Scanning Electron Microscopy (SEM) confirmed the difference of one order-of-magnitude in crystal size (Figure S2). To assess the microporosity of the β zeolites more accurately, argon adsorption measurements at 87 K were performed for the different materials. A pore size of 6.2±0.1 Å was determined for both, post-synthetic Sn/deAl-Beta zeolites and hydrothermal Sn-β (Figure S3).

Another possible explanation for the superior catalytic performance of the materials prepared by direct incorporation *vs.* post-synthetic incorporation of the Lewis acid center could be a higher crystallinity of the zeolitic material. Therefore, powder X-ray diffractograms (pXRD) were collected and the degree of crystallinity of the different zeolites was assessed by integration of the d_{302}-reflection at $2\theta = 22.4$ (Table S1). The characteristic powder pattern of the BEA type was observed for all samples (Figure 3). No direct correlation between the crystallinity of the post-synthetic Sn-β catalysts and the activity in the aqueous phase glucose isomerization could be observed. However, a higher crystallinity was detected for the materials known to exhibit less defect sites, *i.e.* those featuring a more hydrophobic framework (*vide supra*).

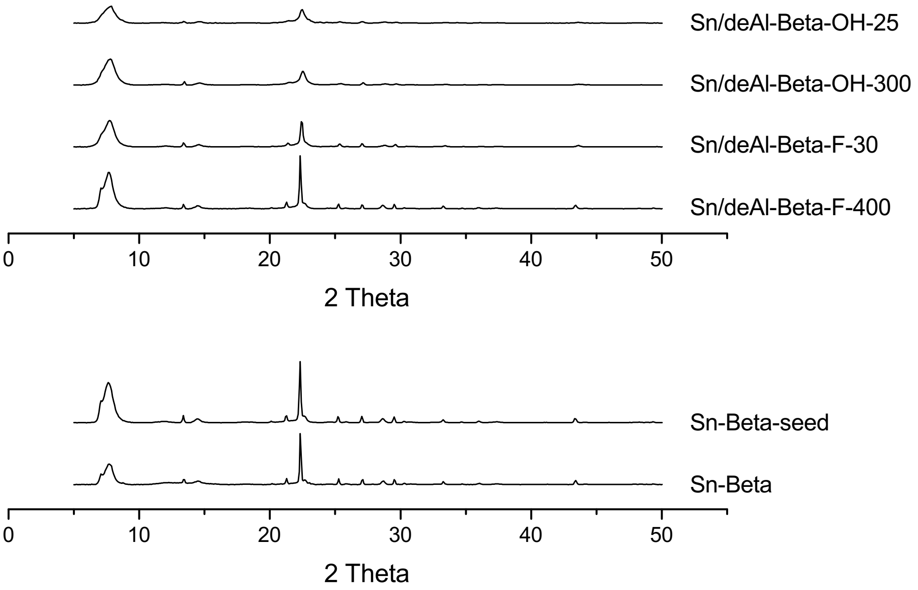

Figure 3. Powder X-ray diffraction patterns obtained for post-synthesis Sn-β (*upper*) and hydrothermal Sn-β catalysts (*lower*).

Considering the physical properties of the Sn-β samples, *i.e.* hydrophobicity, particle size, pore size distribution and crystallinity, one can conclude that when starting from a parent zeolite prepared *via* the fluoride route with a high Si/Al ratio, a post-synthetic Sn-β, *i.e.* Sn/deAl-Beta-F400 can be obtained which is very similar to traditional hydrothermal Sn-β. However, the hydrothermal Sn-β still shows a 2.2 times higher activity than post-synthetic Sn/deAl-Beta-F400 in terms of initial activity per tin in the aqueous phase glucose isomerization. We also evaluated the apparent activation energies for the different Sn-ß samples. Therefore, aqueous phase glucose isomerization reactions were performed at temperatures between 353-383 K allowing measuring activation energies of 21-24 kcal mol^{-1}, in agreement with literature data.[4b] It also confirms that catalytic tests were not run under mass transfer limitations. However, this does not explain the difference by a factor of 2.2 in the activity between the Sn/deAl-Beta-F400 and the two hydrothermal zeolites that have very similar if not identical physicochemical properties. Possible explanations for the difference in activity are site accessibility of the active Sn-site for glucose and a different site distribution in terms of the nature of the active Sn site and the T-site occupancy. The latter results in a different local site geometry and possibly restrictions of bound intermediates and transition states. Recently it was demonstrated that by titrating the active sites in Sn-Beta, the amount of open and closed sites could be quantified.[23] Correlating the number of active sites with the catalytic activity showed that the open sites in Sn-Beta are the dominant active sites for aqueous glucose isomerization. However different hydrophobic Sn-Beta zeolites showed heterogeneity in activity per open Sn site, which has been hypothesized to result from the different local environment of the Sn site (T-site position).[23]

Therefore we first tested the different materials in the aqueous phase glyceraldehyde isomerization where all sites are assumed to be accessible due to the smaller size of the glyceraldehyde molecule compared to the glucose. Similar to glucose, zeolites having a hydrophilic framework showed significant lower activity per Sn for the isomerization of glyceraldehyde to dihydroxyacetone (Table 2, entry 1-3). On the other hand the hydrophobic materials show a more than 5 times higher initial catalytic activity (Table 2 entry 4-6). In contrast to the glucose isomerization the Sn/deAl-Beta-F-400 performs as good as, if not slightly better than, the hydrothermal Sn-Beta. Initial activity per Sn was in general about 3 times higher than for the glucose isomerization. For the Sn/deAl-Beta-F400 the activity per Sn was even 7 times higher for glyceraldehyde compared to glucose isomerization. Thus it is feasible to hypothesize that not all active Sn-sites are accessible for the glucose (as they are for glyceraldehyde).

Table 2. Activity of different Sn-β zeolites in the aqueous phase isomerization reaction of glyceraldehyde[a].

Entry	Catalyst[b]	Activity per Sn_{init}[c,d] [h^{-1}]	DHA Yield[e] [%]	DHA Selectivity[e] [%]
Sn-β From Post-Synthetic Incorporation				
1	Sn/deAl-Beta-OH-25[f]	144 ± 18	13	>99
2	Sn/deAl-Beta-OH-300	122 ± 4	10	>99
3	Sn/deAl-Beta-F-30	156 ± 36	14	>99
4	Sn/deAl-Beta-F-400[f]	868 ± 107	43	95
Sn-β From Hydrothermal Synthesis				
5	Sn-Beta-seed	-	-	-
6	Sn-Beta	764 ± 74	43	98

[a]Reaction conditions: 27 mg of catalyst in 5 mL of a 0.3 M aqueous glyceraldehyde solution at 70 °C. [b]Sn/deAl-Beta: tin incorporated into dealuminated β by solid-solid ion-exchange; OH: parent Al-Beta zeolite synthesized in hydroxide media; F: parent Al-Beta zeolite synthesized in fluoride media; 25: SiO_2/Al_2O_3 ratio of parent zeolite; Sn-Beta: hydrothermally synthesized Sn-β zeolite; seed: β seed crystals added to the synthesis gel. [c]Defined as the mole product generated per mole Sn per hour calculated at the initial stage of the reaction. [d]Error based on ICP-OES determined Sn-loading. [e]After 20 min of reaction. [f] activation energies for this sample can be found in Table S2.

In order to provide an atomic level description of the Sn-β zeolites, *i.e.* to identify the local environment of the Sn sites and to evaluate the corresponding nature of the active sites, we performed NMR measurements of all the synthetized materials. This complements the other physical measurements and catalytic activity data and provides further insights into the differences at atomic level between all the zeolite materials. For this purpose, ^{29}Si and ^{119}Sn DNP NMR experiments were performed to investigate the molecular structure of the Sn(IV) centers. Incipient wetness impregnation with a tetrachloroethane (TCE) solution of a stable bulky 2,6-spirocyclohexyl nitroxide derivative,[28] here TEKPol,[29] was used to prepare the Sn-β samples for the DNP experiments. Since the pores of Sn-β are ca. 6 Å (*vide supra*), the TEKPol radicals do not enter the pores of the material, and hence they do not directly interact with the Sn(IV)-sites. Instead, DNP enhances the polarization of the ^1H nuclei of adsorbed water and TCE molecules near the surface of the zeolite particles. The enhanced ^{1}H polarization at the surface of the particles is then relayed into the interior of the zeolite particles by ^{1}H spin diffusion amongst the ^{1}H nuclei of the TCE and the absorbed water (from ambient moisture) that fills the pores.[18,28a,30] The DNP enhanced ^{1}H polarization can then be transferred to hetero-nuclei such as ^{119}Sn or ^{29}Si by conventional ^{1}H-X cross polarization (CP)[31] experiments. DNP signal enhancements of 10-200 can typically be realized in this way, resulting in a dramatic reduction in experiment time and allowing natural isotopic abundance ^{119}Sn NMR experiments at low Sn loadings.

DNP enhanced ^{29}Si and ^{119}Sn cross-polarization magic-angle spinning (CPMAS) NMR spectra were collected for all of the different Sn-β catalysts (Figure 4). We note that ^{29}Si solid-state NMR experiments are useful to understand how DNP and spin diffusion proceed in the zeolites. ^{29}Si NMR spectra allow the proton DNP enhancement *inside the pores of the zeolite* to be measured, since ^{29}Si CPMAS provides enough sensitivity to acquire a reference NMR spectrum without DNP. On the other hand, direct measurement of the ^{1}H DNP enhancements (ε_{H}) by ^{1}H solid-state NMR provides a measure of the DNP enhancement wherever the impregnating solvent is located, in this case inside and outside the pores. Therefore, during the process of optimizing sample preparation for DNP, the DNP enhancement inside the pores of the zeolite should be measured by ^{29}Si CPMAS experiments, rather than relying upon direct measurements of proton DNP enhancements. Since ^{1}H spin diffusion transports DNP enhanced ^{1}H polarization into the zeolite smaller zeolite particles should yield the highest $\varepsilon_{Si\ CP}$.[30a,30b] However there are many factors which influence the absolute DNP enhancement such, hydration level, dielectric properties and degree of de-oxygenation, therefore, we do not observe a strong correlation between particle size and the observed $\varepsilon_{Si\ CP}$.

The ^{29}Si DNP SENS spectra corroborate the results obtained by H_2O adsorption and pXRD. The ^{29}Si DNP NMR spectra of the different Sn-β catalysts show Q_3 [$(SiO)_3$**Si**OH] and Q_4 [$(SiO)_4$**Si**] Si(IV)-sites with characteristic ^{29}Si isotropic chemical shifts centered around δ_{iso} = –104 and –115 ppm, respectively. Q_3 sites correspond to defect sites in the material, *i.e.* hydroxylated Si(IV) sites that are only partially bound to the zeolite framework. The ^{29}Si DNP SENS spectra of both the post-synthetic Sn-β's prepared in hydroxide media and the post-synthetic Sn/deAl-Beta-F-30 prepared in fluoride media (where there is not enough Sn(IV) to fill the vacant silanol nests), show very intense Q_3 [$(SiO)_3SiOH$] peaks. This is consistent with the pXRD and H_2O adsorption measurements indicating that these materials are the most defected and hydrophilic, respectively. For the post-synthetic Sn/deAl-Beta-F-400 Sn-β there are few, if any, defect sites present in the parent zeolite, and all of the created T-site vacancies are filled with tin. In this case, little or no Q_3 sites were observed in the ^{29}Si NMR spectra. The same is true for the Sn-β prepared *via* hydrothermal synthesis where Q_3 ^{29}Si NMR signals are weak or absent. This is consistent with the high degree of crystallinity and hydrophobicity of these Sn-β samples.

DNP enables the rapid acquisition of ^{119}Sn solid-state NMR spectra and can be used to probe the structure of the tin sites in order to understand the molecular level origin of the activity differences amongst the different Sn-β. 2D ^{119}Sn DNP-NMR magic angle turning (MAT) spectra of the different hydrated Sn-β catalysts were acquired (Figures S10-S14) in order to measure both isotropic Sn chemical shifts and Sn chemical shift tensors. Projections of the indirect isotropic dimension of the DNP enhanced ^{119}Sn MAT NMR spectra (which only show isotropic Sn chemical shifts, i.e., spinning sidebands are absent) are shown in Figure 4.

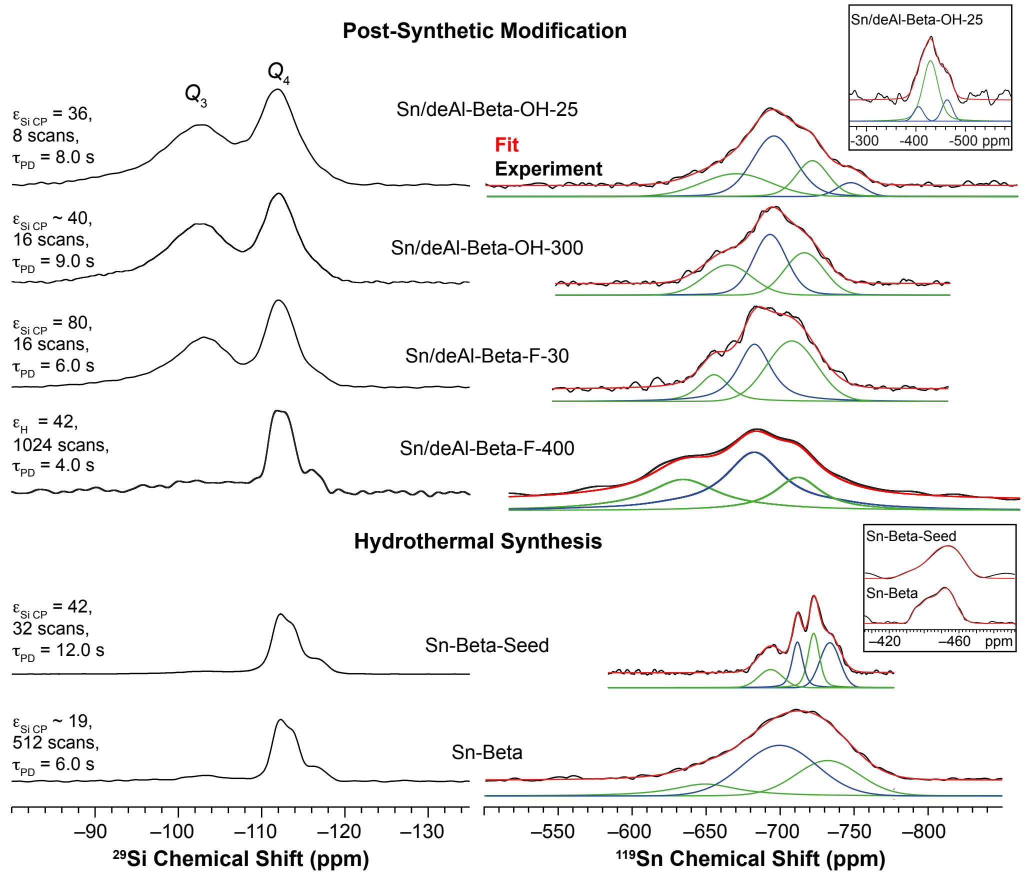

Figure 4. 9.4 T 105 K ^{1}H-^{29}Si (left) DNP-NMR magic-angle spinning cross-polarization spin echo spectra and the 1D projections of ^{1}H-^{119}Sn (right) DNP-NMR cross-polarization magic-angle turning spectra (see Figure S9-S13) of various Sn-β catalysts in the hydrated form. For the Sn/deAl-Beta-F-400 a ^{1}H-^{119}Sn cross-polarization spectra with total suppression of spinning sidebands (TOSS)[32] is shown. ^{1}H-^{119}Sn DNP-NMR magic-angle spinning cross-polarization spin echo spectra of dehydrated Sn/deAl-Beta-OH-25 and both hydrothermal Sn-β samples are shown in the insets.

The projections were fit with simple mixed Gaussian/Lorentzian lineshapes in order to determine distinct isotropic chemical shifts (δ_{iso}). Table 3 summarizes the chemical shifts at the center of each peak and their relative integrated intensities. To evaluate how quantitative are the DNP enhanced ^{119}Sn solid-state NMR spectra and that relative integrated intensity are not affected by the DNP enhancements we performed experiments on Sn/deAl-Beta-OH-25 with variable polarization delays and variable CP contact times. DNP enhanced ^{119}Sn CPMAS spectra acquired with polarization delays ranging from 2 to

30 seconds (Figure S7) show that the relative intensities within the ^{119}Sn NMR spectrum are constant. This suggests that the DNP enhancements for all Sn sites are similar; sites with higher DNP enhancements should be characterized by faster signal build-ups since they would reside closer to the polarizing agents at the surface of the zeolite particles. DNP enhanced ^{119}Sn NMR acquired with variable CP contact times (0.5 ms to 8 ms, Figure S8) show that the relative intensities in the ^{119}Sn NMR spectra are constant. These experiments suggest that intensities observed in the DNP enhanced ^{119}Sn CPMAS spectra are pseudo-quantitative since all ^{119}Sn sites exhibit the same CP dynamics and signal build-up rates, and suggest that the integrated intensities in Table 3 are not substantially biased.

The corresponding chemical shift (CS) tensor parameters[33] for each isotropic shift were obtained from 2D magic angle turning (MAT) experiments. For Sn/deAl-Beta-F-400, MAT experiments were not collected, since poor sensitivity prevented the acquisition of a 2D MAT spectrum in a reasonable experiment time. The poor sensitivity likely arises from a low DNP enhancement, which is caused by the larger zeolite particle size (as confirmed by SEM, see Figure S2). However, for hydrothermal synthesized Sn-β catalysts, which possess a similar crystal size to Sn/deAl-Beta-F-400, sensitivity of the DNP enhanced ^{119}Sn NMR experiments was good enough to allow rapid acquisition of MAT spectra, which suggests that the Sn indirect DNP enhancements were high. Therefore we hypothesize that a difference in the spatial distribution of the Sn centers within the zeolite crystal is causing the lower sensitivity. Tolborg *et al.* recently showed that tin is preferentially located in the outer rim of Sn-β zeolite crystals prepared by hydrothermal synthesis.[27] A more uniform distribution in Sn/deAl-Beta-F-400 could explain the lower DNP enhancement due to a longer diffusion length into the crystal to polarize the Sn-site (see SEM-EDX of Sn/deAl-Beta-F-400 in Figure S4).

Table 3. ^{119}Sn solid-state NMR signatures of the different Sn-β catalysts prepared by different synthetic methods.

δ_{iso} (ppm)	Ω (ppm)	κ(-)	Peak width at half height (ppm)	Relative intensity (%)
Sn/deAl-Beta-OH-25 (dehydrated)				
–464	–	–	25	17
–430	–	–	37	71
–405	–	–	23	11
Sn/deAl- Beta-OH-25 (hydrated)[a]				
–748[b]	–	–	22	6
–722	114	0.4	26	21
–696	124	0.2	34	47
–670	131	0.1	55	26
Sn/deAl- Beta-OH-300 (hydrated)				
–716	141	0.1	31	32
–693	133	0.2	27	41
–664	129	0.2	38	27
Sn/deAl- Beta-F-30 (hydrated)				
–708	126	0.1	40	47
–683	139	0.0	27	38
–655	140	0.0	24	15
Sn/deAl- Beta-F-400 (hydrated)				
–716	–	–	64	27
–689	–	–	59	43
–653	–	–	63	30
Sn-Beta-seed (dehydrated)				
–460	–	–	12	14
–451	–	–	20	78
–432	–	–	13	8
Sn-Beta-seed (hydrated)				
–734	127	–0.2	16	25
–723	127	0.1	9	30
–712	121	0.1	9	24
–693	158	0.6	20	22
Sn-Beta (dehydrated)				
–452	117	–0.3	13	66
–445	101	–0.9	10	29
–435	115	–0.3	5	5
Sn-Beta (hydrated)				
–732	115	–0.1	51	32
–700	132	0	49	52
–649	139	0.2	53	16

[a] Remeasured sample from reference 18a stored under ambient conditions for 2 years. [b] Fitting of the CS tensor not possible due to weak signal.

For all tested materials no SnO_2, associated with a ^{119}Sn signal at –600 ppm, was detected by ^{119}Sn NMR, which is consistent with the UV-Vis of all materials (Figure S5). For post-synthetic Sn/deAl-Beta zeolites in all cases the ^{119}Sn MAS spectra could satisfactorily fit with a maximum of four distinct Sn-sites (Table 3) and the most intense ^{119}Sn NMR resonances were centered around –680 to –690 ppm. The ^{119}Sn DNP SENS CP-TOSS spectrum of the dehydrated Sn/deAl-Beta-OH-25 was also acquired. ^{119}Sn NMR chemical shifts characteristic of the dehydrated four fold coordinated Sn sites in Sn-β were observed. It is important to note that the DNP enhanced ^{119}Sn CP spin echo showed substantial intensity ranging from a chemical shift of –380 ppm to –780 ppm (Figure S15), indicating that not all adsorbed water molecules could be removed although the sample was dehydrated at 500°C over night under high vacuum (10^{-5} mbar). This observation is consistent with the higher hydrophilicity of Sn/deAl-Beta-OH-25 in comparison to hydrothermal Sn-β samples and was also observed for post-synthetic Sn-β prepared via liquid phase grafting.[20] Moreover, a chemical shift of –560 ppm was observed, consistent with the presence of penta-coordinated Sn and a mono-hydrated species as proposed by Hwang *et al.* in a recent study[15] and further supported by our calculations (*vide infra* and Figure S29).

In the case of the hydrothermal Sn-β the ^{119}Sn resonances are clearly shifted to lower chemical shifts. Fits of the ^{119}Sn DNP NMR spectra yielded three to four distinct Sn(IV) sites with δ_{iso} as low as –734 ppm. For the two hydrothermally synthesized samples Sn-Beta-seed and Sn-Beta, ^{119}Sn DNP NMR spectra of the corresponding dehydrated materials were also acquired. The spectra of the dehydrated materials show peaks covering a shift range of ca. –430 and –465 ppm, in agreement with previous studies (inset, Figure 4 and Figure S14).[19,34] Similar to the hydrated samples, the center of the ^{119}Sn NMR resonances of hydrothermal Sn-β zeolites are shifted upfield (–450 ppm) compared to post-synthetic Sn/deAl-Beta-OH-25 were highest intensity was observed around –430 ppm.

Comparing the isotropic ^{119}Sn DNP SENS spectra of the different hydrated Sn-β zeolites, the differences in Sn chemical shifts most likely reflect (*i*) substitution of Sn(IV) in different T-sites of the zeolite framework (Figure 1, top), and/or (*ii*) the presence of closed and/or open Sn(IV)-sites (Figure 1, bottom), which could also explain the difference in activity. Combining the catalytic data in Table 1 with the insights obtained from various characterization techniques leads us to conclude that the Sn(IV)-site giving rise to ^{119}Sn isotropic chemical shifts around –730 ppm in combination with a hydrophobic zeolite framework are most likely provide highest activity for the glucose-to-fructose isomerization.

Computational modeling and Calculated Chemical Shift Map of Sn(IV)-sites in Sn-β. To corroborate on our hypothesis that the Sn(IV)-sites (closed or open) are located in different T-sites in the different zeolite samples, computational modeling based on Density Functional Theory (DFT) was performed. DFT has been extensively used to study structures and reactivity of Sn-β and similar zeolites.[10,14,35] Structures, relative energies, and the spectroscopic signatures such as the ^{119}Sn NMR parameters of Sn(IV)-sites in Sn-β were calculated using cluster models for all proposed T-sites at different hydration levels in order to relate a structure to specific isotropic chemical shift and chemical shift tensors, which were measured experimentally.

Models of T-sites in Sn-β zeolite. The starting structure of the model catalyst is the polymorph A of zeolite β (framework type BEA).[36] In this structure, there are nine unique crystallographic lattice positions for Si(IV), referred to as T1-T9 sites (see Figure 1, top). It is important to note that the BEA topology is a mixture of the two polymorphs A and B. The difference in the two polymorphs results from the stacking of the same building layer.[37] Thus, we only expect minor changes in the local geometry of the Sn within the different polymorphs and performed the calculations exclusively on polymorph A. In order to assign the experimentally observed ^{119}Sn NMR spectra, five different cluster models were constructed from the experimentally determined X-Ray structure zeolite β.[36a] These five models represent the structures corresponding to the nine T-sites, where sites T1/T2, T3/T4, T5/T6 and T7/T8 share the same cluster, with 108, 121, 131 and 128 atoms, respectively. The cluster model for T9 is unique, with 98 atoms. In order to construct Sn(IV) sites in these clusters, the Si atom of a particular T-site was substituted by Sn, giving rise to the nine Sn-β cluster models. In the construction of the clusters all the rings that are part of the evaluated T-site have been included, whereas the dangling bonds that connect the Si atoms to the rest of the zeolite framework were saturated with H-atoms. The models with Sn bonded to four OSi groups correspond to closed sites (**Tn**^{c}). We also consider sites where one Si atom is substituted by Sn and an adjacent Si atom is removed, which results in the presence of dangling O-atoms terminated with H (see Figure 5), referred to hereafter as defect-open sites (**Tn**^{o}).[35d,35e] Hydrated closed (**Tn**^{C1h}, **Tn**^{C2h}, **Tn**^{C3h}) and defect-open sites (**Tn**^{O2h}, **Tn**^{O3h}) were modeled by coordinating one or two water molecules to Sn, and with a third water molecule in the second coordination sphere, as shown in Schemes 1a and 1b for closed and defect-open sites, respectively.

Alternative structures, corresponding to open sites created by hydrolysis of framework Sn-O bonds in doubly- and triply-hydrated closed sites were also considered. Two types of hydrolyzed-open sites can be envisioned: in Type I (Scheme 1c, **Tn**$^{H\text{-}I\text{-}3h}$) a water molecule in the second coordination sphere of tin breaks a Sn-O bond, leading to one Si-OH and one Sn-OH group interacting with each other, while the Sn(IV) remains coordinated to two water molecules. In Type II (Scheme 1d, **Tn**$^{H\text{-}II\text{-}a/b\text{-}2/3h}$), the reaction of coordinated water molecules on Si-O-Sn generates a Si(OH)Sn bridge and a terminal Sn(OH). Up to two water molecules can be split. Hydrolyzed-open sites of type I (Scheme 1c) were studied for all nine T-sites, while hydrolyzed-open sites of Type II (Scheme 1d) were only evaluated for T1, T5 and T9 sites. We also studied some structures where Sn is in a penta-coordinated (**Tn**^{p}) environment with two bridging OH groups between Sn and a neighboring Si, that is, $Sn(\mu\text{-}OH)_2\text{-}Si$, as recently proposed (Scheme 1e).[38] These sites can result from the splitting of the water molecule in the Sn-O-Si group in mono-hydrated sites (**Tn**^{C1h}). As for Type II hydrolyzed sites, only T1, T5 and T9 were considered for these sites.

Structures of dehydrated and hydrated closed and defect-open T-sites. The optimized structures and geometrical parameters (in terms of average values) of all nine dehydrated closed (hereafter **Tn**^{c}) and defect-open T-sites (hereafter **Tn**^{o}) can be found in Figures S17-S18 and Table S3. As an example, Figure 5a shows the optimized structures of the T9 site, in the closed and defect-open forms. Similar geometries are found for other sites. All the sites present a distorted-tetrahedral tin coordination environment. In the case of the closed sites the average Sn-O distances range between 1.886 and 1.895 Å, which is in very good agreement with the Sn-O distance obtained from EXAFS experiments.[10] The six O-Sn-O angles vary from 102.0° to 113.8°, with an average value of 109.5°. The dehydrated defect-open sites also present average O-Sn-O angles of *ca*. 109°, similar to what was found for the closed sites, and the Sn-OH average distances range from 1.886 to 1.923 Å.

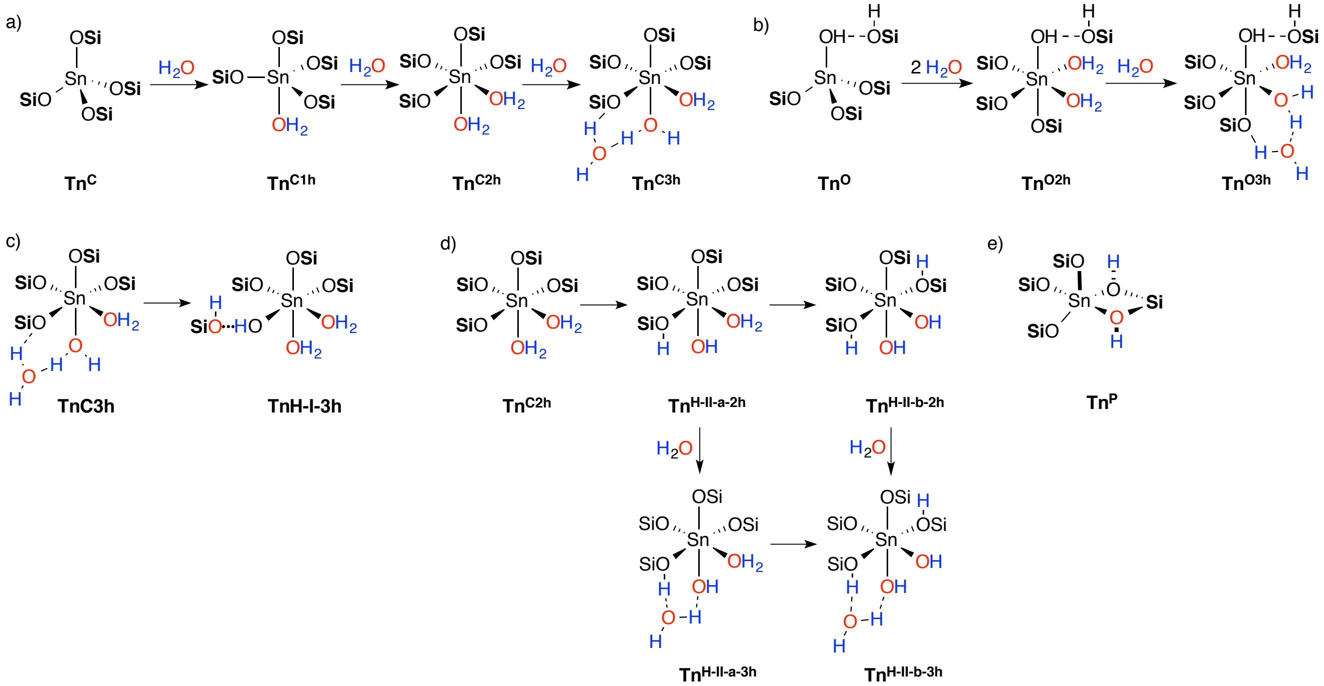

Scheme 1. Formation of hydrated species for a) closed sites; b) defect-open sites; c) hydrolyzed-open sites of type I, d) hydrolyzed-open sites of type II and e) penta-coordinated sites with a bridging OH group in Sn-β. All of the Si atoms are bound to three O atoms of the zeolite framework, however, for clarity connections to the framework are not shown.

The average values of the main geometrical parameters of the hydrated closed and defect-open sites are presented in Tables S3-S7, while Figures S19-S23 show the optimized geometries of all sites in the hydrated form. The optimized structures of the triply-hydrated closed and defect-open T9 site are shown in Figure 5b as an example. While for mono-hydrated sites the geometry around tin corresponds to a distorted trigonal bi-pyramid (TBP, Figure S18), doubly-hydrated closed sites exhibit a geometry at the Sn(IV)-site that corresponds to a distorted octahedron. The coordination of two water molecules increases the Sn-O bond distances to average values between 1.931 and 1.950 Å, while the average values the O-Sn-O angles of framework O atoms in *cis* position range between 96.3-99.8°, and the O-Sn-O^w angles (O and O^w are framework and water oxygen atoms in *trans* position, respectively) vary from 166.3 to 175.5°. The presence of a third water molecule in the second coordination only slightly increases the Sn-O bond distances to values between 1.939 and 1.960 Å (Table S6).

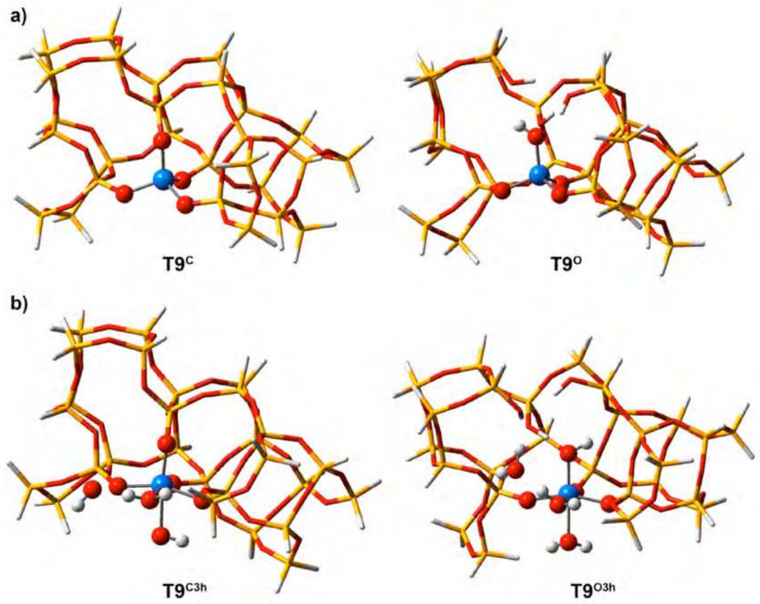

Figure 5. Optimized structures of a) dehydrated closed and defect-open T9 site and b) triply-hydrated closed and defect-open T9 site of Sn-β. The Sn atom and its first coordination sphere are highlighted with balls and sticks models. Sn atoms are shown in blue, oxygen in red, silicon in yellow and hydrogen in white.

Coordination of two water ligands to defect-open sites increases the Sn-OH bond to values in the range 1.925-1.990 Å, and the Sn-O bond distances to values between 1.935 and 1.959 Å, similar to what was found for closed sites species (Table S7). The average O-Sn-O angles for framework oxygen atoms in *cis* position range between 96.8 and 100.7°. The presence of a third water molecule in the second coordination sphere of Sn causes only minor variations to the optimized parameters of the double-hydrated defect sites (Table S8).

Stabilities of T-sites in Sn-β. The relative stability of all nine T-sites was obtained by comparing the energy of substituting one Si atom by Sn at a specific T-site in all nine clusters in the dehydrated closed form. The results are shown in Table S9. In summary, the most stable site for substitution is T1, however, the relative stability of most sites with respect to T1 is within 1-4 kcal·mol^{-1}, indicating that there is not a very strong thermodynamic bias for a preferred location for the Sn substitution. However, the preference of substitution can also be influenced by kinetic factors, which have not been considered in the calculations. We also evaluated the reaction free energies (ΔG_{ads}) for the adsorption of water on the T-sites, which was calculated according to equation 4:

$$\Delta G_{\mathrm{ads}} = G(\mathrm{Tn{-}(H_2O)_x}) - G(\mathrm{Tn}) - \mathrm{x}G(\mathrm{H_2O}) \qquad (1)$$

where Tn–$(H_2O)_x$ corresponds to the adduct between the Tn-site of the zeolite and x molecules of water (either as coordinated water molecule or split over a Sn-O bond, x= 1, 2, 3), and Tn and H_2O refer to the corresponding isolated Tn-site cluster model and the water molecule, respectively.

The free energies for adsorption of water at all T-sites are given in Table 4. According to these results, the adsorption of one water molecule (**Tn**$^{\mathrm{C1h}}$, x= 1) by any closed T-site is favorable, with the reaction free energies ranging from –9.6 to –1.9 kcal · mol^{-1}. Adsorption of two (**Tn**$^{\mathrm{C2h}}$, x= 2) and three water molecules (**Tn**$^{\mathrm{C3h}}$, x= 3) is even more favorable at all sites. In the latter case ΔG_{ads} ranges from –24.3 to –12.5 kcal · mol^{-1}. In general, thermodynamics points toward the formation of hydrated species on the Sn(IV)-sites by coordination of two water molecules as previously proposed,[2b,19,34,39] with a third water molecule in the second coordination sphere involved in H-bonding with the other water molecules. ΔG_{ads} for defect-open sites **Tn**$^{\mathrm{O2h}}$ and **Tn**$^{\mathrm{O3h}}$ in Sn-β are also shown in Table 4. The adsorption of two water molecules is favorable for all defect-open sites, and, in general, for these species the coordination of water molecules to Sn(IV) is more exoergic compared to the corresponding closed sites, except for **T2**. The presence of a third water molecule in the second coordination sphere of tin increases the stability of all species, similar to the effect already observed for closed sites, and the adsorption of three water molecules becomes more exoergic than the similar process for closed sites (compare **Tn**^{C3h} and **Tn**^{O3h} columns in Table 4). The most favorable adsorption of water molecules by the acidic defective open Sn(IV)-sites compared to closed ones is in agreement with previous theoretical results for the adsorption of CH_3CN at T1, T5 and T9 sites in Sn-β.[14]

Table 4. ΔG_{ads} of various Sn(IV)-sites in both closed (x= 1, 2, 3) and open sites (x = 2, 3) of Sn-β, calculated using equation 4. Energies are given in kcal·mol^{-1}

Site	Closed sites			Open sites						
	Tn^{C1h}	Tn^{C2h}	Tn^{C3h}	Tn^{O2h}	Tn^{O3h}	Tn$^{H\text{-}I\text{-}3h}$	Tn$^{H\text{-}II\text{-}a\text{-}2h}$	Tn$^{H\text{-}II\text{-}a\text{-}3h}$	Tn$^{H\text{-}II\text{-}b\text{-}2h}$	Tn$^{H\text{-}II\text{-}b\text{-}3h}$
T1	–3.7	–10.6	–13.3	–18.1	–29.6	18.6	–1.7	–9.5	12.1	4.8
T2	–5.6	–10.3	–16.2	–6.7	–30.1	17.3				
T3	–4.3	–5.1	–12.5	–14.9	–22.8	–3.4				
T4	–8.3	–14.0	–22.3	–14.1	–25.5	–8.3				
T5	–4.4	–11.7	–21.5	–20.9	–26.7	–13.5	–6.7	–11.6	0.5	–2.5
T6	–9.6	–17.2	–24.3	–26.2	–24.6	–6.3				
T7	–8.8	–15.3	–21.6	–19.0	–22.4	–6.2				
T8	–5.0	–15.5	–19.6	–16.5	–23.6	–0.9				
T9	–1.9	–11.9	–17.4	–16.0	–25.7	–8.3	–3.5	–10.1	0.0	0.2

For hydrolyzed-open sites of Type I (**Tn**$^{H\text{-}I\text{-}3h}$; Scheme 1c), ΔG_{ads} is reported in Table 4. Except for the **T1**$^{H\text{-}I\text{-}3h}$ and **T2**$^{H\text{-}I\text{-}3h}$ sites, the formation of these hydrolyzed-open sites is exoergic, ranging from –13.5 to –0.9 kcal · mol^{-1} with respect to separate reactants, although the formation of these hydrolyzed-open sites is always endoergic when compared to the corresponding triply-hydrated closed sites (**Tn**^{C3h}). For hydrolyzed-open sites of Type II (**Tn**$^{H\text{-}II}$ in Scheme 1d), we observed that the splitting of one water molecule in **Tn**$^{H\text{-}II\text{-}a\text{-}2h}$ and **Tn**$^{H\text{-}II\text{-}a\text{-}3h}$ sites is still favorable, but the splitting of the second water molecule in **Tn**$^{\text{H-II-b-2h}}$ and **Tn**$^{\text{H-II-b-3h}}$ sites makes the process thermodynamically unfavorable with respect to separate reactants (only **T5**$^{\text{H-II-b-3h}}$ is slightly exoergic).

^{119}Sn NMR calculations. In order to shed light on the local environment of the Sn(IV)-sites in Sn-β, ^{119}Sn NMR calculations at the B3LYP-D3/TZP level of theory, including relativistic effects (RE) and spin-orbit coupling (SOC), of all sites in both dehydrated and hydrated forms were performed. The chemical shift (CS) tensor is often parameterized with the following equations (2)-(4):

$$\delta_{\mathrm{iso}} = (\delta_{11} + \delta_{22} + \delta_{33})/3 \qquad (2)$$

$$\Omega = \delta_{11}\text{-}\delta_{33} \qquad (3)$$

$$\kappa = 3\left(\delta_{22}\text{-}\delta_{\mathrm{iso}}\right)/\Omega \qquad (4)$$

where $\delta_{11} \geq \delta_{22} \geq \delta_{33}$ are the principal components of the chemical shift tensor.

The isotropic chemical shift (δiso) is the average of the three principal components of the CS tensor and corresponds to the chemical shift that is observed in solution NMR spectroscopy. The span (Ω) describes the magnitude of the chemical shift anisotropy (CSA). The skew (ϰ) describes the axial symmetry of the chemical shift tensor, with extreme values (±1) reflecting the presence of rotational axes at the nuclear site. The computational calculations of the CS tensors of Sn(IV) sites allow us to calculate the CS tensor parameters through equations (2)-(4). Plotting the ^{119}Sn isotropic chemical shift (δiso) against the span (Ω) for all calculated sites allows us to correlate the experimentally determined ^{119}Sn NMR signatures (Table 3) with our computational predictions (Figure 6). Only triply-hydrated sites are shown in Figure 6; the data for the doubly-hydrated Sn-sites are given in Figure S28.

Dehydrated and hydrated closed and defect-open T-sites. Figure 6a shows the relationship between the calculated δ_{iso} and Ω for all dehydrated sites, including closed and defect-open T-sites, as well as the experimentally determined CSA for Sn-Beta-seed zeolites. For the closed sites (in olive green), δ_{iso} varies from –452 to –421 ppm (**T6**^{c} and **T9**^{c}, respectively), with Ω ranging from 97 to 157 ppm (**T6**^{c} and **T2**^{c}, respectively). The dehydrated defect-open sites (in orange) show δ_{iso} ranging between –417 and –375 ppm (**T9**^{o} and **T2**^{o}, respectively) with Ω varying between 101 and 361 ppm (**T9**^{o} and **T1**^{o}, respectively). Interestingly, all closed sites show δ_{iso} that are always below –420 ppm, while δ_{iso} for all open sites are above this value. One can already see that most observed sites have δ_{iso} compatible with closed sites rather than most defect-open sites in their dehydrated form, with exception of **T3**^{o}, and **T7**^{o}-**T9**^{o}, in particular **T9**^{o}, which has calculated CS parameters close to those of some of the closed sites.

Mono-hydrated closed sites show ^{119}Sn δ_{iso} ranging from –586 to –558 ppm, with Ω ranging between 361 and 422 ppm. These predicted CS parameters are significantly different from the experimental data on hydrated and fully dehydrated samples of Sn-β (see Figure S29), but δ_{iso} match very well the experimental signal found at –560 ppm in partially hydrated samples.[15]

The results for penta-coordinated sites with two bridging OH groups, Sn(μ-OH)$_2$-Si (Scheme 1e), are shown in Figure S29. The calculated ^{119}Sn NMR signatures for penta-coordinated Sn-sites (**Tn**^{p}) are very different to any of the collected experimental data (especially the very high calculated span of more than 400 ppm). Therefore we can exclude the presence of this type of sites in our as synthesized hydrated Sn-β samples. Calculated CS tensor parameters for doubly- and triply-hydrated closed sites are presented in Figures S28a and 6b, respectively, and most of them display calculated ^{119}Sn CS tensor parameters that are close to experimental data.

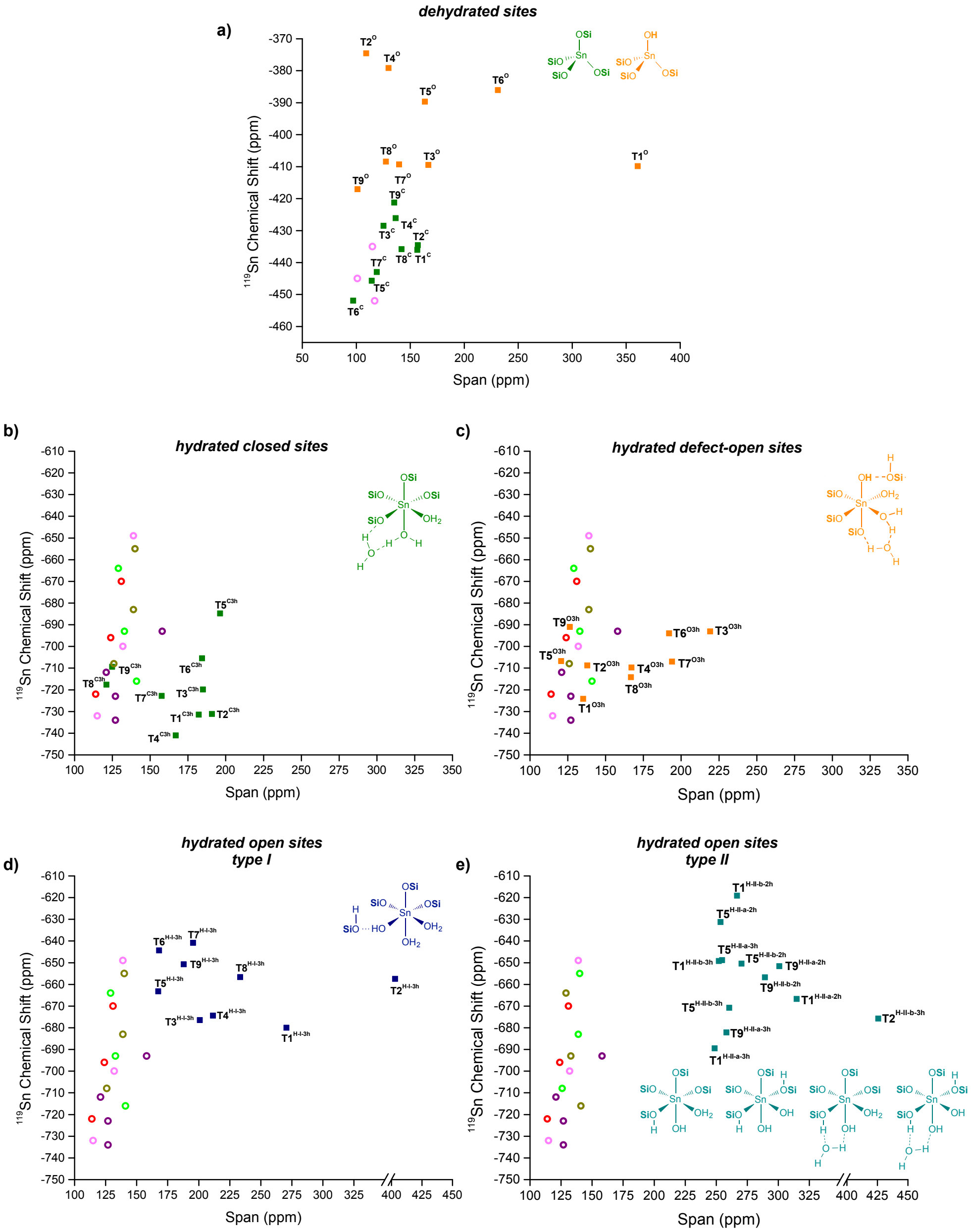

Figure 6. Comparison of measured and calculated ^{119}Sn NMR chemical shifts *vs*. spans. Calculations for a) dehydrated closed Tn^{c} (🟩) and defect-open sites Tn^{o} (🟧); b) triply-hydrated Tn^{C3h} closed sites (🟩); c) triply-hydrated Tn^{O3h} defect-open sites (🟧); d) hydrolyzed-open sites of type I (🟦) and e) hydrolyzed-open sites of type II (■) of Sn-β. Experimental data for dehydrated Sn-Beta (○) is shown in a); hydrated Sn/deAl-Beta-OH-25 (○) Sn/deAl-Beta-OH-300 (○), Sn/deAl-Beta-F-30 (○), Sn-Beta-seed (○) and Sn-Beta (○) in b)-e).

Doubly-hydrated sites (Figure S28a, in blue) have calculated δ_{iso} ranging from –719 to –658 ppm (**T1**$^{\mathrm{C2h}}$ and **T5**$^{\mathrm{C2h}}$, respectively), with Ω varying from 165 to 255 ppm (**T8**$^{\mathrm{C2h}}$ and **T3**$^{\mathrm{C2h}}$, respectively). Including one water molecule in the second coordination sphere of tin, *i.e.* a triply-hydrated site (Figure 6b, in olive green), results in a decrease of both δ_{iso} and Ω, so that δ_{iso} varies from –741 to –684 ppm (**T4**$^{\mathrm{C3h}}$ and **T5**$^{\mathrm{C3h}}$, respectively), while Ω varies from 121 to 196 ppm (**T8**$^{\mathrm{C3h}}$ and **T5**$^{\mathrm{C3h}}$, respectively).

The results for hydrated defect-open sites are shown in Figures S28b and 6c (data in magenta and orange for **Tn**$^{\mathrm{O2h}}$ and **Tn**$^{\mathrm{O3h}}$, respectively). For **Tn**$^{\mathrm{O2h}}$ sites δ_{iso} ranges from –696 to –663 ppm (**T8**$^{\mathrm{O2h}}$ and **T2**$^{\mathrm{O2h}}$, respectively), whereas Ω ranges from 150 and 254 ppm (**T9**$^{\mathrm{O2h}}$ and **T3**$^{\mathrm{O2h}}$, respectively). Similar to the triply-hydrated closed sites, triply-hydrated defect-open sites (**Tn**$^{\mathrm{O3h}}$) also show ^{119}Sn NMR parameters that are, in general, lower in both δ_{iso} and Ω with respect to the doubly-hydrated ones. The δ_{iso} for these sites ranges from –724 to –691 ppm (**T1**$^{\mathrm{O3h}}$ and **T9**$^{\mathrm{O3h}}$, respectively), whereas Ω ranges from 121 and 219 ppm (**T5**$^{\mathrm{O3h}}$ and **T3**$^{\mathrm{O3h}}$, respectively). We showed above that the presence of the surrounding water molecule has a strong effect on the thermodynamic stability of the different closed and defect-open sites, indicating that triply-hydrated species are more stable than mono- and double-hydrated ones. Therefore, it is expected that the different signatures for hydrated samples correspond to mainly triply-hydrated sites.

Figures 6d-e show the ^{119}Sn NMR signatures of the hydrolyzed-open sites of Type I and II. The **Tn**$^{\mathrm{H\text{-}I\text{-}3h}}$ sites (Figure 6d) shows δ_{iso} ranging from –680 to –641 ppm (**T1**$^{\mathrm{H\text{-}I\text{-}3h}}$ and **T7**$^{\mathrm{H\text{-}I\text{-}3h}}$, respectively) and Ω is between 167 and 403 ppm (**T5**$^{\mathrm{H\text{-}I\text{-}3h}}$ and **T2**$^{\mathrm{H\text{-}I\text{-}3h}}$, respectively). For hydrolyzed-open sites of Type II (Figure 6e) δ_{iso} ranges from –690 to –619 ppm (**T1**$^{\mathrm{H\text{-}II\text{-}a\text{-}3h}}$ and **T1**$^{\mathrm{H\text{-}II\text{-}b\text{-}2h}}$, respectively) and Ω ranges from 249 to 426 ppm (**T1**$^{\mathrm{H\text{-}II\text{-}a\text{-}3h}}$ and **T2**$^{\mathrm{H\text{-}II\text{-}b\text{-}3h}}$, respectively.). Hydrolyzing the Sn-O bond with a surrounding water molecule (Scheme 1c) is, in general, energetically preferred over opening the same bond with a coordinated water molecules (Scheme 1d). Therefore, formation of the hydrolyzed sites of Type I should be more favorable than the formation of Type II hydrolyzed species.

The computational modeling on the different Sn(IV)-sites in both closed and open forms shows that they can be associated with specific NMR signatures. However, it is important to compute the variability of the ^{119}Sn NMR parameters (specifically δ_{iso} and Ω) with different conformations of water ligands coordinated to the Sn sites. Therefore, we investigated two geometrical descriptors: the Sn---OH$_2$ distance and the rotation around the Sn---OH$_2$ axis in the **T9**^{C2h} model (See Text S1 and Figure S30). For the Sn---OH$_2$ bond distance lengthening/shortening we observed that δ_{iso} varies by 17 ppm at most, while the variation in Ω can be up to 63 ppm. For Sn---OH$_2$ bond rotation, the largest variation in δ_{iso} is 13 ppm, while for Ω it is 42 ppm (details of these calculations can be found in Figure S30). These results indicate that the calculated NMR parameters are sensitive to subtle changes in the local geometry of the Sn(IV)-sites, with Ω being the most sensitive parameter. The practical consequence will be a broadening of the NMR signal and some uncertainty in the assignment of δ_{iso} and Ω to specific sites. It must also be mentioned that in some cases, the sideband manifolds extracted from the 2D MAT ^{119}Sn NMR spectra may be fit with two CS tensor parameters per isotropic shift, rather than with a single set of CS tensor parameters. These two site fits generally result in a more populated site with lower span (ca. 90-140 ppm) and another one with higher span (ca. 190-230 ppm) (see Figure S9-S13). However the population of the sites with a span larger than 190 ppm represent a minority of the Sn(IV) centers present in all Sn-β catalysts (see two-site fits in Figures S9-S13). Rather than specifically pointing towards two types of sites, the better two-site fits show that we have likely a distribution of sites and associated CS tensor parameters for a given isotropic Sn chemical shift.

Taking into account the variability in δ_{iso} and Ω, as well as the possibility of having multiple Sn(IV)-sites contributing to the same isotropic chemical shift, Figures 6b-d illustrates that several sites display ^{119}Sn NMR signatures that are close to the experimental data of the different zeolites in terms of δ_{iso} and Ω. Triply-hydrated closed (Figure 6b, olive green) and triply-hydrated defect-open (Figure 6c, orange) sites are expected to be potential active Sn(IV) sites for the different Sn-β materials. However, the hydrolyzed-open sites, of Type I and Type II also represent some possible candidates. However, the Type II hydrolyzed-open sites (Figure 6e) are very unlikely in view of their very high, calculated span ($\Omega \geq 250$ ppm), compared to the experimental data.

DISCUSSION

From the calculated chemical shifts and the relative energies, one can infer general trends and discriminate between the different T-sites explored. As mentioned above, the triply-hydrated species are predicted to be the most stable among the sites with different hydration degrees, while the hydrolyzed-open sites are most likely to be formed after hydrolysis of the Sn-O bonds. In order to narrow down the assignment of NMR signatures to more specific sites, it is possible to correlate the chemical shift of dehydrated and the most stable hydrated species, i.e. triply hydrated, as illustrated in Figure 7. Three Sn-β materials for which ^{119}Sn NMR of dehydrated and hydrated samples have been acquired are shown: the post-synthetic material Sn/deAl-Beta-OH-25 (red box in Figure 7a), and both hydrothermally synthesized materials Sn-Beta-seed (violet box in Figure 7b) and Sn-Beta (magenta box in Figure 7c). Since the hydrated and dehydrated samples always show more than one NMR signature, it is *a priori* not possible to know which signals of the hydrated sample are associated with those of the dehydrated one; it is therefore more appropriate to show the possible correlation between hydrated and dehydrated sites with box-shape diagrams (Figure 7). The relevant T-sites will then be those where both experimental and calculated sites are found close *to the corners/intersections* of the boxes.

Starting with the Sn/deAl-Beta-OH-25 zeolite (Figure 7a), three different signals of the dehydrated sample were observed at –463, –429 and –405 ppm (Table 3). The signal at –463 ppm can give rise to the corresponding three signals at –722, –696 and –670 ppm in the hydrated zeolite. According to the calculations carried out in this work, the closed T6 ($\mathbf{T6}^{\mathrm{C3h}}$) site and the T5 site as closed ($\mathbf{T5}^{\mathrm{C3h}}$) or Type I hydrolyzed-open site ($\mathbf{T5}^{\mathrm{H\text{-}I\text{-}3h}}$) (Figure 8) show signatures closest to the signals at –696, –722 ppm respectively. When comparing the calculated with the experimental span in hydrated samples (Figures 6b and 6d), T5 hydrolyzed-open Type I sites ($\mathbf{T5}^{\mathrm{H\text{-}I\text{-}3h}}$) with a chemical shift of –670 ppm is the best match. Note that in view of the calculated reaction free energies (Table 4) the T5 position is the most likely one to get hydrolyzed by a water molecule from the second coordination sphere (Type I). The resonance at –429 ppm can be associated with T3 and T8 closed sites ($\mathbf{T3}^{\mathrm{C3h}}$ and $\mathbf{T8}^{\mathrm{C3h}}$) and the corresponding hydrolyzed-open sites ($\mathbf{T3}^{\mathrm{H\text{-}I\text{-}3h}}$ and $\mathbf{T8}^{\mathrm{H\text{-}I\text{-}3h}}$) as well as $\mathbf{T4}^{\mathrm{H\text{-}I\text{-}3h}}$ based on the chemical shifts observed for the dehydrated and hydrated samples**.** Also taking the span Ω (see Figures 6a-d) into account, $\mathbf{T8}^{\mathrm{C3h}}$ with a hydrated chemical shift of –722 ppm represents the best fit for the active site related with a chemical shift at –429 ppm in dehydrated state. For all other possible sites the span is more than 70 ppm off. Note that this peak has the highest relative integrated intensity in both, the hydrated and the dehydrated spectrum. The last resonance in the dehydrated sample at –405 ppm, which only has a minor contribution with a relative integral intensity of 11 % can be best associated with defect-open sites in T1, T3, T7, T8 or T9 position based on Figure 7a. Including the span calculations the T9 open-defect site ($\mathbf{T9}^{\mathrm{O3h}}$, Figure 5b) is most likely. However, an open-defect site in T1 position is also possible (**T1**$^{\mathrm{O3h}}$). This shows that in Sn/deAl-Beta-OH-25 zeolite closed and open sites, both hydrolyzed-open as well as defect-open, most probably in T8, T5, and T9 location are feasible. The presence of open, in particular defect, sites is consistent with the hydrophilicity of this zeolite and the detection of Q_3 peaks in the ^{29}Si NMR spectra.

For the dehydrated Sn-Beta-seed (Figure 7b), three resonances at –460, –451 and –432 ppm are present (Table 3). The corresponding chemical shifts for the hydrated Sn-Beta-seed sample were observed at –734, –723, –712 and –693 ppm. Given the number of resonances, assigning specific sites to distinct data points for Sn-Beta-seed is very difficult. For the –460 ppm peak a closed T6 site (**T6**$^{\mathrm{C3h}}$) with a chemical shift of –712 ppm in hydrated zeolites is the best fit (see Figure 7b). The site with a chemical shift at –451 ppm site both **T5**$^{\mathrm{C3h}}$ and **T7**$^{\mathrm{C3h}}$ sites (Figure 8) are possible. Considering the ^{119}Sn NMR signatures for the hydrated zeolite, both **T5**$^{\mathrm{C3h}}$ and **T7**$^{\mathrm{C3h}}$ are in good agreement with theoretical predictions. The span is ~50 ppm and ~30 ppm off for **T5**$^{\mathrm{C3h}}$ and **T7**$^{\mathrm{C3h}}$, respectively. Energetically, the T7 position is predicted to be favored by 4 kcal mol^{-1} over T5. An unambiguous assignment of the chemical shift at –451 ppm to either of the two lattice positions is however not possible based on the present study. In case of the resonance at –432 ppm, which had the lowest relative integrated intensity (8 %), closed sites in Tn (n=1-4, 8-9) all represent plausible active sites in Sn-Beta-seed (**T1**$^{\mathrm{C3h}}$**,** **T2**$^{\mathrm{C3h}}$**,** **T3**$^{\mathrm{C3h}}$**,** **T4**$^{\mathrm{C3h}}$**,** **T8**$^{\mathrm{C3h}}$ and **T9**$^{\mathrm{C3h}}$) and also some hydrolyzed-open sites (**T3**$^{\mathrm{H\text{-}I\text{-}3h,}}$ **T4**$^{\mathrm{H\text{-}I\text{-}3h}}$) may be present. Associating a single resonance in the dehydrated spectra with two chemical shifts of the same T-site in the hydrated spectra (closed and hydrolyzed-open) is reasonable considering that the hydrolysis of closed sites in the presence of water should be a reversible process, which results in only closed sites upon dehydration. All of these sites are also feasible in view of the span calculations. A distinct assignment for the minor resonance with chemical shift at –432 ppm is not possible. We emphasize, however, that this zeolite is likely associated with only closed sites, consistent with its high crystallinity and the NMR data (observation of mainly Q_4 peaks in the ^{29}Si NMR spectra of the Sn-Beta-seed material, corresponding to $(SiO)_4Sn$ sites, Figure 4).

Sn-Beta (Figure 7c) showed three distinct resonances at –452, –445 and –435 ppm in its dehydrated form. The first can be associated with the T6 position, as both closed (**T6**$^{\text{C3h}}$) and hydrolyzed-open type I site (**T6**$^{\text{H-I-3h}}$). For the resonance at –445 ppm T5 and/or T7 sites in closed and hydrolyzed-open state (**T5**$^{\text{C3h}}$/**T5**$^{\text{H-I-3h}}$ and **T7**$^{\text{C3h}}$/**T7**$^{\text{H-I-3h}}$) are possible. All these assignments are feasible considering ^{119}Sn NMR calculations for both dehydrated and hydrated sites (see Figure 6a,b,d). The last resonance at –435 ppm can be best linked with T1 and/or T2 sites in closed (–732 ppm) and hydrolyzed-open type I state (–649 ppm) (**T1**$^{\text{C3h}}$/**T1**$^{\text{H-I-3h}}$ and **T2**$^{\text{C3h}}$/**T2**$^{\text{H-I-3h}}$). However hydrolyzed-open sites in T1/T2 lattice position can be excluded based on the very high span (>250) and the low stability predicted for these specific sites. As for Sn-Beta-seed closed **T3**$^{\text{C3h}}$**,** **T4**$^{\text{C3h}}$**,** **T8**$^{\text{C3h}}$ and **T9**$^{\text{C3h}}$ are all possible for the minor resonance (5% relative integral intensity) with a chemical shift at –435 ppm in the dehydrated form. Note that the resonance associated with hydrolyzed-open sites (–649 ppm in the hydrated dimension) only has a minor contribution (16 %) to the ^{119}Sn NMR spectra (Figure 4). Hence, similarly to Sn-Beta-seed, mainly closed sites can be associated with the ^{119}Sn NMR spectra, also consistent with the ^{29}Si NMR spectra where a very minor Q_3 peak and the major Q_4 peak are observed. The highly hydrophobic nature is also in agreement with the presence of mainly closed sites in the Sn-Beta material. Some of the most relevant sites in Sn-Beta and Sn-Beta-seed are shown in Figure 8 (**T5**$^{\text{C3h}}$/**T5**$^{\text{H-I-3h}}$ and **T6**$^{\text{C3h}}$/**T7**$^{\text{C3h}}$).

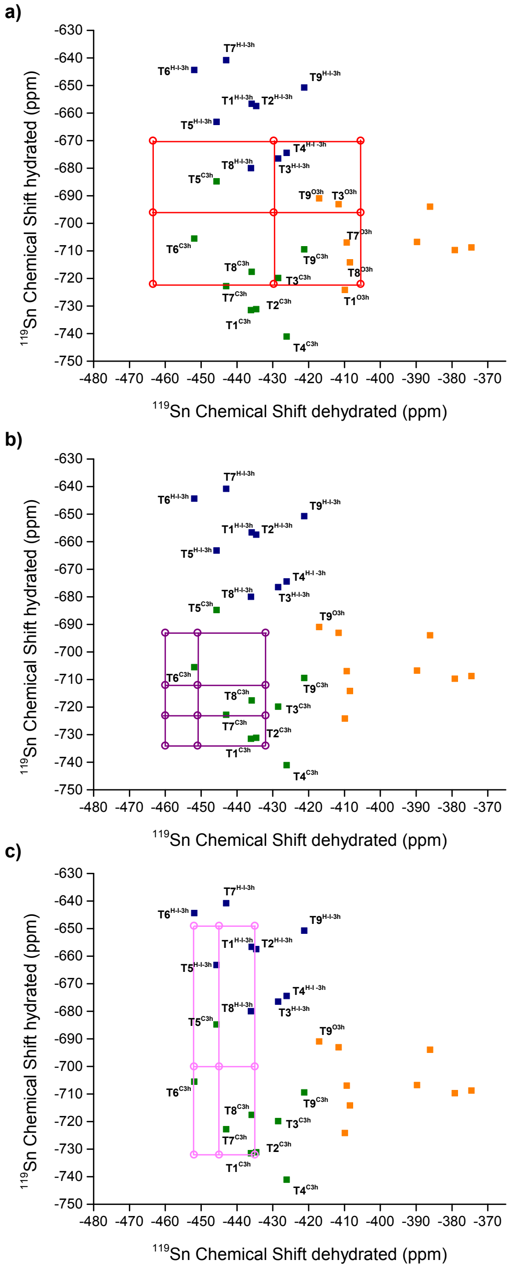

Figure 7. Comparison of measured and calculated ^{119}Sn NMR chemical shifts. Calculations for dehydrated *vs*. hydrated of closed sites (🟩), defect-open sites (🟧) and hydrolyzed-open sites of type I (🟦). Experimental chemical Sn chemical shifts for hydrated Sn/deAl-Beta-OH-25 (a, ○), Sn-Beta-seed (b, ○) and Sn-Beta (c, ○). The corner/intersections of the grids represent any possible combination of the chemical shifts in dehydrated and hydrated samples.

Comparing literature values of ^{119}Sn NMR resonances[2b,15,18b] observed for hydrothermal Sn-β samples prepared in different laboratories (Figure S31) with chemical shifts of hydrothermal Sn-β samples in the present study (Figure 7) reveals that closed sites in T5 and T7 position can be found in all of these samples. It is worth noting that the spectra reported by Davis and co-workers[15] show two resonances at –420 ppm and –445 ppm in the dehydrated sample, while the research groups of Corma[2b] and Román-Leshkov[18b] only observe a single shift at –445 ppm. The present data suggests that the –420 ppm resonance can be ascribed to a defect-open site with a silicon vacancy next to the tin in contrast to an hydrolyzed-open site (with no silicon vacancies).

Combining these insights from DNP-NMR with the other characterizations performed and the catalytic activity in the aqueous phase glucose isomerization (Table 1) shows that the materials possessing highest catalytic activity on our series consist of predominantly closed sites in T6 and T5/T7 of a hydrophobic zeolite β framework. While the importance of hydrophobicity has already been shown for Ti-β samples prepared in both, hydroxide and fluoride media,[22,40] we also show that different synthetic protocols lead to different active site distributions in the Sn-β materials. Hydrothermal synthesis leads to predominantly closed Sn(IV) centers in T6 and T5/T7 position while in post-synthetic materials a closed site in T8 position is the most populated one along with the hydrolyzed-open and defect-open forms in T5 and T9 position. However, one should point that closed sites found in the as synthesized materials are likely to undergo hydrolysis to form open-hydrolyzed sites under reaction conditions.[34,36b,41] Therefore the overall data suggest that a highly hydrophobic framework with accessible Sn sites preferably in the outer rim of the crystal is more important for good activity in the isomerization of glucose rather than the identity of the site, i.e. closed or hydrolyzed-open.

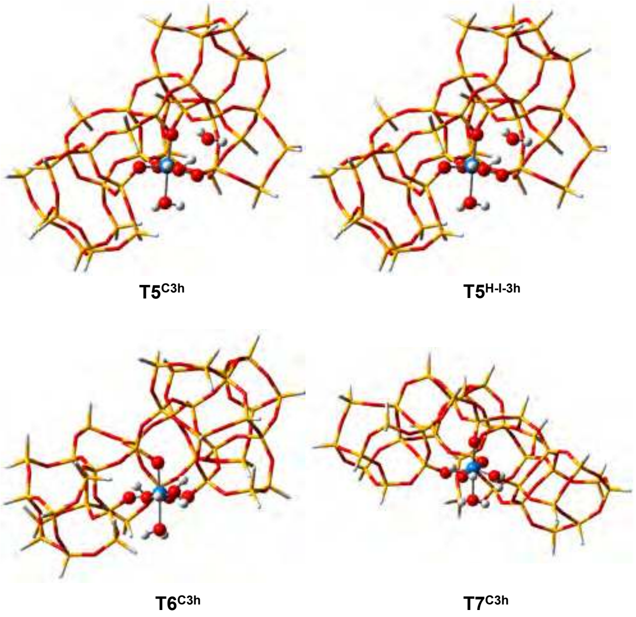

Figure 8. Optimized structures of some of the most feasible T sites as active sites in Sn-β: T5^{C3h}/T5^{H-I-3h} (upper) and T6^{C3h}/T7^{C3h} (bottom).

For both hydrothermal Sn- β zeolites, which showed the highest activity, we determined little to no defects, giving rise to a hydrophobic framework, and mostly closed Sn sites in T6, and T5/T7 positions. T1-T4 and T8/T9 closed sites cannot be fully excluded, but their corresponding resonances posses the lowest relative integral intensity, so they represent a minority of the Sn sites. In the case of the Sn-Beta, a small number of the active sites can also be linked to hydrolyzed-open sites of type I in T6, and T5/T7 positions. For the post-synthetic Sn/deAl-Beta-OH-25 with a hydrophilic framework and a significant amount of defects, Sn is most likely occupying the T8 position in closed and the T5 position in hydrolyzed-open type I form. A significant amount of defect-open sites most probably in T9 lattice position are also proposed. The chemical shifts determined for dehydrated Sn-β samples from hydrothermal synthesis indicate that in absence of water, no defect-open sites are present in the zeolite and "open" sites are only created upon hydrolysis by water, which close upon dehydration.

CONCLUSIONS

Sn-β zeolites prepared *via* different synthetic protocols show different activity in the aqueous phase isomerization of glucose. For all tested catalysts an apparent activation barrier of 20-24 kcal mol^{-1} has been observed consistent with the 1,2-hydride shift being the rate-determining step for all materials as previously found in other studies.[34] Post-synthetic materials prepared by solid-state ion-exchange show a 2.2-5 times lower activity per Sn compared to traditional hydrothermal Sn-β. ^{29}Si NMR, X-ray diffraction and water adsorption isotherms revealed that the post-synthetic materials showing lowest activity possess a hydrophilic, defective framework, which is likely causing the low activity of these materials. On the other hand hydrothermal Sn-β zeolites and post-synthetic Sn-β prepared from a defect-free Al-β with a high Si/Al ratio display a highly hydrophobic, defect-free framework and higher activity than the hydrophilic materials. The lower activity of the defect-free, post-synthetic zeolite compared to the hydrothermal samples in the glucose isomerization is likely due to a lower accessibility of the Sn-sites or a different local geometry of the active site, since almost identical activity was observed with the smaller glyceraldehyde. In addition SEM-EDX showed a more homogeneous distribution of the Sn within the zeolite crystal in case of the post-synthetic, hydrophobic material. Moreover, the use of DNP NMR allowed the expeditious determination of NMR signatures of the sites present in a series of Sn-β zeolites; combined with DFT calculations of the CSA parameters it is possible to provide the nature of these sites present in the as-synthetized samples. Predominantly closed sites, *i.e.* Sn(IV) centers four-fold bound to the zeolite framework, are present in the initial material. ^{119}Sn NMR experiments suggest that in particular T6, and T5/T7 sites represent the most abundant species in hydrothermally synthesized Sn-β materials. In dehydrated form only closed Sn sites and no defect-open sites were found in hydrothermal Sn-β zeolites. In the presence of water, closed sites coordinate water molecules and can probably partially hydrolyze (hydrolyzed-open sites) under reaction conditions, resulting in Sn(IV) three fold bound to the framework and a Sn-OH bond. On the other hand post-synthetic zeolite Sn-β prepared via a two-step method most probably consists of closed T8 and T5 hydrolyzed-open sites as well as T9 defect-open sites incorporated into the hydrophilic, defective framework. Overall, we can conclude that the activity of Sn-β in the aqueous phase isomerization of glucose is highly dependent on the morphology of the material, *i.e.* hydrophobicity. Moreover accessibility and T-site positioning of the Sn-site were found to be important. Although defect-open sites (tetrahedral SnOH) can be active, the data here shows that samples constituted mainly of closed sites are also highly active. Finally, this work provides a signature map of various Sn sites and opens the possibility to determine the active site distributions in terms of nature and lattice position of the tin centers in Sn-β zeolites, to compare the influence of synthetic protocols in the formation of specific sites, and *in fine* to rationally optimize the synthesis protocols towards the formation of the desired active sites present in this highly attractive material.

EXPERIMENTAL SECTION

Synthesis of Al-β in Fluoride media. Al-β in fluoride media was prepared by hydrothermal synthesis according to a literature procedure.[42] First Aluminum powder (99.99%, Acros) was dissolved in an aqueous solution of tetraethyl ammonium hydroxide, TEAOH (35%, SACHEM). After complete dissolution of the aluminum the solution was added to a tetraethyl orthosilicate (TEOS; 98%, Sigma-Aldrich) plus TEAOH solution. The resulting mixture is stirred until complete evaporation of ethanol, formed upon TEOS hydrolysis. To the resulting viscous gel, hydrofluoric acid (48%, Sigma-Aldrich) was added to result in a gel with the following composition: 1 SiO_2 : x Al_2O_3 : (0.54+2x) TEAOH : (0.54+2x) HF : (7+2x) H_2O. Crystallization was carried out at 140 °C in 45 mL scale teflon-lined stainless-steel autoclaves, tumbled at 60 rpm for 7 days. After cooling down, the samples were filtered and subsequently washed with deionized water and acetone before drying them in an oven at 110 °C over night. To remove the structure directing agent, samples were calcined at 580 °C under a steady air flow for 6 h.

Solid-solid ion-exchange post synthesis of Sn-β. Post-synthetic incorporation of tin was performed in two steps as described elsewhere.[43] Dealumination of the parent Al-β zeolites was done by acid leaching (13 □ HNO_3, 20 mL g^{-1}, 100 °C, 20 h). Tin was incorporated via solid-solid ion-exchange by grinding the dealuminated β with the appropriate amount of the tin(II) acetate precursor (Sigma Aldrich) followed by subsequent 3 h heat treatments under N_2 and air at 550 °C. Sn/deAl-Beta-OH represents the post-synthetic material from starting from commercial Al-β zeolite (SiO_2/Al_2O_3=25 Zeochem and SiO_2/Al_2O_3=300, Zeolyst), while the Sn/deAl-Beta-F (SiO_2/Al_2O_3=30,400) is synthesized from the Al-β synthesized in fluoride media *vide supra*.

Hydrothermal synthesis of Sn-β. Sn-β zeolites via direct incorporation of tin during hydrothermal synthesis with and without the use of β seeds were prepared following literature protocols.[27,44] TEOS was added to a TEAOH solution under stirring. After a single phase was obtained, the desired amount of tin ($SnCl_4 \cdot 5\ H_2O$, 98%, STREM) dissolved in H_2O was added drop-wise. The solution was stirred open to evaporate ethanol and water until a viscous gel was obtained. Addition of hydrofluoric acid resulted in a solid gel with the molar composition 1.0 SiO_2 : 0.01 $SnCl_4$: 0.55 TEAOH : 0.55 HF : 7.5 H_2O. In case of Sn-Beta-seed a solution of dealuminated Beta seeds in water was added. Crystallization was carried out at 140 °C in 45 mL scale teflon-lined stainless-steel autoclaves, tumbled at 60 rpm for 14 days. After cooling down, the samples were filtered and subsequently washed with deionized water and acetone before drying them in an oven at 110 °C over night. To remove the structure directing agent, samples were calcined at 580 °C under a steady air flow for 6 h.

Catalyst Characterization. Powder diffraction patterns were recorded on a Bruker D8 advance diffractometer using Cu-$K\alpha_1$ radiation and a Lynxeye detector. Relative crystallinity was calculated by integration of the d_{302}-reflection at 22.4 2θ□ using the Bruker DIFFRAC.EVA software. Al, Si and Sn contents were determined by ICP-AES on a Perkin Elmer Optima 2000 at 396.152, 251.611 and 189.927 nm respectively after acid digestion. Scanning electron microscopy (SEM) was performed using a LEO SUPRA 55 VP S3 field-emission scanning electron microscope operated at 5 kV. N_2 sorption measurements were performed on a Micromeritics 3Flex apparatus at 77K. Samples were degassed under vacuum at 350°C for 3h prior to analysis. The surface area and the pore volume were calculated using the Brunauer-Emmett-Teller (BET) and the t-plot theory respectively. The linear range of the BET plot was chosen following Rouquerol et al.[45] and is $p/p_0 = 0.005$-0.03. Argon adsorption experiments were performed at 87 K. The nonlinear density functional theory (NLDFT) model describing argon adsorption in cylindrical micro- and mesopores of metal oxides was used to calculate the pore size distribution. Water sorption experiments were performed on a Micromeritics 3Flex instrument at 298 K. Water was purified by three freeze and thaw cycles and zeolite samples were degassed under vacuum at 350 °C for 3h prior to analysis. Microporous water uptake was determined at the relative pressure p/p_0 that showed complete filling of the micropores in the N_2 adsorption.

Dynamic Nuclear Polarization NMR Spectroscopy (DNP NMR) was used to selectively enhance signals arising from the surface and to accelerate by several orders of magnitude the acquisition time of acquisition. The nitroxide biradical polarizing agents was TEKPol.[29] Incipient wetness impregnation with 1,1,2,2-tetrachloroethane (TCE) biradical solution with a concentration of approx. 16 mM biradical was used to prepare the samples for DNP NMR experiments. The impregnated samples were packed into sapphire rotors and the samples were frozen at around 105 K inside the low temperature 3.2 mm MAS probe head. Samples were typically subjected to multiple insert-eject cycles and left under an eject gas flow prior to insertion in order to reduce the amount of oxygen in the TCE solution and increase DNP enhancements.[46] Dehydrated samples were subjected to a heat treatment at 500 °C (ramp of 10 °C per min) under high vacuum (10^{-5} mbar) over night. Experiments were performed with a 400 MHz (9.4 T)/263 GHz Bruker DNP system.[47] The sweep coil of the main magnetic field was set so that microwave irradiation occurred at the ^{1}H positive enhancement maximum of nitroxide biradicals. Cross Polarization Magic Angle spinning (CPMAS)[48] with a ramped ^{1}H spin lock pulse[49] was then used to transfer polarization from the ^{1}H nuclei to the nucleus of interest (^{119}Sn or ^{29}Si). A radio frequency field of 100 kHz was always used for the ^{1}H excitation while 50 to 100 kHz RF filed was used for either ^{119}Sn or ^{29}Si excitation. In some cases, ^{119}Sn CPMAS spectra were also acquired with total suppression of spinning sidebands (TOSS)[50]. For all the samples, the ^{1}H longitudinal relaxation time (T_1) was measured using a saturation recovery type experiment. For subsequent CPMAS experiments the polarization delay was then set to $1.3 \cdot T_1$ to obtain optimal sensitivity. 2D CP-magic angle turning (CPMAT) NMR spectra correlating isotropic ^{119}Sn chemical shifts to their spinning sideband manifolds (containing isotropic and anisotropic shifts) were acquired with the 5-π pulse sequence of Grant and co-workers.[51]

Catalytic testing. All reactions were performed in 10 mL thick wall tube reactors capped with a PTFE/silicone seal, capable of holding 15 bar over-pressure. For the glucose isomerization reactions in H_2O, the reactor was charged with aqueous glucose solution (5 mL of 5 wt %) and heated to 100 °C for 15 min, prior to the addition of catalyst (50 mg). The reaction mixture was stirred vigorously at 500 rpm for the required reaction period. Samples were taken periodically and quantified by HPLC equipped with an RI detector. Monosaccharides were separated using a Ca^{2+} column (Phenomenex Rezex RCM).

Isotopic tracer studies were performed similar to a literature procedure.[23] To 1 mL of a 5 wt% aqueous glucose solution of D-glucose-d2 (Cambridge Isotope Laboratories, 2-D, 98%) in a 1.5mL GC vial equipped with a magnetic stir bar, 10 mg of Sn-β were added. The reaction mixture was stirred in a heated oil bath to 100 °C. After 2 h of reaction the reaction mixture was quenched, the catalyst separated by centrifugation and the product mixture concentrated by rotary evaporation. The concentrated product mixture was then dissolved in D_2O (99.9 atom% D, Sigma Aldrich). Solution ^1H-NMR spectra were measured on a Bruker Avance 400 MHz spectrometer averaging 8 scans at a rate of 2 scans per second.

COMPUTATIONAL DETAILS

The structures of the nine T clusters and their corresponding hydrated species were fully optimized with the Gaussian 09 code.[52] These geometries were obtained with the B3LYP-D3 density functional, which accounts for the B3LYP functional[53] with Grimme empirical dispersion corrections and Becke-Johnson damping (D3BJ)[54]. A combination of different basis sets was used in order to obtain the ground state geometries and energies: Sn was described by the LanL2DZ effective core pseudopotential (ECP)[55] augmented with a *d* polarization function, whereas the O-atoms directly bonded to Sn (including O-atoms of water in hydrated species) were described by a 6-31+G(d) basis set. The Si atoms, the rest of O atoms and the H atoms were described by the 6-31G(d,p) basis set.

Calculations of the NMR parameters[56] were carried out at the B3LYP-D3 level as implemented in the ADF code.[57] The all electron TZP basis set[58] for all atoms was used in this case. Relativistic and spin-orbit coupling were taken into account through the ZORA method[59] for the calculation of the isotropic chemical shift (δ_{iso}), the span (Ω) and skew ($\varkappa$) of all considered species. For the calculation of δ_{iso} the chemical shielding of $Sn(CH_3)_4$ was used as reference. The applied methodology has been previously tested for molecular and surface Sn species and showed excellent agreement with experiments within ca. 10 ppm.[60]

ASSOCIATED CONTENT

Supporting Information. Physico-chemical information, SEM images of various materials, glucose isomerization data, pore distribution, CP-MAT spectra, DFT optimized geometrical parameters and calculated geometrical structures of the different T sites of the Sn-β zeolites, signature map for literature examples. This material is available free of charge via the Internet at http://pubs.acs.org.

AUTHOR INFORMATION

Corresponding Author

* Aleix Comas-Vives (comas@inorg.chem.ethz.ch)

* Christophe Copéret (ccoperet@ethz.ch)

* Ive Hermans (hermans@chem.wisc.edu)

Present Addresses

Author Contributions

‡These authors contributed equally.

ACKNOWLEDGMENT

Dr. Frank Krumeich is greatfully thanked for the SEM-EDX measurement. We acknowledge SNF Grants No. 200021_143600 and 200021_146661, Ambizione project PZ00P2_148059, EQUIPEX contract ANR-10-EQPX-47-01, and ERC Advanced Grant No. 320860 for funding.

ABBREVIATIONS

pXRD, powder X-ray diffraction; ICP-OES, inductively coupled plasma-optical emission spectroscopy; BET, Brunauer, Emmett und Teller; SEM, Scanning Electron Microscopy; SSIE, solid-state ion-exchange; HT, hydrothermal; NMR, nuclear magnetic resonance spectroscopy; DNP, dynamic nuclear polarization; CSA, chemical shift anisotropy; TCE, tetrachloroethane; CPMAS, cross-polarization magic-angle spinning; CP-MAT, cross-polarization magic-angle turning; DFT, density functional theory;

REFERENCES

(1)Osmundsen, C. M.; Holm, M. S.; Dahl, S.; Taarning, E. *Proc. R. Soc. A* **2012**, *468*, 2000-2016.

(2) (a) Renz, M.; Blasco, T.; Corma, A.; Fornes, V.; Jensen, R.; Nemeth, L. *Chem. -Eur. J.* **2002**, *8*, 4708-4717; (b) Corma, A.; Nemeth, L. T.; Renz, M.; Valencia, S. *Nature* **2001**, *412*, 423-425.

(3) (a) Corma, A.; Domine, M. E.; Nemeth, L.; Valencia, S. *J. Am. Chem. Soc.* **2002**, *124*, 3194-3195; (b) Corma, A.; Domine, M. E.; Valencia, S. *J. Catal.* **2003**, *215*, 294-304; (c) Conrad, S.; Verel, R.; Hammond, C.; Wolf, P.; Goltl, F.; Hermans, I. *ChemCatChem* **2015**, *7*, 3270-3278.

(4) (a) Wolf, P.; Hammond, C.; Conrad, S.; Hermans, I. *Dalton Trans.* **2014**, *43*, 4514-4519; (b) Moliner, M.; Román-Leshkov, Y.; Davis, M. E. *Proc. Natl. Acad. Sci. U.S.A.* **2010**, *107*, 6164-6168; (c) Choudhary, V.; Pinar, A. B.; Sandler, S. I.; Vlachos, D. G.; Lobo, R. F. *ACS Catal.* **2011**, *1*, 1724-1728.

(5)Lewis, J. D.; Van de Vyver, S.; Roman-Leshkov, Y. *Angew. Chem. Int. Ed.* **2015**, *54*, 9835-9838.

(6)Van de Vyver, S.; Odermatt, C.; Romero, K.; Prasomsri, T.; Román-Leshkov, Y. *ACS Catal.* **2015**, *5*, 972-977.

(7)Pacheco, J. J.; Davis, M. E. *Proc. Natl. Acad. Sci. U.S.A.* **2014**, *111*, 8363-8367.

(8) (a) Chang, C. C.; Wang, Z. P.; Dornath, P.; Cho, H. J.; Fan, W. *RSC Adv.* **2012**, *2*, 10475-10477; (b) Kang, Z. H.; Zhang, X. F.; Liu, H. O.; Qiu, J. S.; Yeung, K. L. *Chem. Eng. J.* **2013**, *218*, 425-432.

(9) (a) Dijkmans, J.; Gabriels, D.; Dusselier, M.; de Clippel, F.; Vanelderen, P.; Houthoofd, K.; Malfliet, A.; Pontikes, Y.; Sels, B. F. *Green Chem.* **2013**, *15*, 2777-2785; (b) Tang, B.; Dai, W.

L.; Wu, G. J.; Guan, N. J.; Li, L. D.; Hunger, M. *ACS Catal.* **2014**, *4*, 2801-2810; (c) Hammond, C.; Conrad, S.; Hermans, I. *Angew. Chem. Int. Ed.* **2012**, *51*, 11736-11739.

(10)Bare, S. R.; Kelly, S. D.; Sinkler, W.; Low, J. J.; Modica, F. S.; Valencia, S.; Corma, A.; Nemeth, L. T. *J. Am. Chem. Soc.* **2005**, *127*, 12924-12932.

(11)Lamberti, C.; Bordiga, S.; Zecchina, A.; Artioli, G.; Marra, G.; Spano, G. *J. Am. Chem. Soc.* **2001**, *123*, 2204-2212.

(12)Vjunov, A.; Fulton, J. L.; Huthwelker, T.; Pin, S.; Mei, D. H.; Schenter, G. K.; Govind, N.; Camaioni, D. M.; Hu, J. Z.; Lercher, J. A. *J. Am. Chem. Soc.* **2014**, *136*, 8296-8306.

(13)Bermejo-Deval, R.; Orazov, M.; Gounder, R.; Hwang, S. J.; Davis, M. E. *ACS Catal.* **2014**, *4*, 2288-2297.

(14)Boronat, M.; Concepcion, P.; Corma, A.; Renz, M.; Valencia, S. *J. Catal.* **2005**, *234*, 111-118.

(15)Hwang, S.-J.; Gounder, R.; Bhawe, Y.; Orazov, M.; Bermejo-Deval, R.; Davis, M. *Top. Catal.* **2015**, 1-6.

(16) (a) Rai, N.; Caratzoulas, S.; Vlachos, D. G. *ACS Catal.* **2013**, *3*, 2294-2298; (b) Li, G. N.; Pidko, E. A.; Hensen, E. J. M. *Catal. Sci. Technol.* **2014**, *4*, 2241-2250.

(17) (a) Rossini, A. J.; Zagdoun, A.; Lelli, M.; Lesage, A.; Coperet, C.; Emsley, L. *Acc. Chem. Res.* **2013**, *46*, 1942-1951; (b) Lesage, A.; Lelli, M.; Gajan, D.; Caporini, M. A.; Vitzthum, V.; Mieville, P.; Alauzun, J.; Roussey, A.; Thieuleux, C.; Mehdi, A.; Bodenhausen, G.; Coperet, C.; Emsley, L. *J. Am. Chem. Soc.* **2010**, *132*, 15459-15461.

(18) (a) Wolf, P.; Valla, M.; Rossini, A. J.; Comas-Vives, A.; Nunez-Zarur, F.; Malaman, B.; Lesage, A.; Emsley, L.; Coperet, C.; Hermans, I. *Angew. Chem. Int. Ed.* **2014**, *53*, 10179-10183; (b) Gunther, W. R.; Michaelis, V. K.; Caporini, M. A.; Griffin, R. G.; Román-Leshkov, Y. *J. Am. Chem. Soc.* **2014**, *136*, 6219-6222.

(19)Bermejo-Deval, R.; Gounder, R.; Davis, M. E. *ACS Catal.* **2012**, *2*, 2705-2713.

(20)Dijkmans, J.; Dusselier, M.; Janssens, W.; Trekels, M.; Vantomme, A.; Breynaert, E.; Kirschhock, C. E. A.; Sels, B. F. *ACS Catal.* **2016**, *6*, 31-46.

(21)Roman-Leshkov, Y.; Moliner, M.; Labinger, J. A.; Davis, M. E. *Angew. Chem. Int. Ed.* **2010**, *49*, 8954-8957.

(22)Gounder, R. *Catal. Sci. Technol.* **2014**, *4*, 2877-2886.

(23)Harris, J. W.; Cordon, M. J.; Di Iorio, J. R.; Vega-Vila, J. C.; Ribeiro, F. H.; Gounder, R. *J. Catal.* **2016**, *335*, 141-154.

(24)Brunauer, S.; Deming, L. S.; Deming, W. E.; Teller, E. *J. Am. Chem. Soc.* **1940**, *62*, 1723-1732.

(25)Camblor, M. A.; Corma, A.; Valencia, S. *Chem. Commun.* **1996**, 2365-2366.

(26)Lippens, B. C.; Deboer, J. H. *J. Catal.* **1965**, *4*, 319-323.

(27)Tolborg, S.; Katerinopoulou, A.; Falcone, D. D.; Sadaba, I.; Osmundsen, C. M.; Davis, R. J.; Taarning, E.; Fristrup, P.; Holm, M. S. *J. Mater. Chem. A* **2014**, *2*, 20252-20262.

(28) (a) Rossini, A. J.; Zagdoun, A.; Lelli, M.; Canivet, J.; Aguado, S.; Ouari, O.; Tordo, P.; Rosay, M.; Maas, W. E.; Coperet, C.; Farrusseng, D.; Emsley, L.; Lesage, A. *Angew. Chem. Int. Ed.* **2012**, *51*, 123-127; (b) Zagdoun, A.; Casano, G.; Ouari, O.; Lapadula, G.; Rossini, A. J.; Lelli, M.; Baffert, M.; Gajan, D.; Veyre, L.; Maas, W. E.; Rosay, M.; Weber, R. T.; Thieuleux, C.; Coperet, C.; Lesage, A.; Tordo, P.; Emsley, L. *J. Am. Chem. Soc.* **2012**, *134*, 2284-2291; (c) Zagdoun, A.; Rossini, A. J.; Gajan, D.; Bourdolle, A.; Ouari, O.; Rosay, M.; Maas, W. E.; Tordo, P.; Lelli, M.; Emsley, L.; Lesage, A.; Coperet, C. *Chem. Commun.* **2012**, *48*, 654-656.

(29)Zagdoun, A.; Casano, G.; Ouari, O.; Schwarzwalder, M.; Rossini, A. J.; Aussenac, F.; Yulikov, M.; Jeschke, G.; Coperet, C.; Lesage, A.; Tordo, P.; Emsley, L. *J. Am. Chem. Soc.* **2013**, *135*, 12790-12797.
(30) (a) van der Wel, P. C. A.; Hu, K. N.; Lewandowski, J.; Griffin, R. G. *J. Am. Chem. Soc.* **2006**, *128*, 10840-10846; (b) Rossini, A. J.; Zagdoun, A.; Hegner, F.; Schwarzwalder, M.; Gajan, D.; Coperet, C.; Lesage, A.; Emsley, L. *J. Am. Chem. Soc.* **2012**, *134*, 16899-16908; (c) Lafon, O.; Thankamony, A. S. L.; Kobayashi, T.; Carnevale, D.; Vitzthum, V.; Slowing, I. I.; Kandel, K.; Vezin, H.; Amoureux, J. P.; Bodenhausen, G.; Pruski, M. *J. Phys. Chem. C* **2013**, *117*, 1375-1382.
(31)Pines, A.; Gibby, M. G.; Waugh, J. S. *J. Chem. Phys.* **1973**, *59*, 569-590.
(32) (a) Dixon, W. T. *J. Chem. Phys.* **1982**, *77*, 1800-1809; (b) Antzutkin, O. N.; Song, Z. Y.; Feng, X. L.; Levitt, M. H. *J. Chem. Phys.* **1994**, *100*, 130-140.
(33)Herzfeld, J.; Berger, A. E. *J. Chem. Phys.* **1980**, *73*, 6021-6030.
(34)Bermejo-Deval, R.; Assary, R. S.; Nikolla, E.; Moliner, M.; Román-Leshkov, Y.; Hwang, S. J.; Palsdottir, A.; Silverman, D.; Lobo, R. F.; Curtiss, L. A.; Davis, M. E. *Proc. Natl. Acad. Sci. U.S.A.* **2012**, *109*, 9727-9732.
(35) (a) Shetty, S.; Kulkarni, B. S.; Kanhere, D. G.; Goursot, A.; Pal, S. *J. Phys. Chem. B* **2008**, *112*, 2573-2579; (b) Shetty, S.; Pal, S.; Kanhere, D. G.; Goursot, A. *Chem. – Eur. J.* **2006**, *12*, 518-523; (c) Kulkarni, B. S.; Krishnamurty, S.; Pal, S. *J. Mol. Catal. A: Chem.* **2010**, *329*, 36-43; (d) Yang, G.; Pidko, E. A.; Hensen, E. J. M. *Chemsuschem* **2013**, *6*, 1688-1696; (e) Yang, G.; Pidko, E. A.; Hensen, E. J. M. *J. Phys. Chem. C* **2013**, *117*, 3976-3986.
(36) (a) Newsam, J. M.; Treacy, M. M. J.; Koetsier, W. T.; Degruyter, C. B. *Proc. R. Soc. A* **1988**, *420*, 375-&; (b) Montejo-Valencia, B. D.; Curet-Arana, M. C. *J. Phys. Chem. C* **2015**, *119*, 4148-4157.
(37)Corma, A.; Moliner, M.; Cantin, A.; Diaz-Cabanas, M. J.; Lorda, J. L.; Zhang, D. L.; Sun, J. L.; Jansson, K.; Hovmoller, S.; Zou, X. D. *Chem. Mater.* **2008**, *20*, 3218-3223.
(38)Christianson, J. R.; Caratzoulas, S.; Vlachos, D. G. *ACS Catal.* **2015**, *5*, 5256-5263.
(39)Roy, S.; Bakhmutsky, K.; Mahmoud, E.; Lobo, R. F.; Gorte, R. J. *ACS Catal.* **2013**, *3*, 573-580.
(40)Gounder, R.; Davis, M. E. *AIChE J.* **2013**, *59*, 3349-3358.
(41) (a) Boronat, M.; Corma, A.; Renz, M. *J. Phys. Chem. B* **2006**, *110*, 21168-21174; (b) Luo, H. Y.; Consoli, D. F.; Gunther, W. R.; Roman-Leshkov, Y. *J. Catal.* **2014**, *320*, 198-207.
(42)Camblor, M. A.; Corma, A.; Valencia, S. *J. Mater. Chem.* **1998**, *8*, 2137-2145.
(43)Parvulescu, A. N.; Müller, U.; Teles, J. H.; Vautravers, N.; Uhl, G.; Hermans, I.; Wolf, P.; Hammond, C. WO2015067654 A1, 2015.
(44)Valencia, S. V.; Corma, US6306364 B1 2001.
(45)Rouquerol, J.; Llewellyn, P.; Rouquerol, F. In *Stud. Surf. Sci. Catal.*; P.L. Llewellyn, F. R.-R. J. R., Seaton, N., Eds.; Elsevier: 2007; Vol. Volume 160, p 49-56.
(46)Kubicki, D. J.; Rossini, A. J.; Purea, A.; Zagdoun, A.; Ouari, O.; Tordo, P.; Engelke, F.; Lesage, A.; Emsley, L. *J. Am. Chem. Soc.* **2014**, *136*, 15711-15718.
(47)Rosay, M.; Tometich, L.; Pawsey, S.; Bader, R.; Schauwecker, R.; Blank, M.; Borchard, P. M.; Cauffman, S. R.; Felch, K. L.; Weber, R. T.; Temkin, R. J.; Griffin, R. G.; Maas, W. E. *Phys. Chem. Chem. Phys.* **2010**, *12*, 5850-5860.
(48)Pines, A.; Waugh, J. S.; Gibby, M. G. *J. Chem. Phys.* **1972**, *56*, 1776-&.
(49)Metz, G.; Wu, X. L.; Smith, S. O. *J. Magn. Reson., Ser. A* **1994**, *110*, 219-227.

(50)Dixon, W. T.; Schaefer, J.; Sefcik, M. D.; Stejskal, E. O.; Mckay, R. A. *J. Magn. Reson.* **1982**, *49*, 341-345.

(51)Hu, J. Z.; Alderman, D. W.; Ye, C. H.; Pugmire, R. J.; Grant, D. M. *J. Magn. Reson., Ser. A* **1993**, *105*, 82-87.

(52)Frisch, M. J.; Trucks, G. W.; Schlegel, H. B.; Scuseria, G. E.; Robb, M. A.; Cheeseman, J. R.; Scalmani, G.; Barone, V.; Mennucci, B.; Petersson, G. A.; Nakatsuji, H.; Caricato, M.; Li, X.; Hratchian, H. P.; Izmaylov, A. F.; Bloino, J.; Zheng, G.; Sonnenberg, J. L.; Hada, M.; Ehara, M.; Toyota, K.; Fukuda, R.; Hasegawa, J.; Ishida, M.; Nakajima, T.; Honda, Y.; Kitao, O.; Nakai, H.; Vreven, T.; Montgomery, J. A.; Peralta, J. E.; Ogliaro, F.; Bearpark, M.; Heyd, J. J.; Brothers, E.; Kudin, K. N.; Staroverov, V. N.; Kobayashi, R.; Normand, J.; Raghavachari, K.; Rendell, A.; Burant, J. C.; Iyengar, S. S.; Tomasi, J.; Cossi, M.; Rega, N.; Millam, J. M.; Klene, M.; Knox, J. E.; Cross, J. B.; Bakken, V.; Adamo, C.; Jaramillo, J.; Gomperts, R.; Stratmann, R. E.; Yazyev, O.; Austin, A. J.; Cammi, R.; Pomelli, C.; Ochterski, J. W.; Martin, R. L.; Morokuma, K.; Zakrzewski, V. G.; Voth, G. A.; Salvador, P.; Dannenberg, J. J.; Dapprich, S.; Daniels, A. D.; Farkas; Foresman, J. B.; Ortiz, J. V.; Cioslowski, J.; Fox, D. J. Wallingford CT, 2009.

(53) (a) Vosko, S. H.; Wilk, L.; Nusair, M. *Can. J. Phys.* **1980**, *58*, 1200-1211; (b) Lee, C. T.; Yang, W. T.; Parr, R. G. *Phys. Rev. B* **1988**, *37*, 785-789; (c) Becke, A. D. *J. Chem. Phys.* **1993**, *98*, 5648-5652; (d) Stephens, P. J.; Devlin, F. J.; Chabalowski, C. F.; Frisch, M. J. *J. Phys. Chem.* **1994**, *98*, 11623-11627.

(54) (a) Grimme, S.; Antony, J.; Ehrlich, S.; Krieg, H. *J. Chem. Phys.* **2010**, *132*; (b) Grimme, S.; Ehrlich, S.; Goerigk, L. *J. Comput. Chem.* **2011**, *32*, 1456-1465.

(55) (a) Wadt, W. R.; Hay, P. J. *J. Chem. Phys.* **1985**, *82*, 284-298; (b) Hay, P. J.; Wadt, W. R. *J. Chem. Phys.* **1985**, *82*, 299-310; (c) Hay, P. J.; Wadt, W. R. *J. Chem. Phys.* **1985**, *82*, 270-283.

(56) (a) Schreckenbach, G.; Ziegler, T. *J. Phys. Chem.* **1995**, *99*, 606-611; (b) Krykunov, M.; Ziegler, T.; Van Lenthe, E. *Int. J. Quantum. Chem.* **2009**, *109*, 1676-1683.

(57)te Velde, G.; Bickelhaupt, F. M.; Baerends, E. J.; Guerra, C. F.; Van Gisbergen, S. J. A.; Snijders, J. G.; Ziegler, T. *J. Comput. Chem.* **2001**, *22*, 931-967.

(58)Van Lenthe, E.; Baerends, E. J. *J. Comput. Chem.* **2003**, *24*, 1142-1156.

(59) (a) Wolff, S. K.; Ziegler, T. *J. Chem. Phys.* **1998**, *109*, 895-905; (b) Wolff, S. K.; Ziegler, T.; van Lenthe, E.; Baerends, E. J. *J. Chem. Phys.* **1999**, *110*, 7689-7698.

(60)Conley, M. P.; Rossini, A. J.; Comas-Vives, A.; Valla, M.; Casano, G.; Ouari, O.; Tordo, P.; Lesage, A.; Emsley, L.; Coperet, C. *Phys. Chem. Chem. Phys.* **2014**, *16*, 17822-17827.

for Table of Contents use only

Correlating Synthetic Methods, Morphology, Atomic-Level Structure and Catalytic Activity of Sn-β Catalysts

Patrick Wolf,[a,b,‡] Maxence Valla,[a,‡] Francisco Núñez-Zarur,[a,c,‡] Aleix Comas-Vives,[a,*,‡] Aaron J. Rossini,[d,‡] Connor Firth,[b] Hana Kallas,[b] Anne Lesage,[e] Lyndon Emsley,[d] Christophe Copéret,[a,*] and Ive Hermans[b,*]

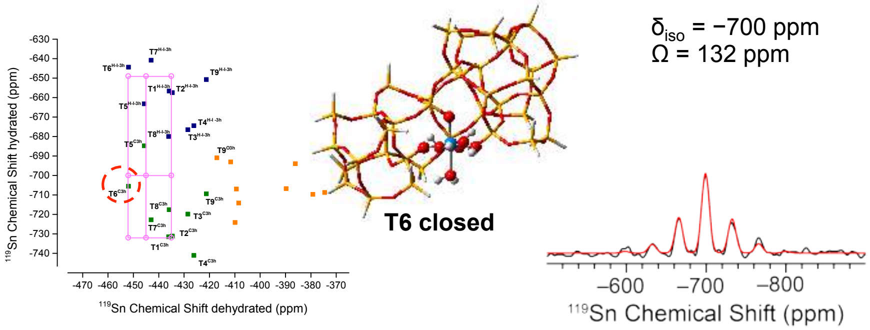

Supporting Information

Correlating Synthetic Methods, Morphology, Atomic-Level Structure and Catalytic Activity of Sn-β Catalysts

Patrick Wolf,[a,b,‡] Maxence Valla,[a, ‡] Francisco Núñez-Zarur,[a,c, ‡] Aleix Comas-Vives,[a, *,‡] Aaron J. Rossini,[d, ‡] Connor Firth,[b] Hana Kallas,[b] Anne Lesage,[e] Lyndon Emsley,[d] Christophe Copéret,[a,*] and Ive Hermans[b,*]

[a] Department of Chemistry and Applied Biosciences, ETH Zurich, Vladimir Prelog Weg 2, 8093 Zurich (Switzerland)

[b] Department of Chemistry & Department of Chemical and Biological Engineering, University of Wisconsin – Madison, 1101 University Avenue, Madison, WI 53706 (USA)

[c] Instituto de Química, Universidad de Antioquia, Calle 70 Nº. 52-21, Medellín, Colombia
[d] Institut des Sciences et Ingénierie Chimiques, Ecole Polytechnique Fédérale de Lausanne, EPFL, Batochime, 1015 Lausanne (Switzerland)

[e] Centre de RMN à Tres Hauts Champs, Institut de Sciences Analytiques, Université de Lyon (CNRS/ENS Lyon/UCB Lyon 1) 69100 Villeurbanne (France)

* To whom correspondence should be addressed: Aleix Comas-Vives (comas@inorg.chem.ethz.ch);
Christophe Copéret (ccoperet@inorg.chem.ethz.ch);
Ive Hermans (hermans@chem.wisc.edu)

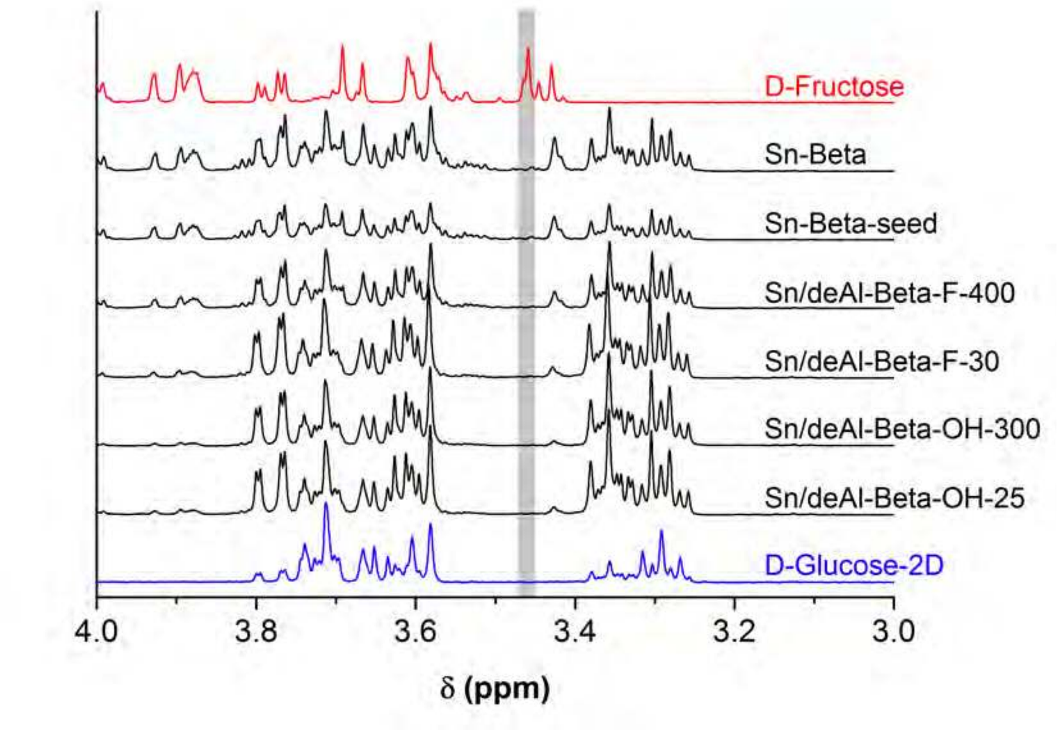

Figure S1. ^{1}H NMR spectra of reaction mixtures from D-glucose-2D isomerization after 2h at 100°C with the Sn-ß samples tested in this study. The δ=3.47 ppm is characteristic for the ^{1}H in the C1 position of the D-fructose. The absence of this resonance confirms the selective formation of D-Fructose-1D from D-glucose-2D *via* 1,2-hydride shift over the Lewis acid Sn sites.

Table S1. Physicochemical properties of different Sn-ß zeolites.

Catalyst	Crystallinity[a] [%]	BET[b] [m^2 g^{-1}]	V_{micro}[c] [mL g^{-1}]	V_{meso}[c] [mL g^{-1}]	S_{ext}[c] [m^2 g^{-1}]	Si/Sn[d]	SiO_2/Al_2O_3[e]	H_2O_{ads}[f] [mmol g^{-1}]	H_2O_{ads}[g] [mmol g^{-1}]
Sn-β From Post-Synthetic Incorporation									
Sn/deAl-Beta-OH-25	53	616	0.18	0.18	166.9	163	25	1.22	12.0
Sn/deAl-Beta-OH-300	52	637	0.20	0.17	151.0	178	300	1.28	10.1
Sn/deAl-Beta-F-30	61	651	0.20	0.14	151.1	160	32	0.54	7.9
Sn/deAl-Beta-F-400	85	554	0.20	0.05	32.5	196	398	0.33	2.3
Sn-β From Hydrothermal Synthesis									
Sn-Beta-seed	100	650	0.23	0.04	53.3	197	-	0.27	2.5
Sn-Beta	78	610	0.21	0.07	66.7	182	-	0.26	2.4

[a] Calculated from integration of the d_{302}-reflection at 22.4 2θ. [b] Brunauer-Emmet-Teller area; linear range of $p/p_0 = 0.005$-0.03 chosen following Rouquerol et al.[1] [c] Micropore, mesopore volume and external surface area derived from the t-plot. [d] Determined by ICP-AES. [e] Si/Al ratio of parent zeolite determined by ICP-AES. [f] quantity of water adsorbed in the micropores; $p/p_0 = 0.10$. [g] at $p/p_0 = 0.82$.

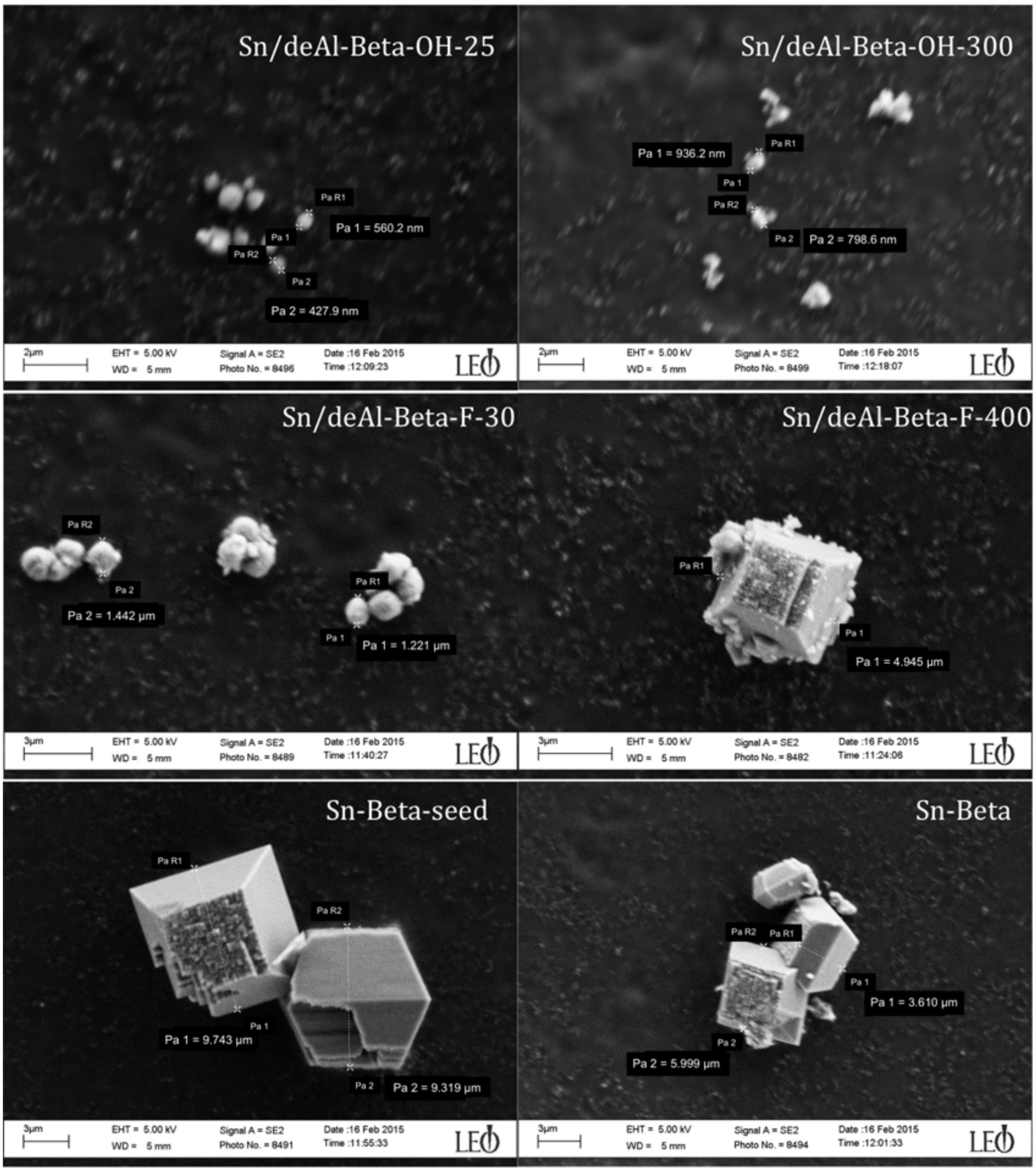

Figure S2. Scanning Electron Micrographs of the various Sn-ß samples.

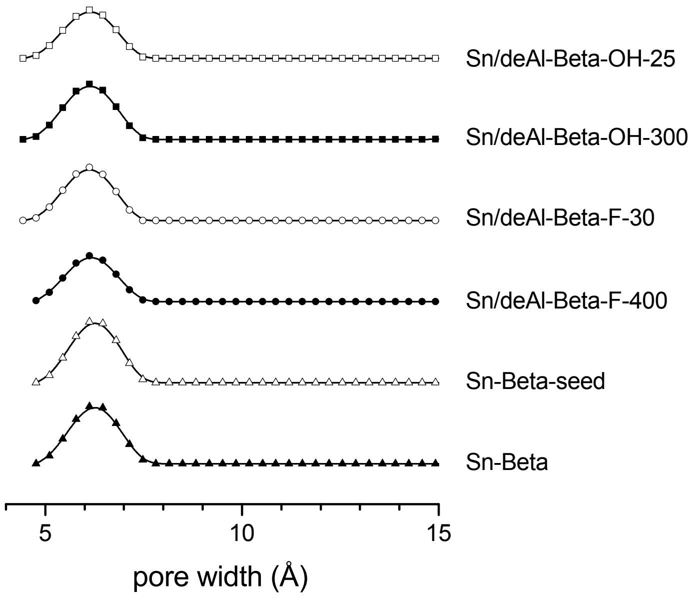

Figure S3. DFT pore size distribution derived from Ar adsorption isotherms at 87 K for various Sn-ß catalysts.

Figure S4. SEM-EDX of Sn/deAl-Beta-F400 showing the homogeneous distribution of Sn in the crystal.

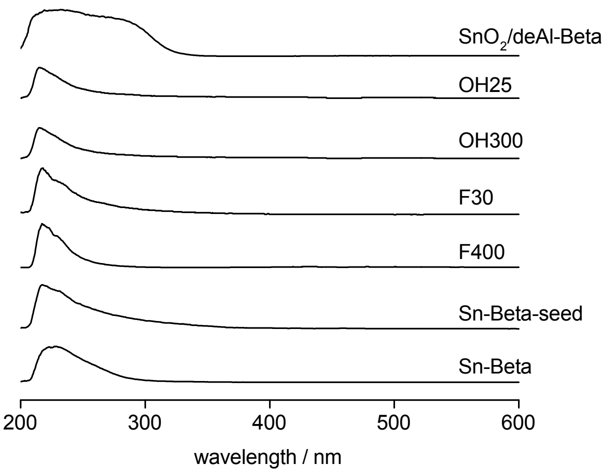

Figure S5. DR-UV/Vis spectra of SnO_2 on deAl-Beta and the different Sn-Beta zeolites showing the absence of SnO_2 in the prepared Sn-ß samples.

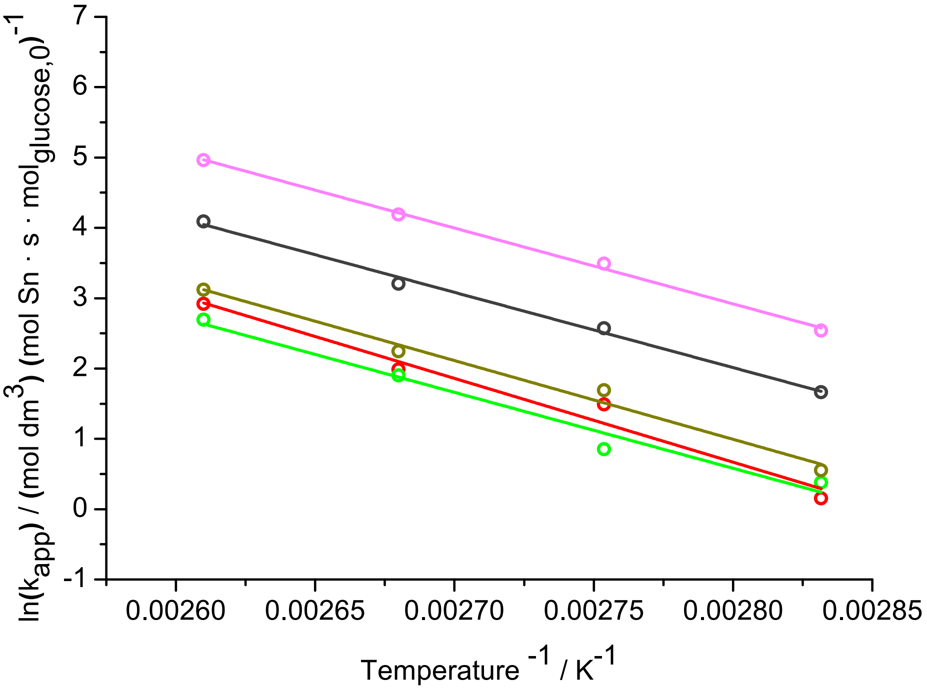

Figure S6. Arrhenius plot for the isomerization of glucose with different Sn-ß zeolites in the temperature range of 353-383K. Sn/deAl-Beta-OH-25 (○) Sn/deAl-Beta-OH-300 (○), Sn/deAl-Beta-F-30 (○), Sn-Beta-F-400 (○) and Sn-Beta (○).

Table S2 Activity and activation energies of different Sn-β zeolites in the aqueous phase isomerization reaction of glyceraldehyde.[a,f]

Entry	Catalyst[b]	Activity per Sn_{init}[c,d] [h^{-1}]	DHA Yield[e] [%]	DHA Selectivity[e] [%]	E_{app}[f] [kcal mol^{-1}]	Pre-exponential factor A[f,g]
Sn-β From Post-Synthetic Incorporation						
1	Sn/deAl-Beta-OH-25	144 ± 18	13	>99	21.3 ± 0.8	22 ± 1.0
2	Sn/deAl-Beta-F-400	868 ± 107	43	95	18.5 ± 0.5	19.5 ± 0.6

[a] Reaction conditions: 27 mg of catalyst in 5 mL of a 0.3 M aqueous glyceraldehyde solution at 70 °C. [b] Sn/deAl-Beta: tin incorporated into dealuminated β by solid-solid ion-exchange; OH: parent Al-Beta zeolite synthesized in hydroxide media; F: parent Al-Beta zeolite synthesized in fluoride media; 25: SiO_2/Al_2O_3 ratio of parent zeolite; Sn-Beta: hydrothermally synthesized Sn-β zeolite; seed: β seed crystals added to the synthesis gel. [c] Defined as the mole product generated per mole Sn per hour calculated at the initial stage of the reaction. [d] Error based on ICP-OES determined Sn-loading. [e] After 20 min of reaction. [f] rates are measured in mole product formed per second normalized per total mole metal in the catalyst; temperatures for Arrhenius plot range from 50-80°C. [g] units: (mol · dm^3)(mol Sn · s · mol glyceraldehyde)$^{-1}$

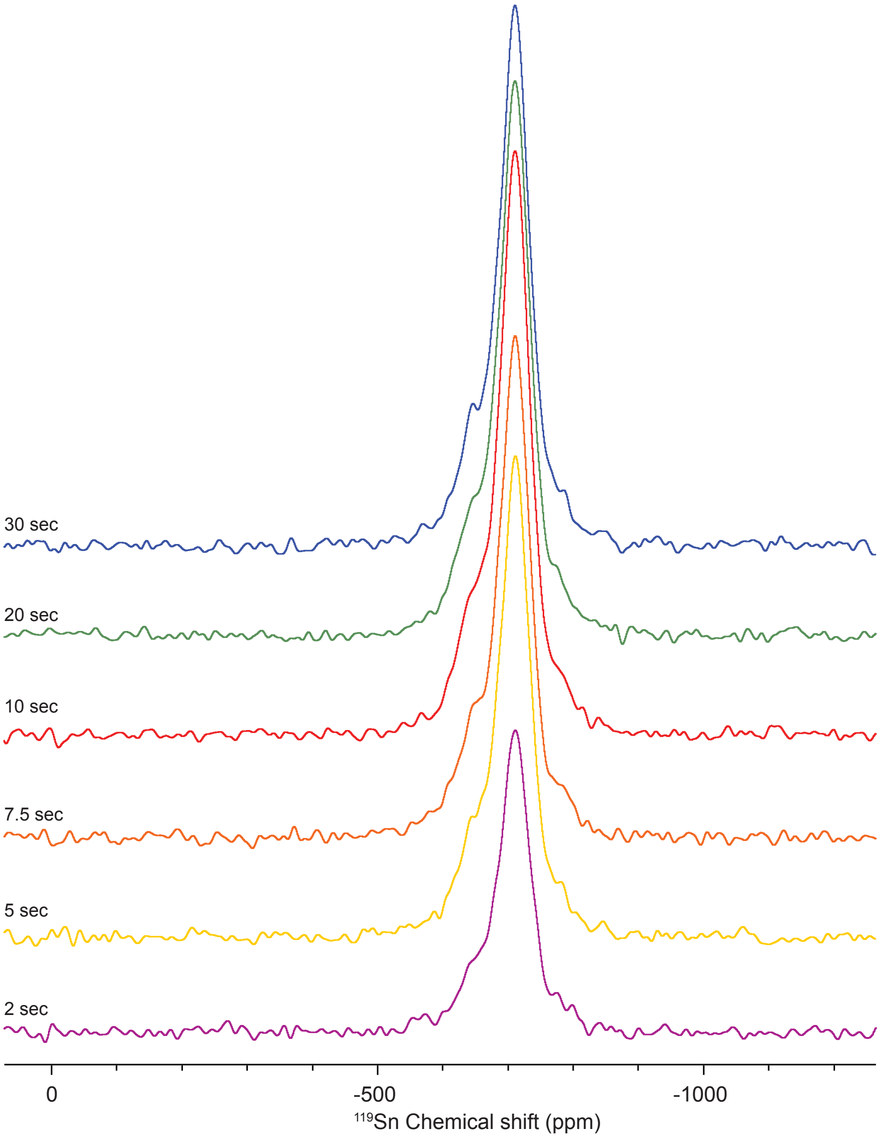

Figure S7. DNP enhanced ^{1}H-^{119}Sn CP-echo spectrum of Sn/deAl-Beta-OH-25 with polarization delays between 2.0 to 30 s. The spectra were acquired with a CP contact time of 3.5 ms, a t_1 increment of 12.50 μs, 280 scans per t_1 increment and 132 t_1 increments were acquired. A MAS frequency of 4000 Hz was used.

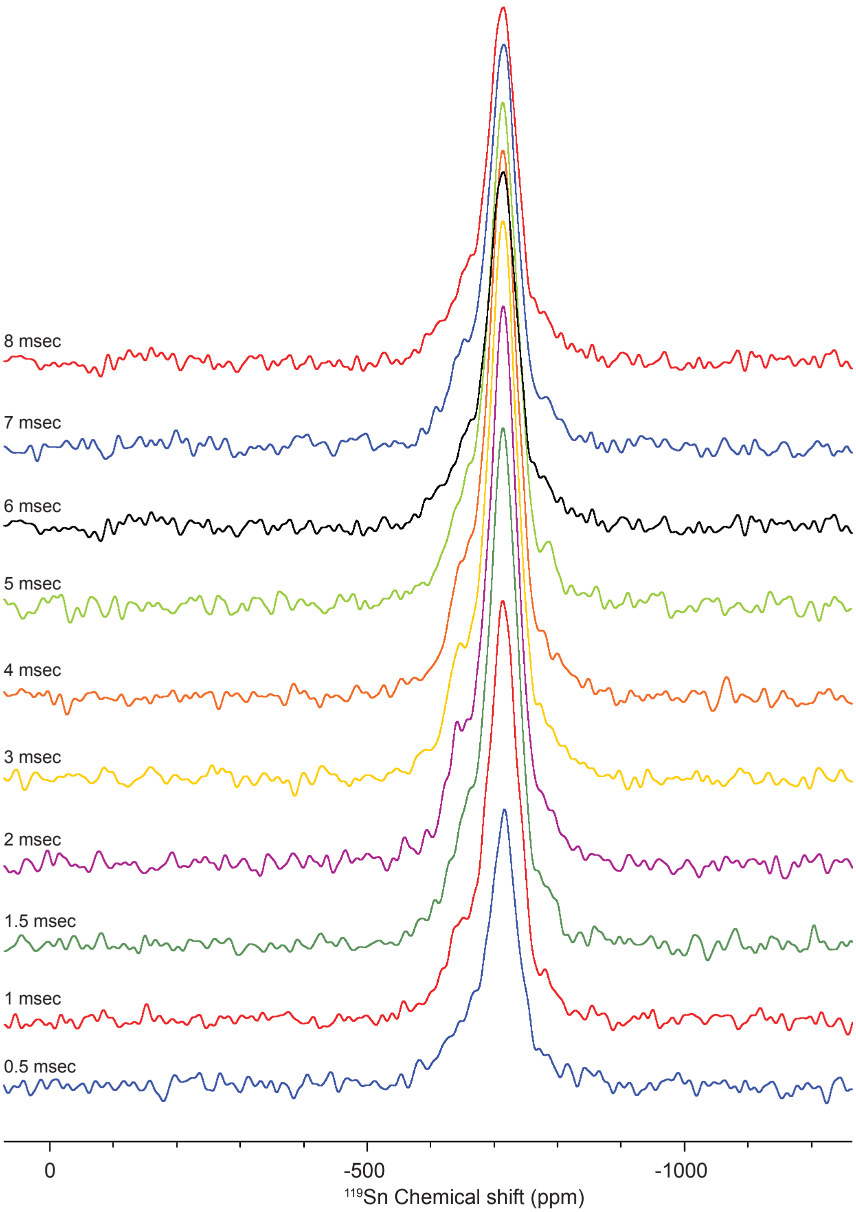

Figure S8. DNP enhanced DNP enhanced ^{1}H-^{119}Sn CP-echo spectrum of Sn/deAl-Beta-OH-25 with different CP contact times. The spectra were acquired with a polarization delay of 3.5 s, a t_1 increment of 12.50 μs, 280 scans per t_1 increment and 132 t_1 increments were acquired. A MAS frequency of 4000 Hz was used.

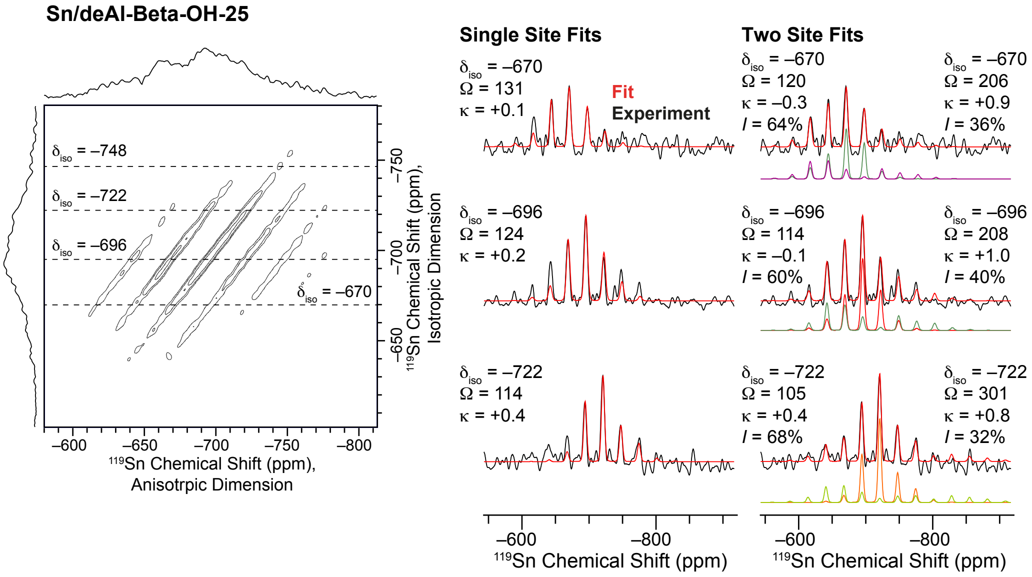

Figure S9. DNP enhanced ^{1}H-^{119}Sn CP-MAT spectrum of Sn/deAl-Beta-OH-25. The spectrum was acquired with a CP contact time of 3.5 ms, a polarization delay of 2.2 s, a t_1 increment of 12.50 μs, 280 scans per t_1 increment and 132 t_1 increments were acquired. A MAS frequency of 4000 Hz was used. Fits to the sideband manifolds are shown for the three most intense isotropic peaks (dashed lines) and the CS tensor parameters obtained from the fits for both a single-site and a two-site fit are indicated. The site at –748 ppm with a relative integral intensity of only 6% cannot be properly fitted.

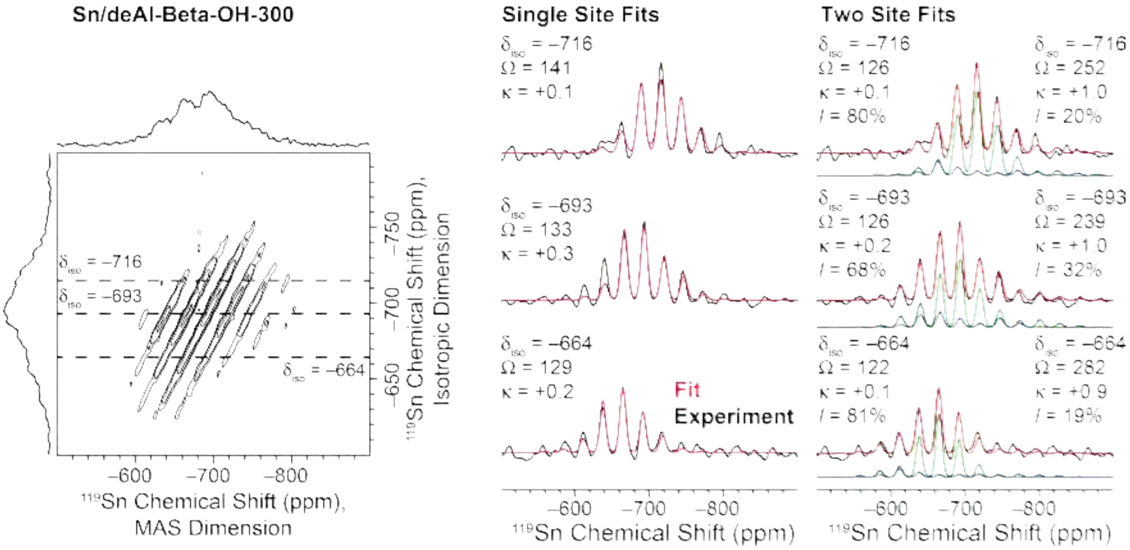

Figure S10. DNP enhanced ^{1}H-^{119}Sn CP-MAT spectrum of Sn/deAl-Beta-OH-300. The spectrum was acquired with a CP contact time of 3 ms, a polarization delay of 3.2 s, a 25 μs t_1 increment, 112 scans per t_1 increment and 56 t_1 increments were acquired. A MAS frequency of 4000 Hz was used. A MAS frequency of 4000 Hz was used. Fits to the sideband manifolds are shown for the three isotropic peaks (dashed lines) and the CS tensor parameters obtained from the fits for both a single-site and a two-site fit are indicated.

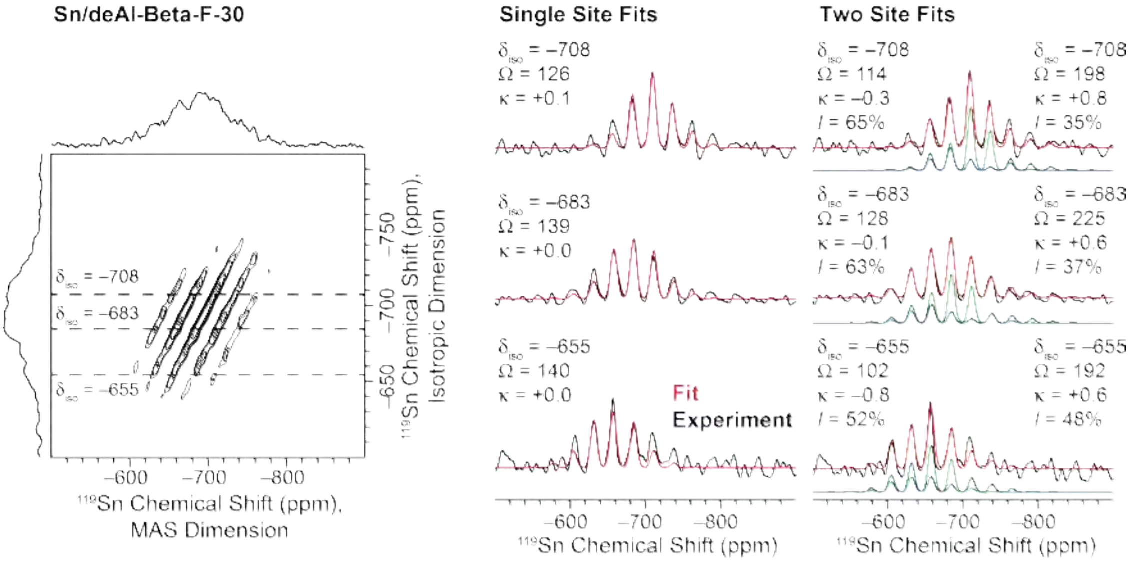

Figure S11. DNP enhanced ^{1}H-^{119}Sn CP-MAT spectrum of Sn/deAl-Beta-F-30. The spectrum was acquired with a CP contact time of 3 ms, a polarization delay of 3.2 s, a 25 μs t_1 increment, 56 scans per t_1 increment and 90 t_1 increments were acquired. A MAS frequency of 4000 Hz was used. Fits to the sideband manifolds are shown for the two isotropic peaks (dashed lines) and the CS tensor parameters obtained from the fits for both a single-site and a two-site fit are indicated.

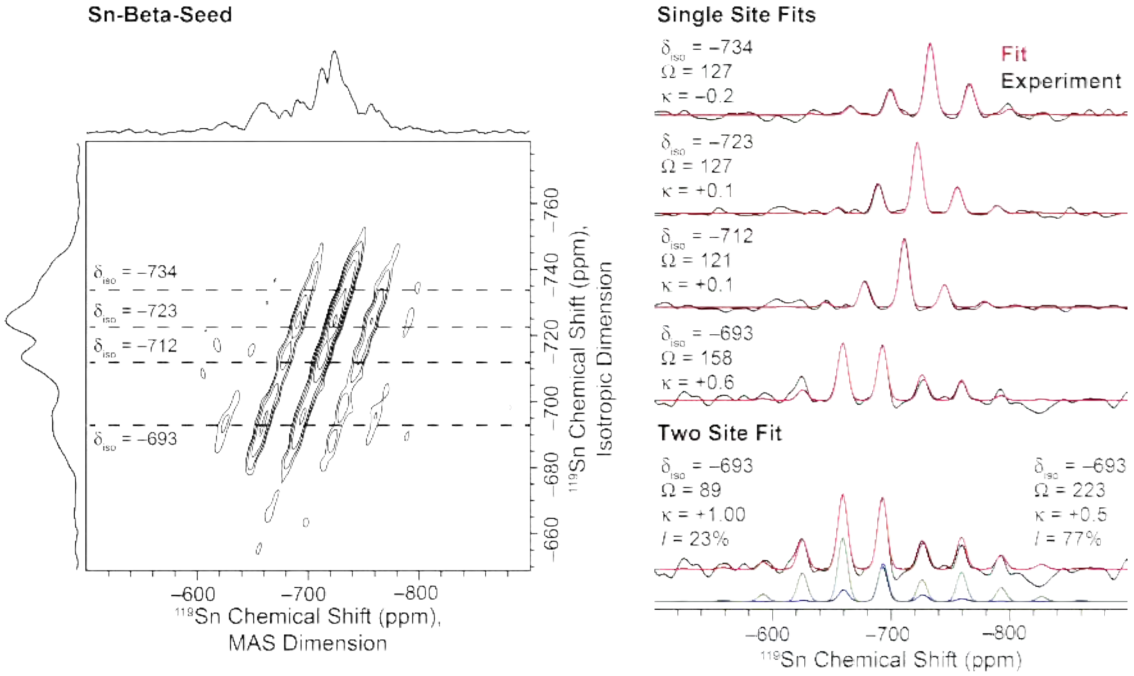

Figure S12. DNP enhanced ^{1}H-^{119}Sn CP-MAT spectrum of Sn-Beta-seed. The spectrum was acquired with a CP contact time of 3 ms, a polarization delay of 7 s, a 34.7 μs t_1 increment, 56 scans per t_1 increment and 132 t_1 increments were acquired. A MAS frequency of 5000 Hz was used. Fits to the sideband manifolds are shown for the two isotropic peaks (dashed lines) and the CS tensor parameters obtained from the fits for a single-site. For the peak at δ_{iso} = –693 ppm a two-site fit is also shown.

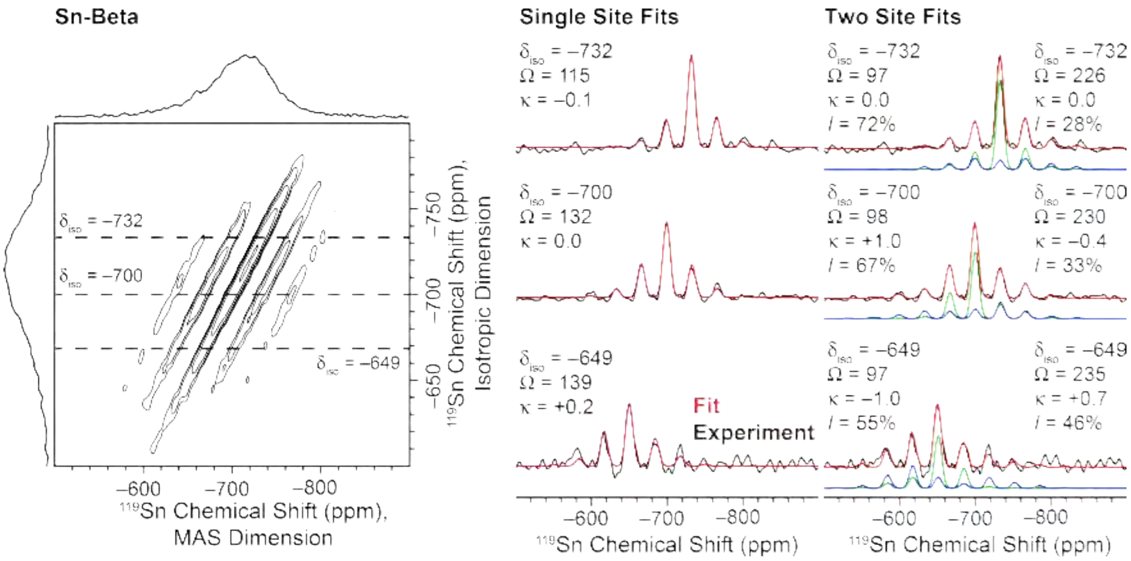

Figure S13. DNP enhanced ^{1}H-^{119}Sn CP-MAT spectrum of Sn-Beta. The spectrum was acquired with a CP contact time of 3 ms, a polarization delay of 5 s, a 12.5 μs t_1 increment, 140 scans per t_1 increment and 80 t_1 increments were acquired. A MAS frequency of 5000 Hz was used. Fits to the sideband manifolds are shown for the two isotropic peaks (dashed lines) and the CS tensor parameters obtained from the fits for both a single-site and a two-site fit are indicated.

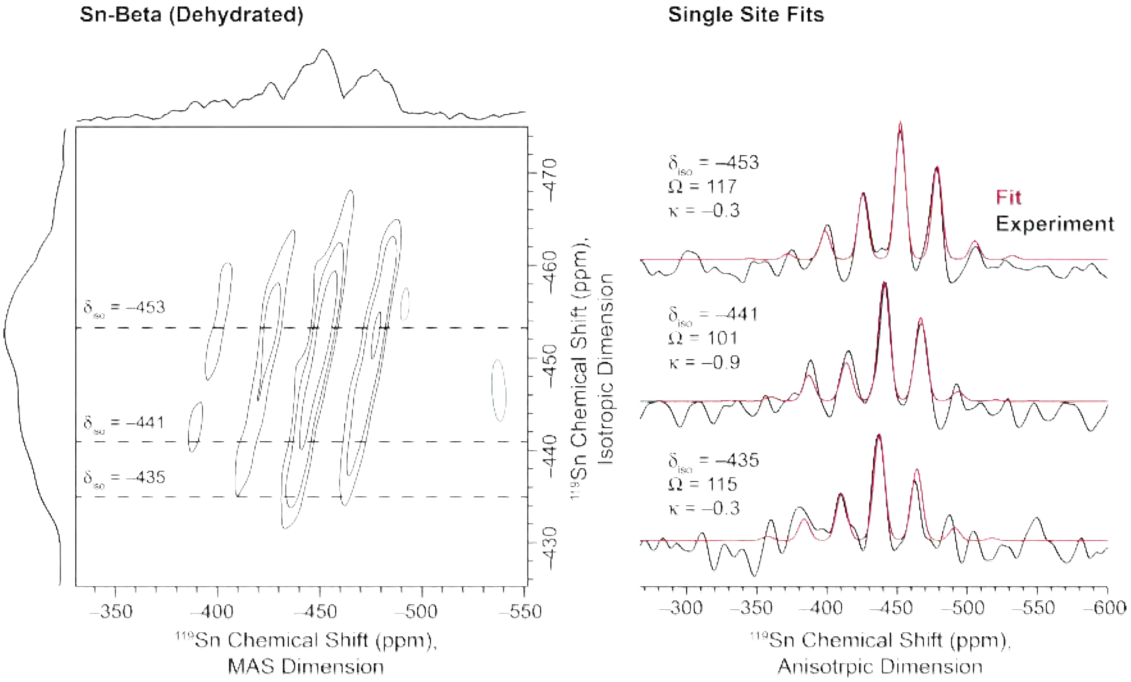

Figure S14. DNP enhanced ^{1}H-^{119}Sn CP-MAT spectrum of Sn-Beta dehydrated The spectrum was acquired with a CP contact time of 5.5 ms, a polarization delay of 15 s, a 77.4 μs t_1 increment, 392 scans per t_1 increment and 28 t_1 increments were acquired. A MAS frequency of 4500 Hz was used. Fits to the sideband manifolds are shown for the two isotropic peaks (dashed lines) and the CS tensor parameters obtained from the fits for a single-site.

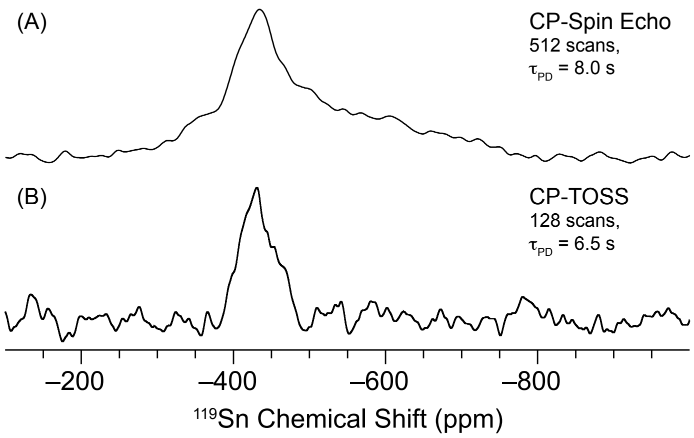

Figure S15. Comparison of DNP enhanced ^{1}H-^{119}Sn CP-echo (A) and CP-TOSS (B) spectrum of dehydrated Sn/deAl-Beta-OH-25.

Table S3. Calculated main average geometrical parameters of all dehydrated T sites in Sn-β. Average distances are given in Å and average angles in degrees.

	Closed sites				**Defect-open sites**				
Site	**Sn-O**	**Sn-Si**	**O-Sn-O**	**Sn-O-Si**	**Sn-OH**	**Sn-O**	**Sn-Si**	**O-Sn-O**	**Sn-O-Si**
T1	1.894	3.235	109.5	132.8	1.886	1.904	3.299	109.3	138.5
T2	1.895	3.234	109.5	132.9	1.889	1.905	3.210	109.5	129.5
T3	1.894	3.242	109.4	133.6	1.904	1.892	3.251	109.5	133.8
T4	1.894	3.232	109.4	133.1	1.906	1.895	3.209	109.5	129.5
T5	1.888	3.273	109.5	129.5	1.923	1.888	3.216	109.5	132.8
T6	1.886	3.291	109.4	140.8	1.903	1.895	3.270	109.5	136.2
T7	1.890	3.248	109.5	135.9	1.921	1.890	3.241	109.5	136.0
T8	1.893	3.226	109.5	133.3	1.904	1.898	3.225	109.4	133.3
T9	1.894	3.213	109.4	131.9	1.918	1.893	3.229	109.4	133.7

Table S4. Main average geometrical parameters of all mono-hydrated closed sites formed in Sn-β. O atoms with “w” superscript correspond to O atoms of the water ligands. Distances are given in Å and angles in degrees.

Site	Sn-O	Sn-Ow	Sn-Si	O-Sn-O	O-Sn-Ow	Sn-O-Si
$T1^{C1}$	1.913	2.278	3.251	118.0	178.1	133.5
$T2^{C1}$	1.910	2.300	3.282	117.8	173.3	136.5
$T3^{C1}$	1.907	2.334	3.286	117.0	173.0	138.0
$T4^{C1}$	1.911	2.315	3.284	116.8	175.8	137.4
$T5^{C1}$	1.908	2.289	3.330	116.9	170.2	143.8
$T6^{C1}$	1.904	2.275	3.331	117.5	175.8	142.1
$T7^{C1}$	1.911	2.303	3.259	116.9	174.5	135.2
$T8^{C1}$	1.914	2.330	3.254	116.2	172.8	135.2
$T9^{C1}$	1.912	2.331	3.258	116.4	174.8	135.3

Table S5. Main average geometrical parameters of all doubly-hydrated closed sites formed in Sn-β. O atoms with "w" superscript correspond to O atoms of the water ligands. Distances are given in Å and angles in degrees.

	Sn-O	**$Sn-O^{w1}$**	**$Sn-O^{w2}$**	**Sn-Si**	**O-Sn-O**	**$O-Sn-O^{w}$**	**Sn-O-Si**
$T1^{C2}$	1.939	2.251	2.174	3.290	96.3	171.3	129.7
$T2^{C2}$	1.933	2.255	2.223	3.303	96.9	166.3	142.5
$T3^{C2}$	1.931	2.253	2.292	3.297	98.0	170.5	140.1
$T4^{C2}$	1.934	2.260	2.274	3.337	99.8	171.5	140.7
$T5^{C2}$	1.940	2.266	2.296	3.247	99.7	174.8	131.4
$T6^{C2}$	1.945	2.242	2.266	3.264	97.9	172.2	133.0
$T7^{C2}$	1.944	2.258	2.218	3.289	99.5	175.5	135.3
$T8^{C2}$	1.950	2.219	2.219	3.263	98.6	174.3	132.8
$T9^{C2}$	1.945	2.202	2.270	3.275	99.3	168.6	134.1

Table S6. Main average geometrical parameters of all triply-hydrated closed sites formed in Sn-β. O atoms with “w” superscript correspond to O atoms of the water ligands. Distances are given in Å and angles in degrees.

	Sn-O	**Sn-O^{w1}**	**Sn-O^{w2}**	**Sn-Si**	**O-Sn-O**	**O-Sn-O^{w}**	**Sn-O-Si**
T1^{C3}	1.945	2.271	2.127	3.304	95.4	169.5	138.3
T2^{C3}	1.943	2.174	2.180	3.302	95.3	170.7	141.0
T3^{C3}	1.939	2.168	2.289	3.302	97.0	173.2	139.4
T4^{C3}	1.947	2.164	2.260	3.359	98.2	170.1	141.7
T5^{C3}	1.948	2.191	2.284	3.285	98.7	173.5	133.9
T6^{C3}	1.955	2.221	2.197	3.270	96.9	168.9	132.7
T7^{C3}	1.953	2.180	2.236	3.290	98.4	176.5	134.6
T8^{C3}	1.960	2.159	2.219	3.268	97.5	174.7	132.4
T9^{C3}	1.957	2.134	2.279	3.274	97.9	168.8	132.9

Table S7. Main average geometrical parameters of all doubly-hydrated defect-open sites formed in Sn-β. O atoms with "w" superscript correspond to O atoms of the water ligands. Distances are given in Å and angles in degrees.

	Sn-OH	**Sn-O**	**Sn-O^{w1}**	**Sn-O^{w2}**	**Sn-Si**	**O-Sn-O**	**O-Sn-O^{w}**	**Sn-O-Si**
T1^{O2}	1.967	1.935	2.288	2.154	3.348	98.1	169.7	143.1
T2^{O2}	1.925	1.953	2.189	2.266	3.289	96.8	167.2	138.3
T3^{O2}	1.960	1.956	2.218	2.198	3.315	97.4	171.4	134.4
T4^{O2}	1.951	1.938	2.304	2.262	3.307	100.7	177.2	144.1
T5^{O2}	1.990	1.939	2.177	2.287	3.303	99.3	170.9	136.9
T6^{O2}	1.948	1.959	2.227	2.250	3.289	97.8	167.7	134.3
T7^{O2}	1.958	1.943	2.292	2.245	3.295	99.9	174.9	135.8
T8^{O2}	1.989	1.943	2.219	2.233	3.293	98.4	176.5	135.4
T9^{O2}	1.953	1.946	2.276	2.264	3.300	100.1	165.1	136.2

Table S8. Main average geometrical parameters of all triply-hydrated defect-open sites formed in Sn-β. O atoms with "w" superscript correspond to O atoms of the water ligands. Distances are given in Å and angles in degrees.

	Sn-OH	**Sn-O**	**Sn-O^{w1}**	**Sn-O^{w2}**	**Sn-Si**	**O-Sn-O**	**O-Sn-O^{w}**	**Sn-O-Si**
$T1^{O3}$	1.970	1.942	2.177	2.127	3.398	96.0	170.8	154.0
$T2^{O3}$	1.982	1.955	2.154	2.172	3.332	96.3	174.8	138.3
$T3^{O3}$	1.957	1.972	2.130	2.225	3.326	95.8	173.4	135.9
$T4^{O3}$	1.959	1.947	2.174	2.250	3.341	98.7	177.4	140.5
$T5^{O3}$	1.995	1.949	2.119	2.275	3.312	97.8	171.2	137.0
$T6^{O3}$	1.934	1.974	2.145	2.300	3.297	97.4	170.5	133.6
$T7^{O3}$	1.984	1.952	2.206	2.230	3.306	98.2	174.4	136.1
$T8^{O3}$	1.985	1.955	2.157	2.240	3.310	97.2	176.1	137.3
$T9^{O3}$	1.964	1.954	2.147	2.238	3.308	97.7	172.0	137.1

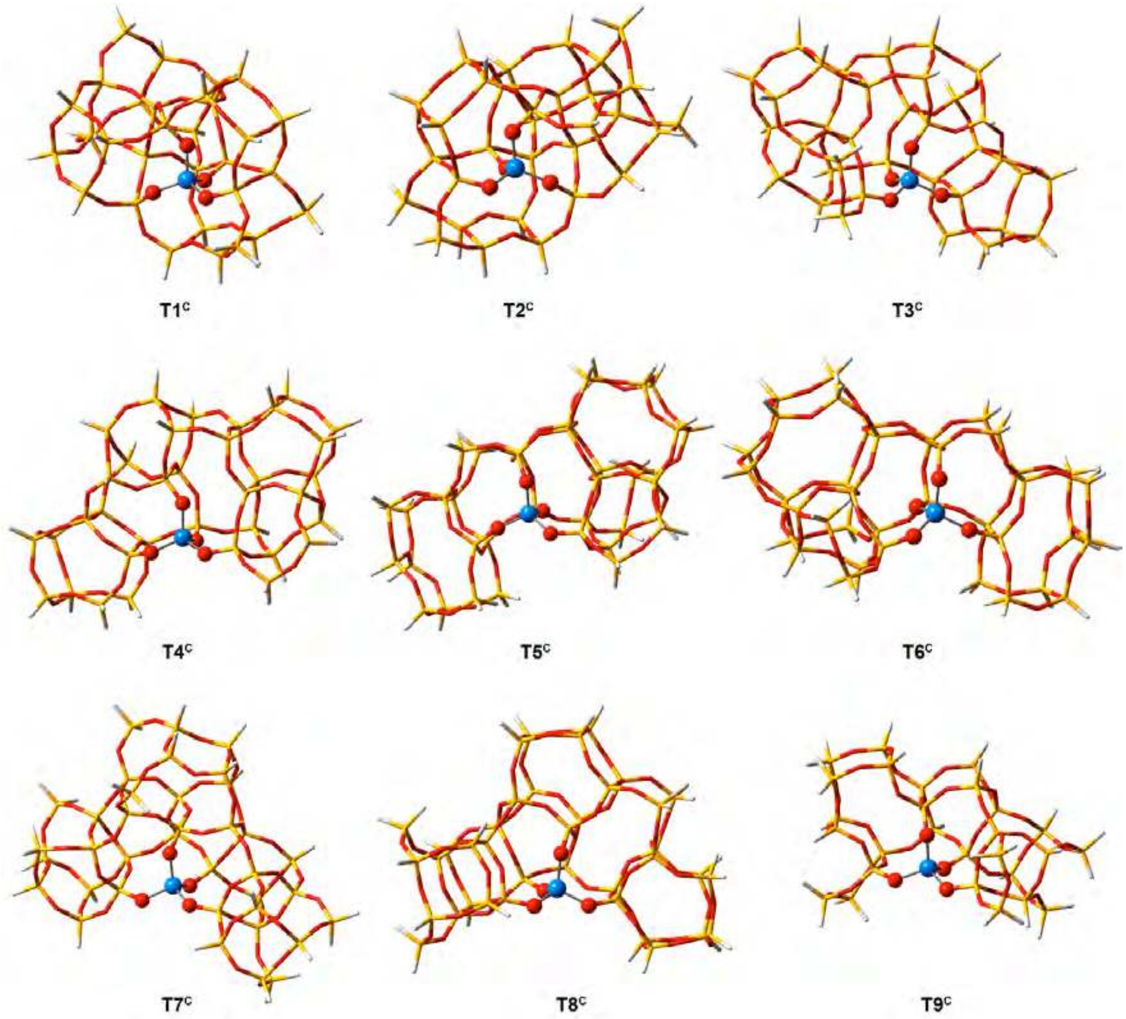

T1^c T2^c T3^c T4^c T5^c T6^c T7^c T8^c T9^c

Figure S16. Optimized structures of all dehydrated closed sites of Sn-β. The Sn atom and its first coordination sphere are highlighted with ball and sticks model. Sn atoms are shown in blue, oxygen in red, silicon in yellow and hydrogen in white.

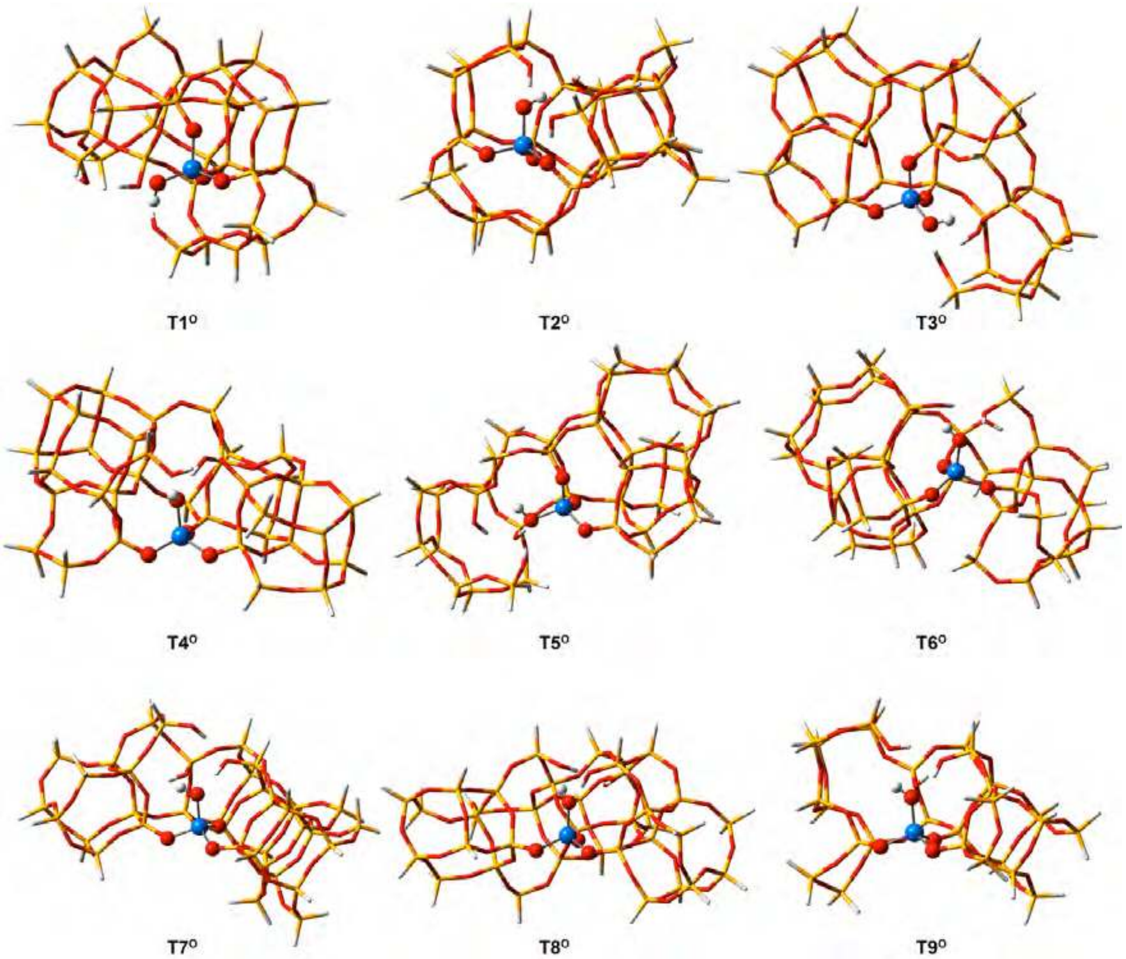

T1^{O} T2^{O} T3^{O}

T4^{O} T5^{O} T6^{O}

T7^{O} T8^{O} T9^{O}

Figure S17. Optimized structures of all dehydrated defect-open sites of Sn-β. The Sn atom and its first coordination sphere are highlighted with ball and sticks model. Sn atoms are shown in blue, oxygen in red, silicon in yellow and hydrogen in white.

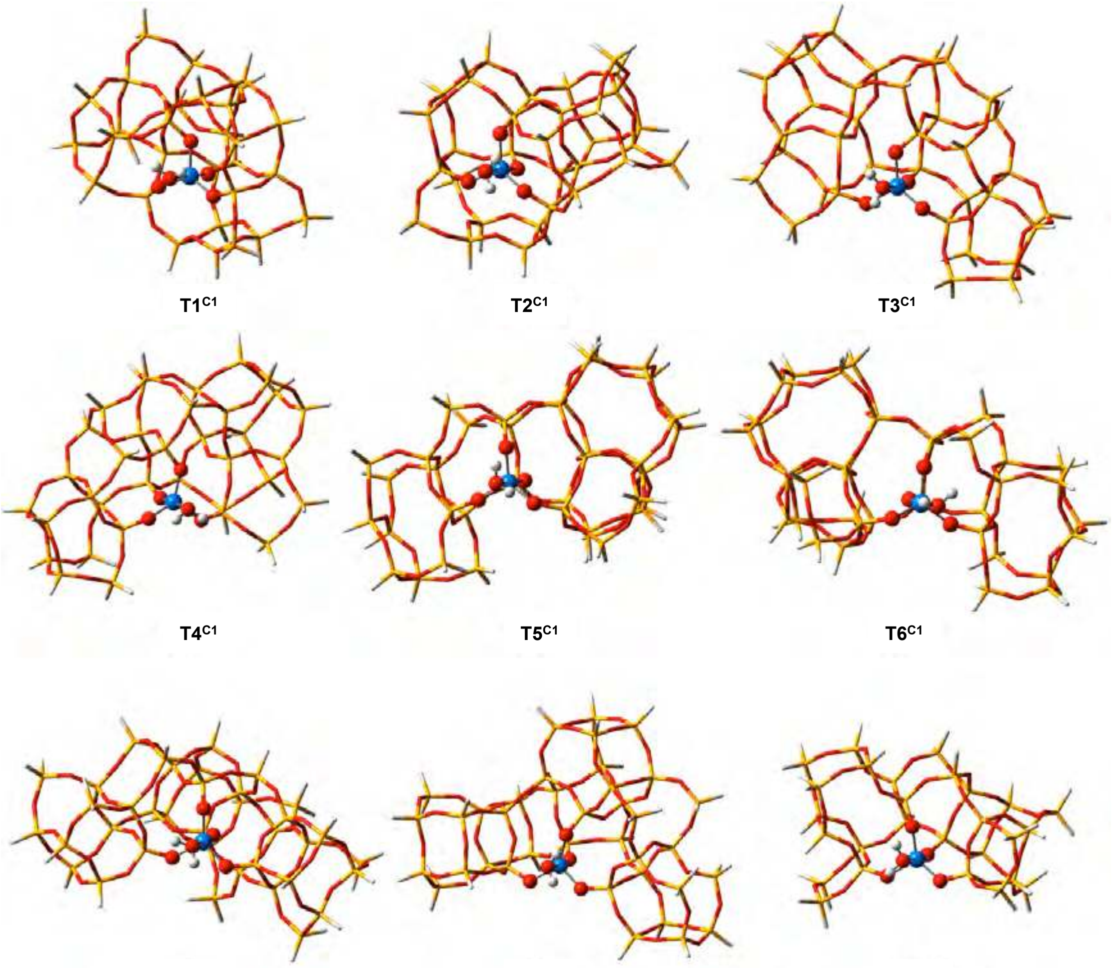

T1^{C1} T2^{C1} T3^{C1}

T4^{C1} T5^{C1} T6^{C1}

T7^{C1} T8^{C1} T9^{C1}

Figure S18. Optimized structures of all mono-hydrated closed sites of Sn-β. The Sn atom and its first coordination sphere are highlighted with ball and sticks model. Sn atoms are shown in blue, oxygen in red, silicon in yellow and hydrogen in white.

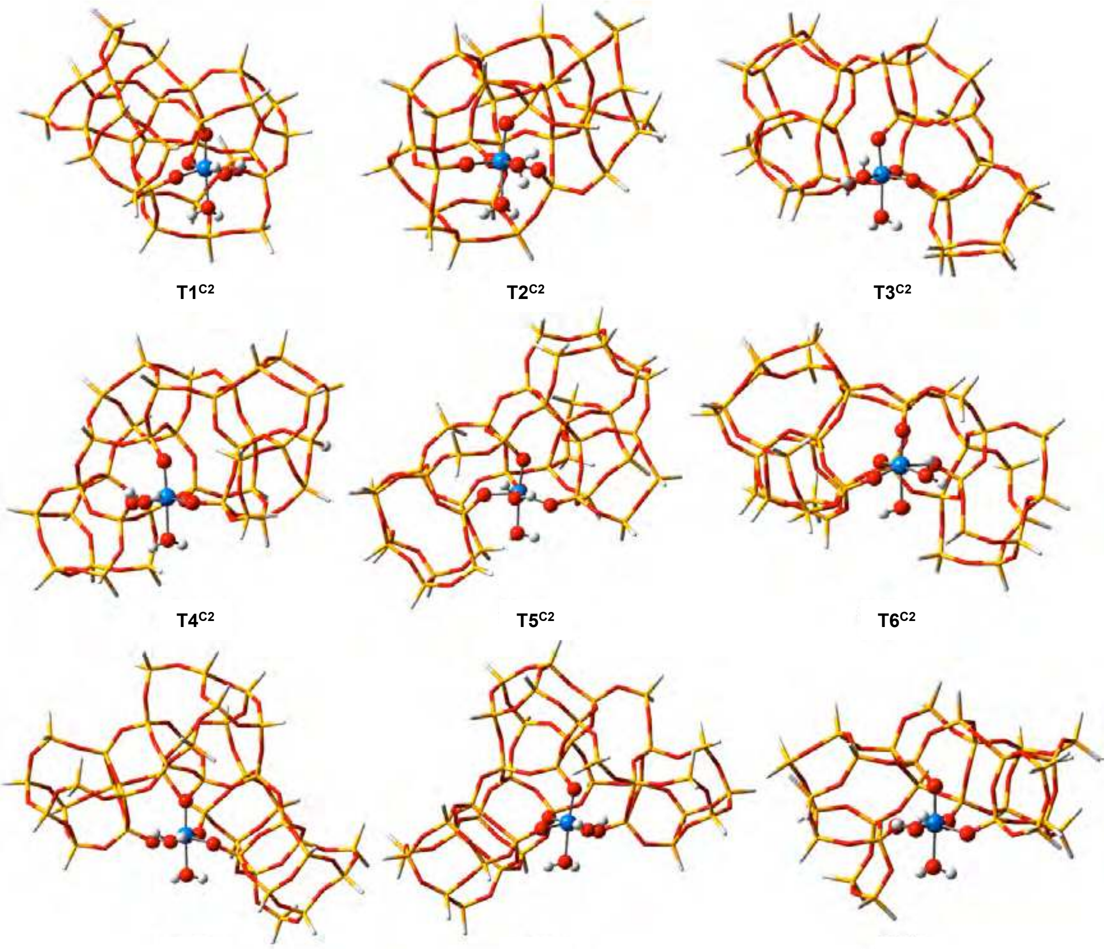

T1^{C2} T2^{C2} T3^{C2}

T4^{C2} T5^{C2} T6^{C2}

T7^{C2} T8^{C2} T9^{C2}

Figure S19. Optimized structures of all doubly-hydrated closed sites of Sn-β. The Sn atom and its first coordination sphere are highlighted with ball and sticks model. Sn atoms are shown in blue, oxygen in red, silicon in yellow and hydrogen in white.

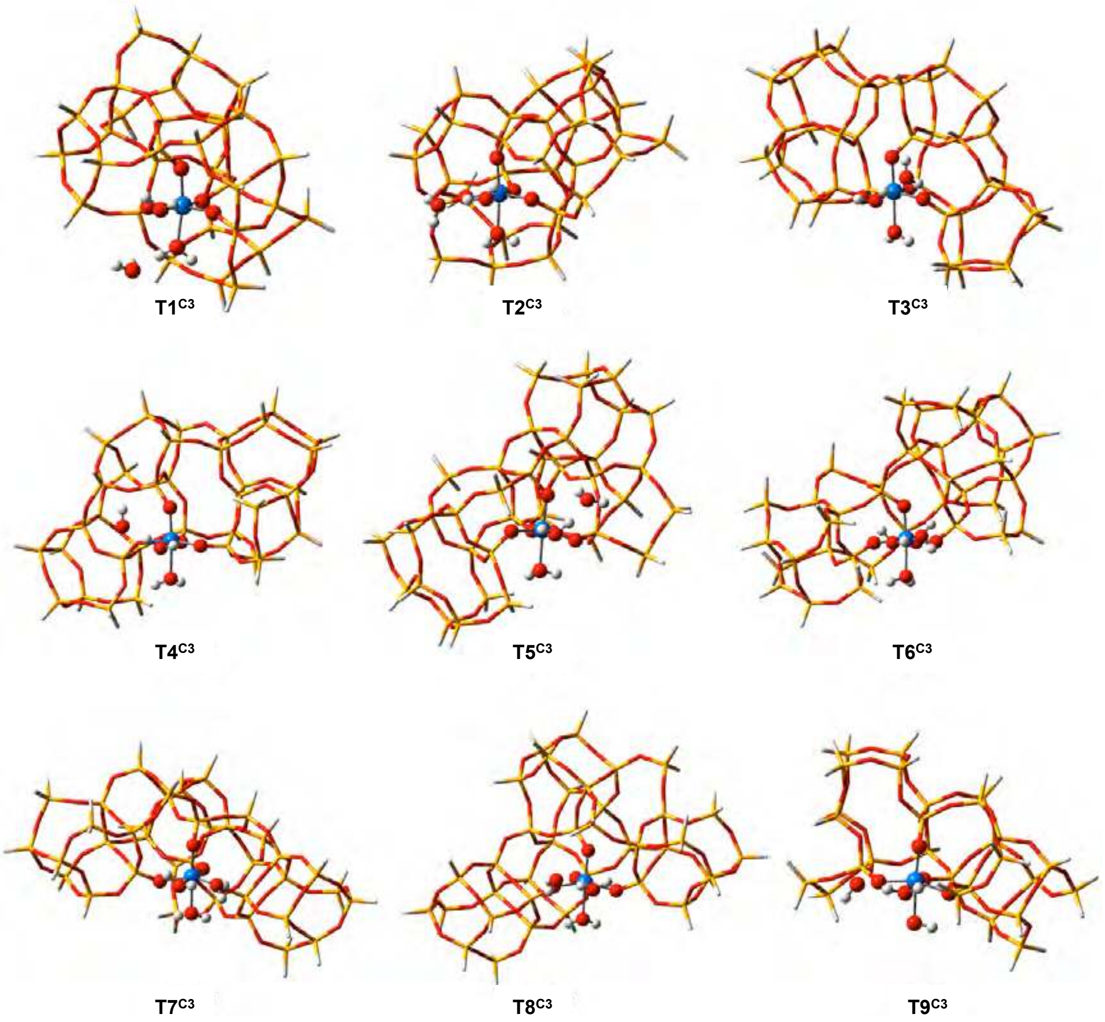

$T1^{C3}$ $T2^{C3}$ $T3^{C3}$

$T4^{C3}$ $T5^{C3}$ $T6^{C3}$

$T7^{C3}$ $T8^{C3}$ $T9^{C3}$

Figure S20. Optimized structures of all triply-hydrated closed sites of Sn-β. The Sn atom and its first coordination sphere are highlighted with ball and sticks model. Sn atoms are shown in blue, oxygen in red, silicon in yellow and hydrogen in white.

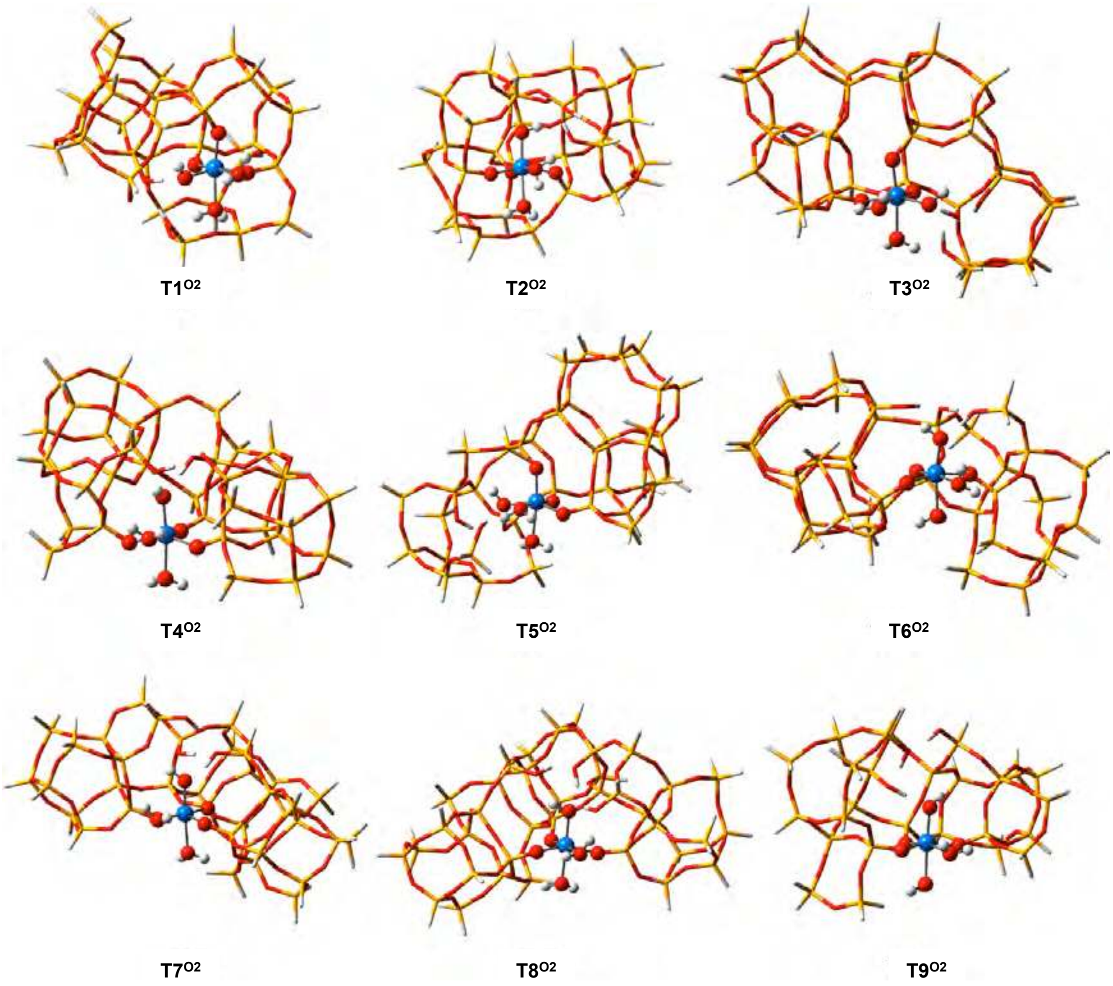

T1^{O2} T2^{O2} T3^{O2}

T4^{O2} T5^{O2} T6^{O2}

T7^{O2} T8^{O2} T9^{O2}

Figure S21. Optimized structures of all doubly-hydrated defect-open sites of Sn-β. The Sn atom and its first coordination sphere are highlighted with ball and sticks model. Sn atoms are shown in blue, oxygen in red, silicon in yellow and hydrogen in white.

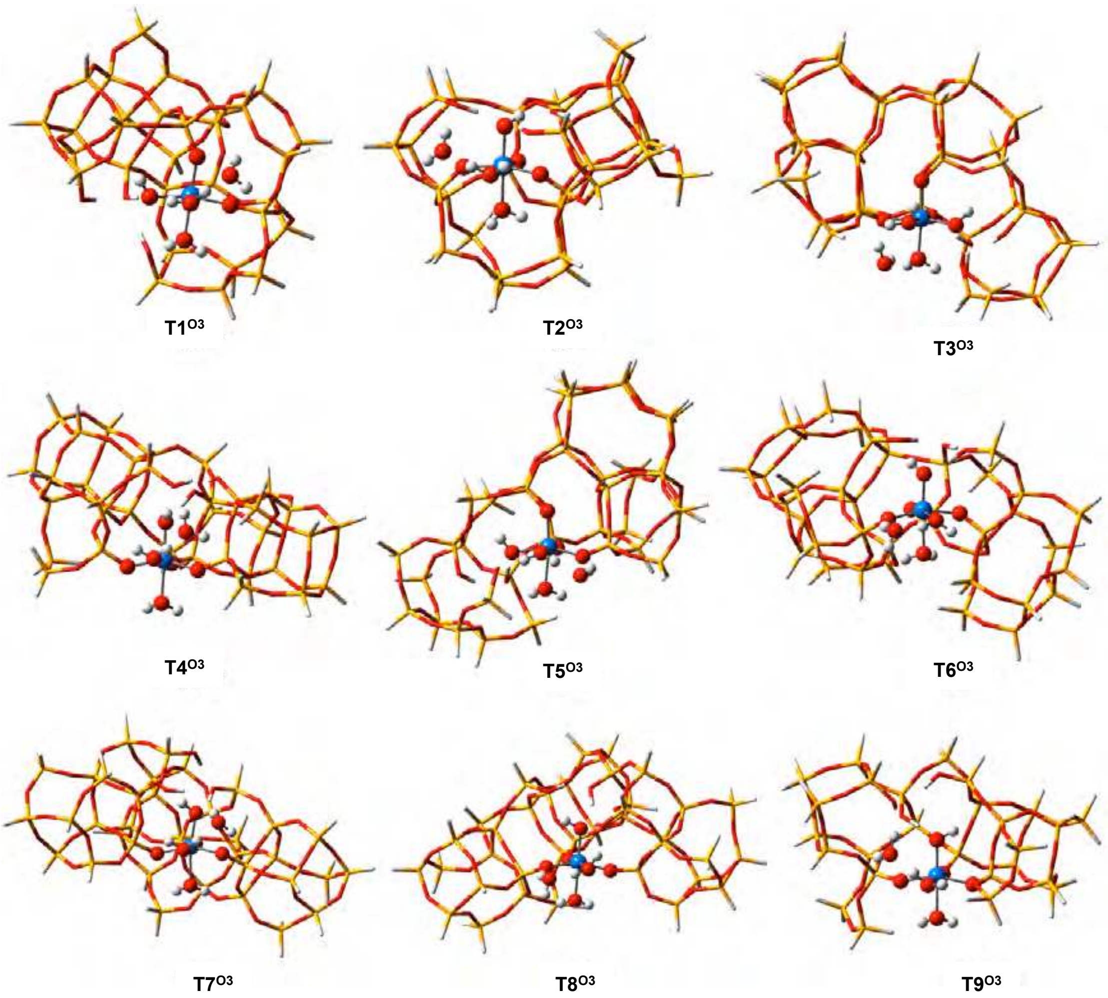

T1^{O3} T2^{O3} T3^{O3}

T4^{O3} T5^{O3} T6^{O3}

T7^{O3} T8^{O3} T9^{O3}

Figure S22. Optimized structures of all triply-hydrated defect-open sites of Sn-β. The Sn atom and its first coordination sphere are highlighted with ball and sticks model. Sn atoms are shown in blue, oxygen in red, silicon in yellow and hydrogen in white.

Table S9. Relative stabilities of the different T sites in cluster models of Sn-β. The ΔE energies correspond to electronic energies calculated with the B3LYP with dispersion corrections (B3LYP-D3). Energies are given in kcal·mol^{-1}

Site	**ΔE**
T1	0.0
T2	1.4
T3	3.4
T4	3.7
T5	6.9
T6	6.3
T7	2.9
T8	3.5
T9	3.2

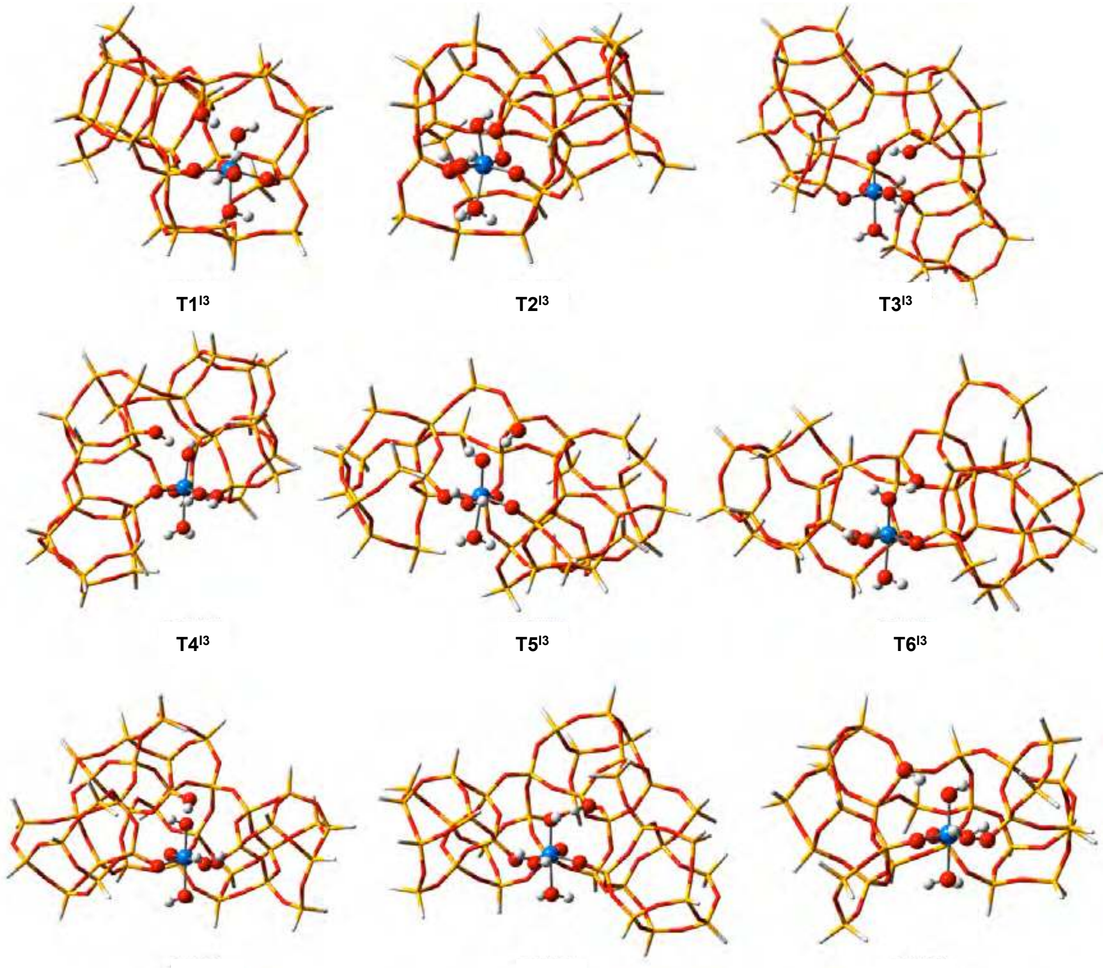

T1^{I3} T2^{I3} T3^{I3}

T4^{I3} T5^{I3} T6^{I3}

T7^{I3} T8^{I3} T9^{I3}

Figure S23. Optimized structures of hydrolyzed-open sites of Type I of Sn-β. The Sn atom and its first coordination sphere are highlighted with ball and sticks model. Sn atoms are shown in blue, oxygen in red, silicon in yellow and hydrogen in white.

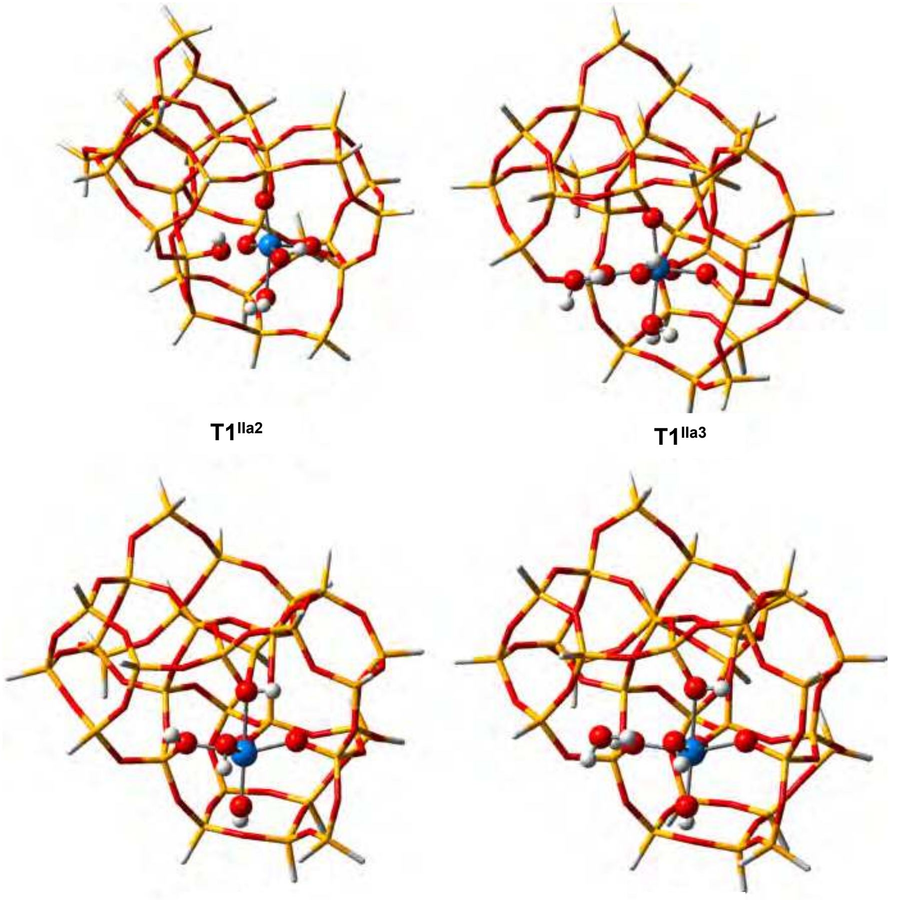

T1^{IIa2} **T1**^{IIa3}

T1^{IIb2} **T1**^{IIb3}

Figure S24. Optimized structures of T1 hydrolyzed-open sites of Type II of Sn-β. The Sn atom and its first coordination sphere are highlighted with ball and sticks model. Sn atoms are shown in blue, oxygen in red, silicon in yellow and hydrogen in white.

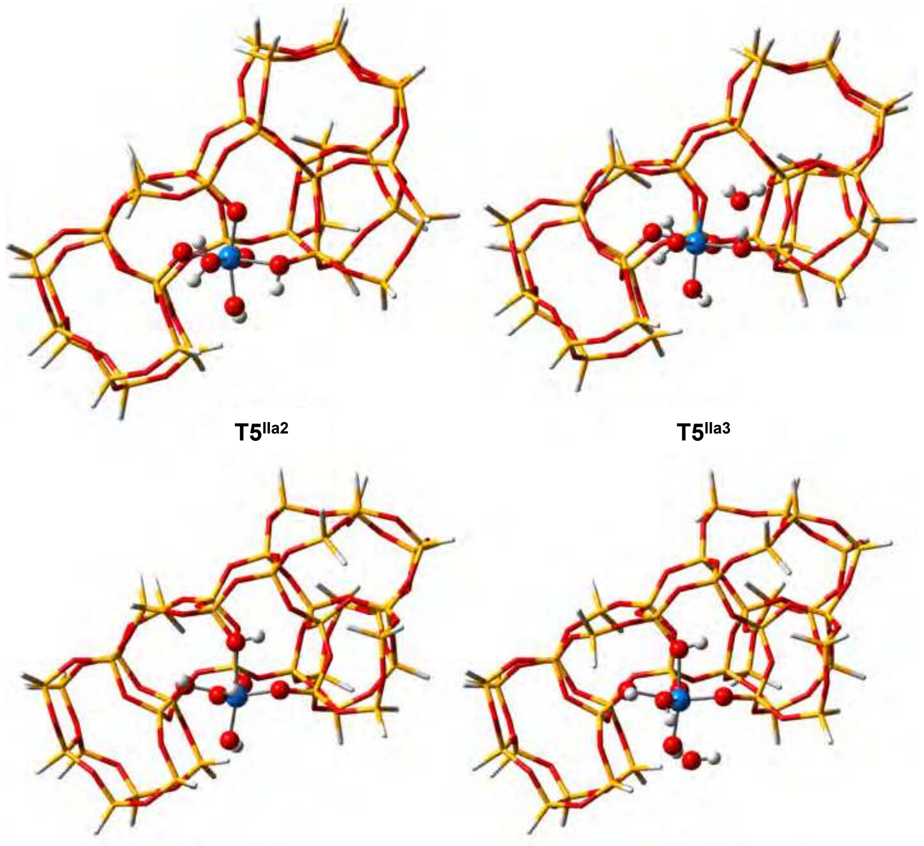

T5^{IIa2} **T5^{IIa3}**

T5^{IIb2} **T5^{IIb3}**

Figure S25. Optimized structures of T5 hydrolyzed-open sites of Type II of Sn-β. The Sn atom and its first coordination sphere are highlighted with ball and sticks model. Sn atoms are shown in blue, oxygen in red, silicon in yellow and hydrogen in white.

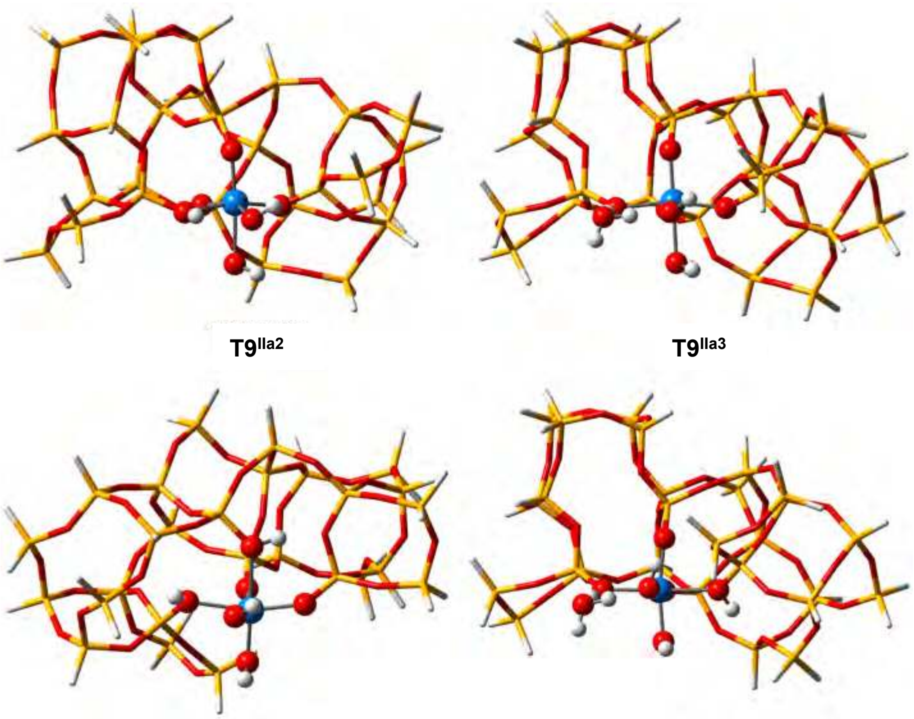

T9^{IIa2} T9^{IIa3}

T9^{IIb2} T9^{IIb3}

Figure S26. Optimized structures of T9 hydrolyzed-open sites of Type II of Sn-β. The Sn atom and its first coordination sphere are highlighted with ball and sticks model. Sn atoms are shown in blue, oxygen in red, silicon in yellow and hydrogen in white.

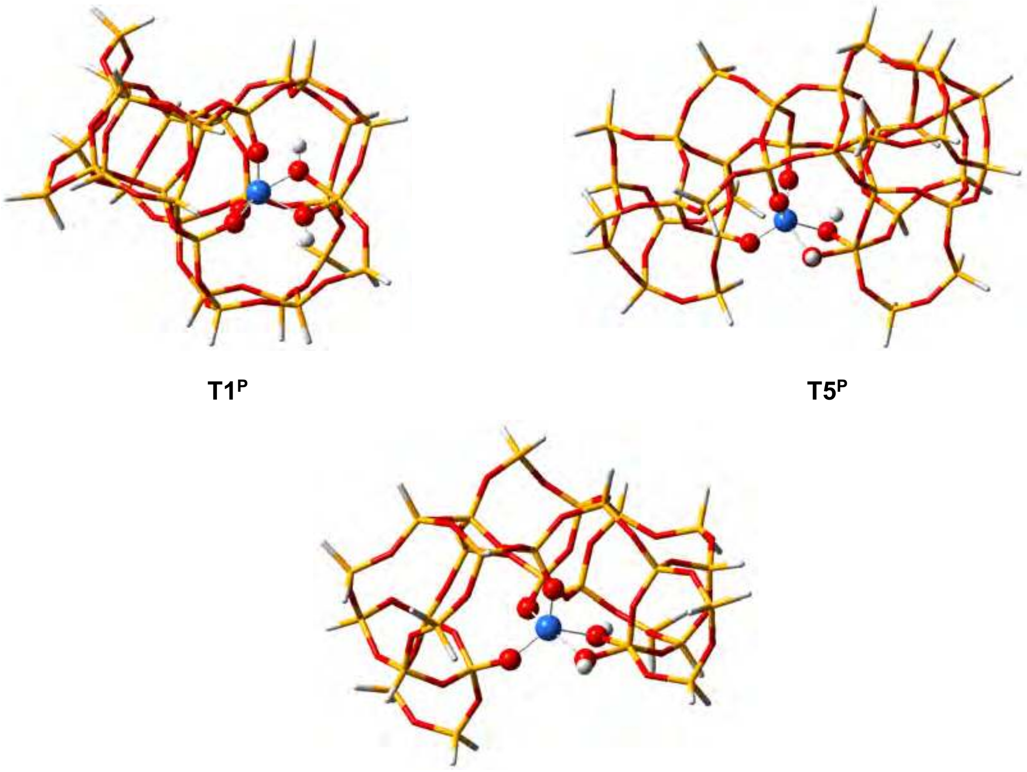

T1^{P} **T5^{P}**

T9^{P}

Figure S27. Optimized structures of T1, T5 and T9 penta-coordinated sites of Sn-β. The Sn atom and its first coordination sphere are highlighted with ball and sticks model. Sn atoms are shown in blue, oxygen in red, silicon in yellow and hydrogen in white.

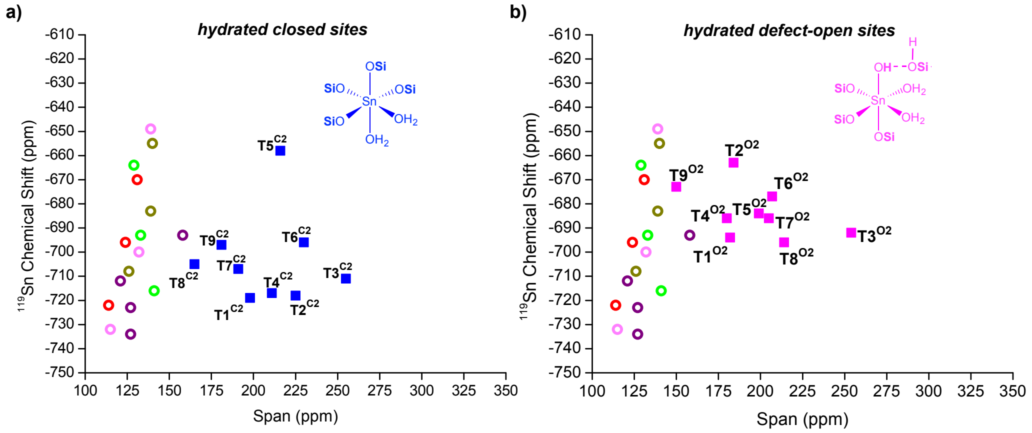

Figure S28. Comparison of measured and calculated ^{119}Sn NMR chemical shifts *vs*. spans. Calculations for a) double-hydrated **Tn^{C2}** (■) closed sites; b) double-hydrated **Tn^{O2}** (■) Experimental data are shown for hydrated Sn/deAl-Beta-OH-25 (○) Sn/deAl-Beta-OH-300 (○), Sn/deAl-Beta-F-30 (○), Sn-Beta-seed (○) and Sn-Beta (○).

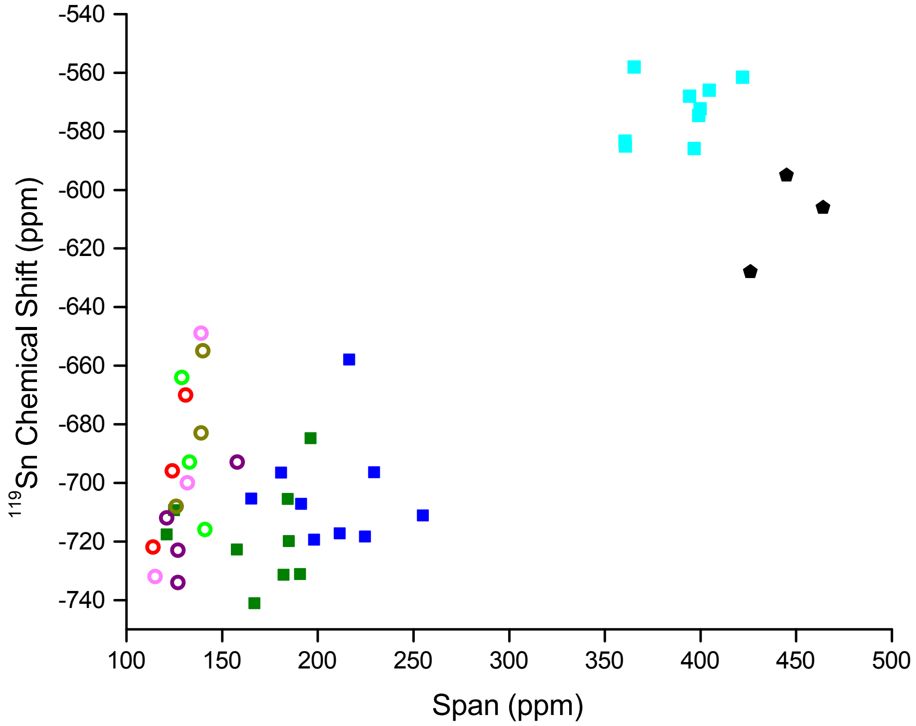

Figure S29. ^{119}Sn NMR chemical shift *vs*. span for mono-hydrated-hydrated **Tn**$^{\mathbf{C1}}$ (■), double-hydrated **Tn**$^{\mathbf{C2}}$ (■), triply-hydrated **Tn**$^{\mathbf{C3}}$ (■) closed sites and pentacoordinated hydrated **Tn**$^{\mathbf{P}}$ sites (⬟). Experimental data for hydrated Sn/deAl-Beta-OH-25 (○), Sn/deAl-Beta-OH-300 (○), Sn/deAl-Beta-F-30 (○), Sn-Beta seeded (○) and Sn-Beta unseeded (○) are also shown for comparison.

Text S1. Effect of water ligand conformations on the ^{119}Sn NMR signatures

We investigated the effect of variations of the water ligand on the ^{119}Sn NMR signatures of Sn-β. To this end, we decided to explore the NMR spectra of ^{119}Sn in constrained structures, that is, by selecting different degrees of freedom (geometrical parameters) involving the water molecules and calculate the NMR signatures for certain fixed values of those parameters. We chose two different parameters: the distance between Sn and the water molecule (Sn-OH_2) and the Sn-OH_2 rotational axis, as shown in Figure S30 (top). Exemplarily, we carried out the calculations only for the **T9^{C2}** site and explored the movement of only one water ligand, by fixing the mentioned parameters and freely optimizing the rest of the cluster. For the first parameter, the Sn-OH_2bond distance, we explored eight structures by increasing/decreasing the Sn-OH_2equilibrium distance four times by 0.05 Å, while for the second parameter, the Sn-OH_2rotational axis, we explored seven points resulting from the rotation of the Sn-OH_2bond around by 45°.

The results of these calculations are shown in Figure S30 (bottom). We observed in Figure S30a that the energetic variation of both processes is low compared to the equilibrium structure (eq). For the Sn-OH_2 bond distance the variation is at most 2.5 kcal·mol^{-1}, while for the Sn-OH_2 rotation the energy change for most of the explored structures compared to the equilibrium structure (eq) is below 1.5 kcal·mol^{-1} (only two points are about 3.0 kcal·mol^{-1} from the equilibrium structure). This means that the water ligand can actually fluctuate from the equilibrium distance with very low energetic cost. This result is in agreement with a recent *Ab initio* Molecular Dynamics (AIMD) study on the water absorption to the T2 site of the Sn-β. At T=300K, it was found that the water molecule prefers to coordinate to the heteroatom (Sn) and that the Sn-OH_2bond distance fluctuate with an average value of 2.44 Å.[2]

Figure S30b shows the variation of the ^{119}Sn NMR parameters (δ_{iso} and Ω) for the explored structures. For the Sn-OH_2 bond distance variation we observed that δ_{iso} only varies by 17 ppm at most (eq and point 8), while the variation in Ω is more drastic, with a window of 63 ppm (points 1 and 8). In the case of the Sn-OH_2 rotational axis, the variation in δ_{iso} and Ω is random. The largest variation in δ_{iso} is only 13 ppm, while that for Ω is 42 ppm.

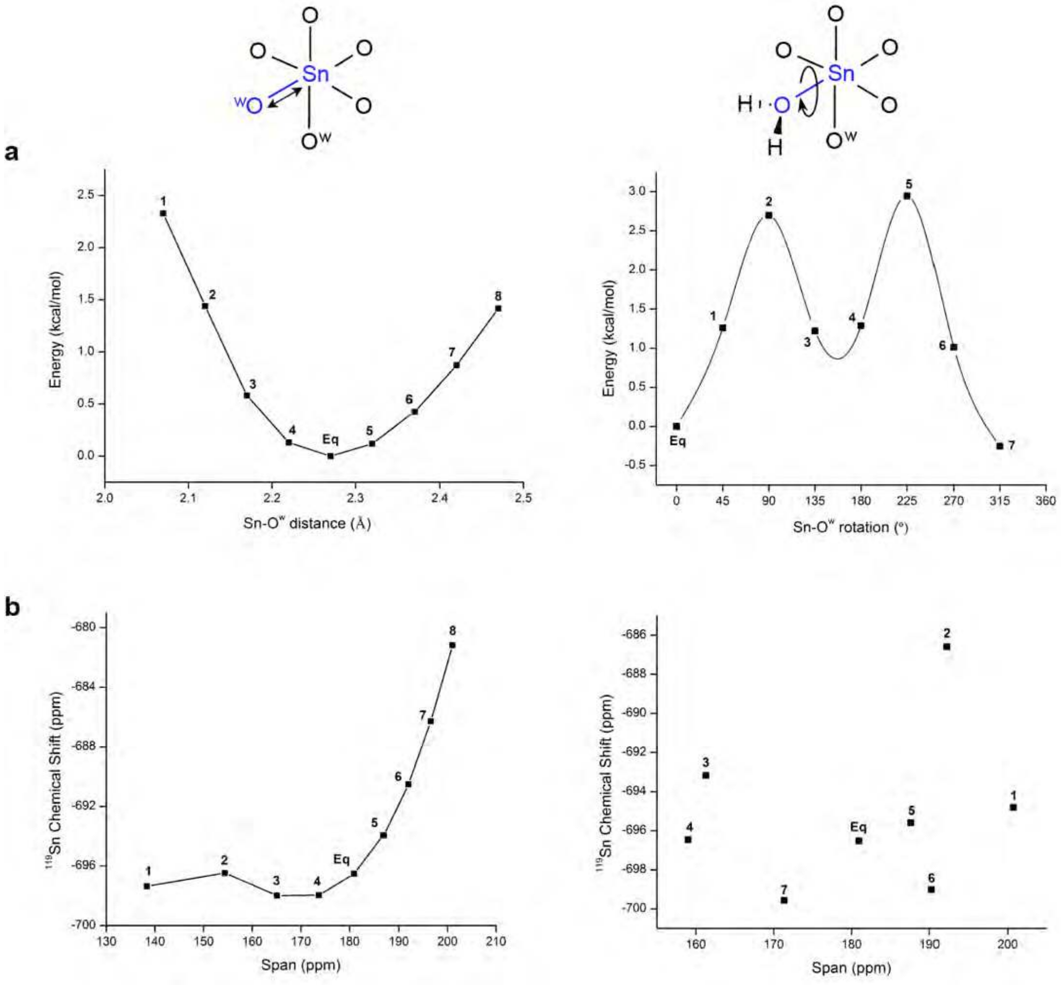

Figure S30. a) Electronic energy profiles for the Sn---OH$_2$ bond distance variation (left) and rotation (right) in the T9^{C2} site; b) ^{119}Sn NMR parameters for the variation of the Sn-OH$_2$ bond distance variation (left) and rotation (right) in the T9^{C2} site.

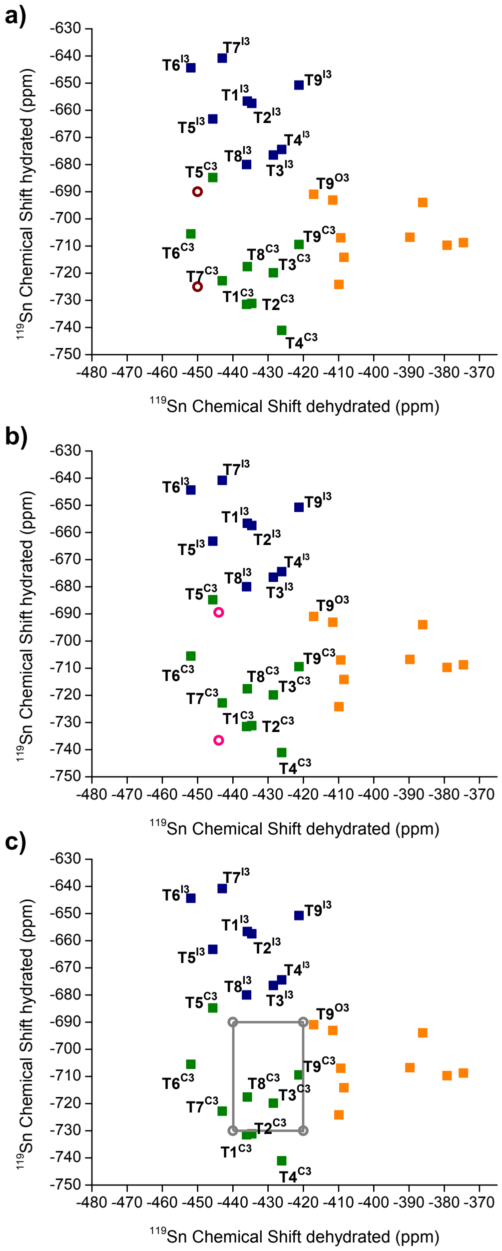

Figure S31. Comparison of experimental ^{119}Sn NMR chemical shifts found in literature with computational ^{119}Sn NMR. Calculations for dehydrated *vs*. hydrated of closed sites (■), defect-open sites (■) and hydrolyzed-open sites of type I (■). Experimental chemical Sn chemical shifts for hydrothermal Sn-ß samples from different research labs: (a) Román-Leshkov et al.[3] (○), (b) Corma et al.[4] (○), (c) Davis et al.[5] (○). The corner/intersections of the grids represent any possible combination of the chemical shifts in dehydrated and hydrated samples.

References

(1) Rouquerol, J.; Llewellyn, P.; Rouquerol, F. In *Stud. Surf. Sci. Catal.*; P.L. Llewellyn, F. R.-R. J. R., Seaton, N., Eds.; Elsevier: **2007**; Vol. Volume 160, p 49-56.

(2) Yang, G.; Pidko, E. A.; Hensen, E. J. M. *J. Phys. Chem. C* **2013**, *117*, 3976-3986.

(3) Gunther, W. R.; Michaelis, V. K.; Caporini, M. A.; Griffin, R. G.; Román-Leshkov, Y. *J. Am. Chem. Soc.* **2014**, *136*, 6219-6222.

(4) Corma, A.; Nemeth, L. T.; Renz, M.; Valencia, S. *Nature* **2001**, *412*, 423-425.

(5) Hwang, S.-J.; Gounder, R.; Bhawe, Y.; Orazov, M.; Bermejo-Deval, R.; Davis, M. *Top. Catal.* **2015**, 1-6.